NTNU
Faculty of Natural Sciences
and Technology
Department of Physics

MASTER'S THESIS FOR

MATS SIGSTAD

Study Direction Technical Physics

"Experimental studies of temperature effects on colloidal dispersions of clay nanoplatelets"

This work has been carried out at the Department of Physics at NTNU, Norway, under the supervision of Professor Jon Otto Fossum.

Trondheim, 07.05.10

Abstract

Colloidal dispersions of platelet-shaped particles may selforganize into liquid crystalline phases under certain conditions. Clays are both ubiquitous and important. Given their role in potential applications, e.g. in composite materials, clays that are able to self-organize have been given much attention during recent years. Platelet-shaped particles of the synthetic polydisperse 2:1 clay sodium fluorohectorite (NaFh), which under certain conditions show coexisting isotropic and nematic phases, have been studied by small angle x-ray scattering (SAXS).

It is found that positional correlations appear upon increasing the temperature from room temperature to around 40 degrees °C. This is evidenced by peaks in the SAXS patterns. It is also found that the intensity corresponding to real-space distances of the biggest particles decreases as the temperature is increased. Exfoliation of the thickest particles could be responsible for the SAXS patterns found. The study indicates that the concentration of salt in the dispersions plays an important role concerning the extent of exfoliation.

Contents

Preface

In this thesis, representing the efforts of one semester, I investigate the effects of heating aqueous dispersions of sodium fluorohectorite. The investigations have been both frustrating and rewarding, and it is with great pleasure I see that they have revealed some exciting behaviour. However, it must be stressed that this thesis never would have been were it not for the talented and helpful people working around me. I want to thank my supervisor, professor Jon Otto Fossum, for the possibility to gain experience and knowledge of an interesting subject, for insightful discussions, as well as giving me the freedom to explore the subject in whatever way I found best; co-student Christophe Coutant, who has been working on the same subject as me; PhD students Elisabeth Hansen and Henrik Hemmen have always been very helpful, no matter how silly or difficult my questions or wishes have been; post doc. Davi de Miranda Fonseca has in the same way been very helpful, modifying his ellipse fitting script to my needs. These persons also deserve a collective mention for performing the experiment on which most of this thesis is based, in Grenoble in May 2010. I am also grateful for the services provided by technician Ole Tore Buset, he was always there to help me whenever I have had any of the technical problems that inevitable show up during experimental studies. I also want to thank Henriette Frich for putting a smile on my face whenever I have been frustrated and tired. Finally, I want to thank my parents for always being there for me. They have been invaluable.

Mats Sigstad, Trondheim, July 2010.

Chapter 1

Introduction

In this master thesis, I aim to describe some of the aspects regarding the temperature dependency of salt-water solutions containing the synthetic clay sodium fluorohectorite (NaFh). The properties of such solutions have not, as far as the author is aware of, previously been investigated in detail. As clays are an important part of material science as well as interesting in its own right, this is important to investigate. The clay solutions, being inside glass capillaries of diameters of 1 and 2 mm, have been investigated mainly through the use of x-rays.

1.1 The structure of the thesis

In order to give a satisfactory description of the temperature dependency of a NaFh solution it is necessary to provide a background for the reader, on which the findings of the investigations can be evaluated. This background will inevitably contain descriptions of the structure and behaviour of clays, on several scales of magnitude. Some clays, among them NaFh, can organize its molecules in various ways. Some of these organization modes will be described. The branch of physics dealing with this, can be termed the physics of liquid crystals. Liquid crystals is an interdiciplinary branch, combining elements from physics, chemistry, engineering and more. Liquid crystals have proved to be useful in many applications, e.g. as in the popular Liquid Crystal Display (LCD) screens. The behaviour of NaFh has been investigated for several years, and some of the results from these investigations will be treated here in order to give the reader an idea of how the clay behaves.
The background will also have to plow into the nature and workings of x-rays, as these are an immensely important tool in this

thesis. X-rays are electromagnetic radiation from a specific part of the electromagnetic spectrum, and it is hence important to describe the nature of electromagnetic radiation. The basics of electromagnetism, as given by Maxwell, as well as those of wave mechanics, are given in the appendix. The appendix will provide the background for the somewhat more advanced theory in the theory section. In order to do this in an orderly fashion, descriptions of crystals and the so-called reciprocal space will be given.

The purpose of all this is of course to provide a sufficiently thorough fundament for the understanding of the diffractograms and the plots produced from them, from which the eventual conclusions of the experiments will be based. There is also an experimental section. What equipment have been used, as well as the physical conditions the clay solutions have been subjected to, will be treated.

1.2 General introduction

Clay is a ubiquitous material in the world. Clays are fine-grained materials with particle diameters of $< 2\mu$m. This is a definition from the nineteenth century [42] which applied to materials smaller than the resolution of optical microscopes. This small size gives clay crystals an important property; they have large surface area compared to the volume. Clays are both physically and chemically active, and can combine with water to make pastes, slurries and suspensions. Attracting water molecules, they can change their effective physical size [42]. Clays can take various chemical substances, i.e. ions and molecules, onto their surfaces or into their structure. These substances can easily be exchanged for others, given the right circumstances. Being abundant in the Earth's surface environment, while being very active, the importance of clay can hardly be overestimated.

In school, one is taught about three phases of matter; solid, liquid and gas. While these are the most commonly encountered phases, they are not the only ones. The difference between crystals and liquids, the two most common condensed matter phases, is that the molecules in a crystal are ordered whereas in a liquid they are not. The order in a crystal is usually both positional and orientational, in that molecules are constrained to both to occupy specific sites in a lattice and to point their molecular axes in specific directions. The molecules in liquids diffuse randomly throughout the sample container with the molecular axes pointing in all directions. The ordering of liquid crystals arise from the molecular form; the molecules constituting liquid crystals are anisotropic.

Another important property that differentiates solids and liquids is flow. Liquids flow and take the shape of the container, whereas solids do not flow and tend to retain their shape. The optical properties of liquids and some solids can also be quite different. For example, some solids change the polarisation of light whereas liquids do not. Many phases with more order than present in liquids but less order than typical of crystals also exist in nature. These phases are grouped together and called liquid crystals, since they share properties normally associated with both liquids and crystals [4]. The discovery of liquid crystals is usually attributed to an Austrian botanist by the name of Friedrich Reinitzer [4]. In 1888, he experimented with a substance related to cholesterol and noted that it had two melting points. At 154.5 °C it melted from a solid to a cloudy liquid and at 178.5 °C it turned into a clear liquid. He also observed some unusual colour behaviour upon cooling; first a pale blue colour appeared as the clear liquid turned cloudy and second a bright blue-violet colour was present as the cloudy liquid crystallised. Reinitzer sent samples of this substance to Otto Lehmann, a professor of natural philosophy, i.e. physics, in Germany. Lehmann was one of the people studying the crystallisation properties of various substances and Reinitzer wondered whether what he observed was related to what Lehmann was reporting. Lehmann had constructed a polarising microscope with a stage on which he could precisely control the temperature of his samples. This allowed him to observe the crystallisation of his sample under controlled conditions. Lehmann observed Reinitzer's substance with his microscope and noted its similarity to some of his own samples. He first referred to them as soft crystals; later he used the term crystalline fluids. As he became more convinced that the opaque phase was a uniform phase of matter sharing properties of both liquid and crystals, he began to call them liquid crystals [4]. They are now recognised as a stable phase for many compounds, thus putting them on equal footing to the solid, liquid and gas phases.

Scientifically, liquid crystals are an important phase for the investigation of cooperative phenomena, and liquid crystal synthesis is a field in its own right, especially in investigating structure-property relationships. Technologically, liquid crystals have become a part of our daily lives, first showing up in wristwatches and pocket calculators, but now being used for displays in all sorts of instrumentation, including portable computers and televisions [4].

This report concerns aqueous dispersions of colloidal clay nanoplatelets contained in glass capillaries. The synthetic clay sodium-fluorohectorite

(NaFh) has been investigated using optical birefringence and x-ray scattering techniques. Even though NaFh has been studied for years, e.g. a rich phase behaviour has been found in gravitationally settled dispersions [10], there are still physical characteristics which are unknown. In this report I investigate the effects of temperature on dispersions of NaFh and saltwater. The phase behaviour of NaFh includes liquid crystalline phases which are readily observed between crossed polarisers. So far no technologically important use has been found for NaFh, but the popular liquid crystal displays (LCDs), and the widespread use of clay elsewhere, suggest that NaFh could play an important role as an environmental-friendly material of tomorrow.

Chapter 2

Theory

In order to explain and interpret the results presented in this thesis, it is necessary that some theoretical background is present. The theory in this chapter will provide the reader with some basic knowledge within the fields of clays, colloids, liquid crystals and x-ray science. All these fields are highly relevant for this thesis.

2.1 Clays

Clays are fascinating, exciting and important materials. They are present almost everywhere on Earth, and their environment and that of human activity cross paths all the time. There has been suggested that clays played an important role in the formation of life on Earth [18]. Today, clays are used in a vast number of applications, such as cosmetics, pottery, confinement of hazardous waste storage and petroluem-relevant areas to name a few, and the knowledge of how clay soils behave when constructing buildings on them is utterly important. For this reason, among others, clays have been studied for centuries by geologists and geo-chemists. However, the fundamental study of some complex physical phenomena in clays is a relatively new field of research [11]. These phenomena are indeed interesting from a scientific point of view. In addition, liquid suspensions of clay can take the role as model systems for nanoparticle assembly and ordering, which means that studies of clays can prove to be a valuable tool in order to understand systems at this scale. The behaviour exhibited by saline solutions of sodium fluorohectorite is as an example of such a system.

2.1.1 Nanoscale clays

Phyllosilicates, from Greek *phyllon* meaning *leaf*, are sheets consisting of silicon and oxygen. Clay minerals, consisting of both natural and synthetic clays, are often phyllosilicates, even though this is not strictly necessary [2]. In order to discuss clay at this level, some elementary clay science should be presented.

One of the most important features of clays on the nanoscale is its sheet-like appearance. Two kinds of sheets, the tetrahedral and the octahedral, are bound together through the sharing of oxygen atoms. In natural minerals, the combinations of one tetrahedral and one octahedral layer (1:1), two tetrahedral and one octahedral layer (2:1), and two tetrahedral and two octahedral layers (2:1 + 1) are common [42]. The tetrahedral sheets consist in general of silicon (Si^{4+}) or aluminum (Al^{3+}) coordinated tetrahedrally by oxygen (O^{2-}). The octahedral sheets, on the other hand, consist mostly of aluminum (Al^{3+}), magnesium (Mg^{2+}) or iron (Fe^{2+} or Fe^{3+}), which is coordinated by O^{2-} or OH^- anions, and for some synthetic clays, fluorine F^- [29]. A single clay layer unit, given by one of the configurations discussed above, consists of several atomic planes. A 1:1 single clay layer unit is formed by five planes. First is the basal oxygen atoms of the silicate sheet, and secondly there is the cation coordinated by the basal oxygens and the apical oxygens. These apical oxygens, together with with one of the planes of oxygen and hydroxyl from the octahedral sheet, constitutes the third plane. The fourth plane is occupied by the cations of the octahedral sheet, while the fifth plane is the second oxygen and hydroxyl plane of the octahedral sheet. The 2:1 clay layer unit is similar, but this time the octahedral sheet is sandwiched in between the two tetrahedral sheets, which both have their apical oxygen pointing towards the octahedral sheet. It is this regular structure that justifies the use of the term unit cell when discussing clays. Figure 2.2 shows a 2:1 clay layer unit.

In a 2:1 clay layer, the unit cell is formed by 20 oxygens and four hydroxyl groups. There are eight tetrahedral sites and six octahedral sites along with four cavities surrounded by a six-membered oxygen ring on the surface. When two thirds of the octahedral sites are occupied by cations, the mineral is classified as a dioctahedral 2:1 phyllosilicate. A trioctahedral 2:1 phyllosilicate has all the octahedral sites filled with cations.

Based on the magnitude of the layer charge per unit cell, 2:1 phyllosilicates are divided into five groups; talc-pyrophillite, smectite, vermiculite, mica and brittle mica [24]. The members of each group are distinguished by the type and location of cations in the oxygen framework. The charge on the layers of smectites is intermediate and varies from 0.4 to 1.2 e^- per Si_8O_{20} unit. To balance the layer charge, layers of hydrated cations are intercalated between the clay layers, as illustrated in Figure 2.2. The moderate layer charge in smectite clays, gives physical and chemical properties that are not found in the end members mica and talc [24]. Some substitutions can cause a negative unit layer charge for some 2:1 clays. Tetravalent silicon may be substituted with trivalent aluminum in the tetrahedral sheet or tri- or divalent cations with di- or monovalentcations in the octahedral sheet.

Some clays have a special property; they are able to swell. It is known that in the spacing between the layers, which is occupied by cations whose effect is to allow stacking of the layers, also can be occupied by water molecules. The swelling property is determined by the ability of cations to retain their polar molecular 'shell', which can consist of e.g. water or glycerol, within the interlayer environment. This property is non-existent if the layer charge is either zero or too high and is characteristic of di- or trioctahedral smectites [29].

There are many types of clay, and it would be fruitless to mention them all in this context. However, some of the important features of the family of clays from which sodium fluorohectorite originates, will be given. Hectorite is a 2:1 phyllosilicate, meaning that the platelets are formed by two inverted silicate tetrahedral sheets, sharing their apical oxygens with one octahedral sheet sandwiched in between. It is classified as a trioctahedral smectite, and is octahedrally charged with Li^+ substituting for Mg^{2+} in the octahedral sheet, and its chemical formula (per half unit cell) is in general written as $(M_y \cdot nH_2O)(Mg^{2+}_{3-y}Li^+_y)Si^{4+}_4O_{10}(OH)_2$ [2, 24].

2.1.2 Sodium fluorohectorite

Sodium fluorohectorite (NaFh) is a synthetic smectite clay, which differs from natural hectorite in that the hydroxyl (OH) groups have been replaced by fluorine (F). The nominal chemical formula (per half unit cell) of NaFh is $Na_x(Mg^{2+}_{3-x}Li^+_x)Si^{4+}_4O_{10}F_2$, where $x = 0.6$, and the atomic configuration of NaFh is shown in Figure 2.2 [21, 38]. One such layer consists of one aluminum octahedral layer between two silicon tetrahedral layers. This configuration is the 2:1 layer unit discussed above. These layers have a negative surface charge of 1.2 e^- per unit cell. Smectites have an intermediate layer charge, usually from 0.4 e^- - 1.2 e^-. per unit cell, which means that the

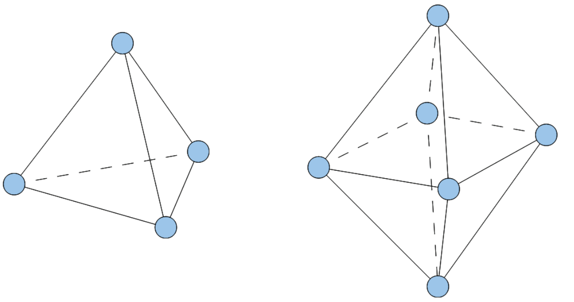

(a) A tetrahedron.

(b) An octahedron.

Figure 2.1: To the left is a tetrahedron, a polyhedron consisting of four triangular faces. Three triangles meet at each of the four vertices. To the right is an octahedron, consisting of six triangular faces. Here, four triangles meet at each of the six vertices.

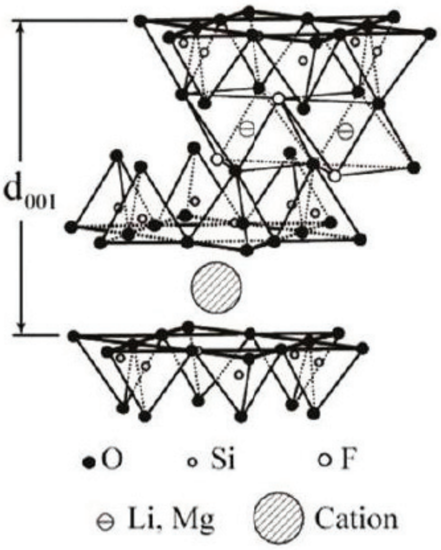

Figure 2.2: The atomic configuration of fluorohectorite. For NaFh, the intercalated cation is Na^+. Figure from [21].

layer charge of NaFh is quite large compared to other, similar unit cells [24]. Several such layers can stack together if intercalated ions such as Na^+ or Ka^+ balance the charge. These ions are commonly called counterions [10]. The NaFh particles are composed by 20-100 silicate lamellae that stack by sharing Na^+ ions between their basal planes. The thickness of each lamellae is around 10^{-9} m, meaning that each particle has a thickness of the order of 0.1 μm. The particle diameter[1] can be as large as 20 μm. NaFh particles have shown a quite large polydispersity, meaning that the particles varies in size. The high layer charge cause the platelets to remain stacked even when suspended in water [36].

Dry NaFh powder has no water molecules between the layers, but given enough humidity, both one water layer (1WL), and two water layers (2WL) are possible. As the word *swelling* implies, the interlamellar distance between the stacked platelets is affected by the amount of water between them. As one intuitively think, more water between the layers increases the distance between them. For 0WL, the distance has been measured to 10 Å, while the interlamellar distances for 1WL and 2WL have been measured to 12 and 15 Å, respectively [38].

Sodium fluorohectorite in saltwater solutions

Systems of platelet-shaped nanostacks of the synthetic clay NaFh, suspended in saline solutions of various salt concentrations, exhibit a rich phase behavior with up to four phases coexisting in a single sample tube [10].

A polydisperse suspension of NaFh will, over time, be sorted by particle size and concentration in the gravitational field. This separates the suspension into different coexisting strata, like gels, sols[2], and sediments. Typically, e.g. if the container is a 2 mm diameter glass capillary, the upper stratum will be isotropic, in the middle it will be nematic, and at the bottom a sediment consisting of large particles aggregates. While it is the gravitational force that causes the initial phase separation, other effects can play a role too. For example, it has been shown that evaporation can play a significant role. Hansen [20] isolated the isotropic phase into a separate container, and observed that after evaporation, a highly ordered nematic remained,

---

[1] Using the word *diameter* does not imply that the particles have to be circular.

[2] A sol is a colloidal dispersion of small particles suspended in a liquid. Under suitable conditions, the particles in some sols can be made to react or interact electrostatically so that they form a continuous, three dimensional network of connected particles, known as gel, instead of aggregating to form larger, discrete particles, as happen in precipitation or flocculation [7].

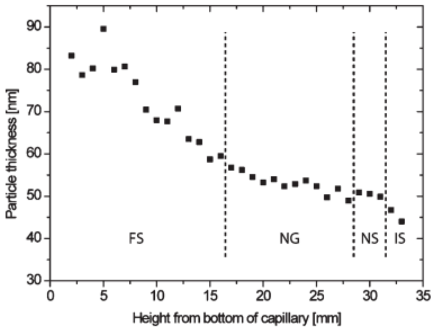

Figure 2.3: A wide angle x-ray scattering study lead to an estimation of the average particle thickness as a function of height in a capillary of a four week old dispersion of 3 % w/w NaFh, 1 mM NaCl. Figure from [21].

i.e. evaporation is an effective means of achieving highly ordered nematic phases. When a sample undergoes evaporation, the age of the sample is important when the behaviour of the sample is considered. Evaporation is likely to cause a concentration increase near the surface, and if the sample is old enough, i.e. gelled, the high concentration near the surface is likely to remain so because of the slow dynamics hindering the establishment of thermal equilibrium in the sample as a whole. Thus did she observe largest order at the surface [20].

Hemmen *et al.* [21] have shown that the thickness of the particles in the isotropic phase is smaller than in the nematic phase, with strong indications of the particle diameters being smaller in the isotropic phase due to the ability of these particles to stay dispersed for several months. Is is tempting to imagine, quite simply, that the bigger particles sink to the bottom, while it is the smaller one which stay suspended. An estimate of the average particle thickness as a function of heights in the flocculated sediment (FS), nematic gel (NG), nematic sol (NS) and the isotropic sol (IS) of a four week old dispersion of 3 % w/w NaFh, 1 mM NaCl, is shown in Figure 2.3. Such suspensions can be studied by several means, of which x-rays is an important one. X-ray measurements can be used to determine the anisotropicity of the sample, and together with x-ray absorption measurements, this information can be used to elucidate the phase boundaries and a measure of the orientational ordering of the various phases. The coexistence of different phases, as stated above, is due to a sedimentation-induced vertical gradient in particle fraction. A quantitative relation of the vertical coordinate to the clay particle fraction in these samples has allowed a determination of a phase diagram of this system, as a function of particle fraction and salt concentration, as seen in Figure 2.4 [10].

As indicated in the phase diagram, the strata depends on salt concentration as well as clay content. In [36], the authors explain that the dependence on ionic strength displays three regimes, irrelevant of clay content. For 0.1 - 5 mM NaCl, which can be considered low ionic strength, the Debye screening length, a length which describes the range of repulsion in an ionic solution, is longer than the attractive van der Waals force range, which in turn leads to the particles repelling each other electrostatically. Entropy-driven Onsager-type nematic ordering may occur in this regime, although gelation effects could play a role. In the second regime, for ionic strengths above about 5 mM, the authors believe that the van der Waals forces comes into play and that the particles attract each other locally according to the DLVO model of colloidal interactions. This results in small-domain regimes of attractive nematiclike ordering. Finally, for ionic strengths over about 10 mM, the clay particles tend to aggregate into larger assemblies. For such strong ionic strengths, the van der Waals force dominates [36]. The DLVO model and the effect of salt concentration will be discussed in more detail in section 2.2.

2.2 Colloids and colloidal interactions

Colloidal particles in dispersions have sizes which range from 10 - 10 000 nm and are typically suspended in a host medium. In colloids, the particles are solid, in contrast to emulsions, where surfactant-coated liquid droplets are dispersed in a fluid medium, or in the case of aerosols, where fluid or solid particles are floating in a gaseous environment. There exists a whole zoo of interactions between particles whose delicate balance determines the stability of a colloidal dispersion [26].

In the following I will try to give a introductory overview of *some* of the forces that has to be taken into consideration when dealing with colloidal dispersion. A complete theoretical understanding of the subject at hand is still not in place, but the celebrated DLVO theory is indeed able to explain many aspects concerning such dispersions.

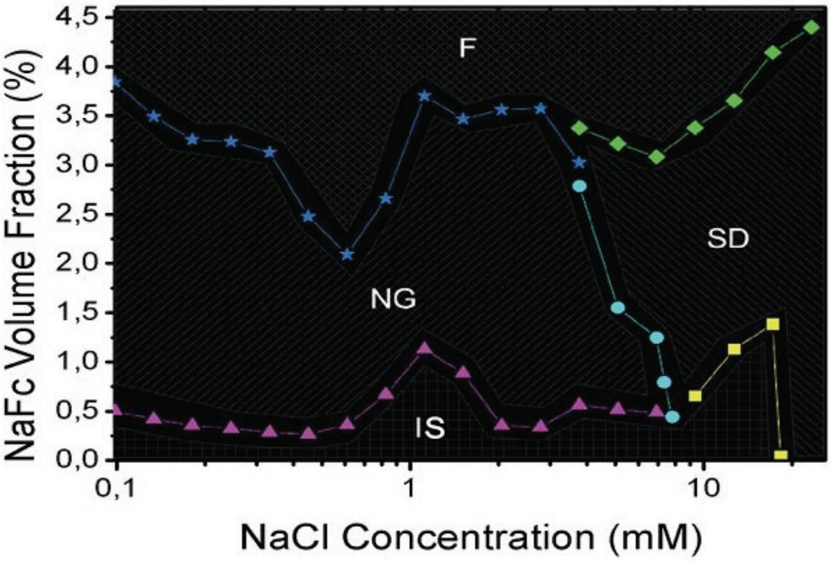

Figure 2.4: The phase behaviour of saline solutions of NaFh is a function of both salt concentration and clay volume fraction. Upon gravitational settling in capillaries, the different phases can all be visible after sufficient time. F, NG, SD and IS represent Flocculated sediment, Nematic Gel, Small Domains and Isotropic Sol, respectively. Figure from [10].

According to this theory, particles that are insoluble in a solvent can form colloidal dispersions when forces preventing aggregation are present. Colloidal stability occurs when the colloidal particles are trapped in a local minimum of the potential energy arising from the attractive van der Waals forces and the repulsive double layer interactions, or when repulsive forces prevent flocculation. In order to reach this conclusion, both forces should be properly introduced. This will be the purpose of the following sections.

2.2.1 The pair potential

At the most basic molecular level, the interaction potential between two particles, like atoms or molecules, is decisive when trying to determine their behaviour. This potential is often referred to as the *pair potential*. When the interaction takes place in a solvent medium, some call it the *potential of mean force*. The potential $w(r)$ is related to the force between the two particles by $F = -\mathrm{d}w(r)/\mathrm{d}r$. The derivative of $w(r)$ with respect to distance r gives the force, and hence makes it possible to calculate the work that can be done by the force. $w(r)$ is often referred to as the *free energy* or *available energy* [23].

2.2.2 Van der Waals forces

Van der Waals forces are ubiquitous, but also very weak. Because of this, they are only important when other and usually stronger forces are absent or correspondingly weak. The attractive nature of this force is due to dipole-dipole interactions between even closed-shell atoms with spherically symmetric charge distributions. This attractive interaction has a characteristic r^{-6} dependence, which can be derived from classical electrostatic considerations, even though it should be treated as a quantum mechanical phenomenon [7]. The following hand-waving argument explains what the force is about: if a fluctuation of an otherwise spherical symmetric charge distribution, which could be that of an atom, should appear, it will produce an instantaneous dipole moment p_1. This dipole moment, in turn, will give rise to an electric field at a distance r from the perturbed charge distribution of the form $E \propto p_1/r^3$. This electric field can polarize a second atom at r, inducing a dipole moment $p_2 \propto \alpha p_1/r^3$, where α is the polarizability of the second atom. As the potential of a dipole $\vec{p}$ in a field $\vec{E}$ varies as $\vec{p} \cdot \vec{E}$, it follows that this attractive interaction varies as $-Cr^{-6}$, where C for now is an arbitrary constant [7]. However, this attraction must somehow be countered at some time, if the particles are not to collapse into each other. Ultimately, the electronic charge distributions of the two atoms will start to overlap, leading to the electrons being promoted to a higher-lying state in order to satisfy the Pauli exclusion principle[3]. This increases the electronic energy, and thus leads to a repulsive action. This action varies very rapidly with r, and it is often convenient to describe the action with a empirical power law of the form B/r^{-n}, where $n = 12$. That 12 is chosen is partly due to the abrupt changes this exponent produces, and partly because computations are simplified [7]. The combined potential of attractive and repulsive nature can be described mathematically by a Lennard-Jones type potential

$$w_{vdW}(r) = 4\eta \left[\left(\frac{\nu}{r} \right)^{12} - \left(\frac{\nu}{r} \right)^{6} \right], \tag{2.1}$$

where the parameters η and ν have the units of energy and length, respectively [7].

---

[3] The Pauli exclusion principle states that a single-particle state can not be occupied by more than one electron [33]. This limits the number of electrons having approximately the same energy in atoms.

The Hamaker constant, an important concept related to vdW forces between surfaces

The interaction energies originating from the van der Waals forces acting between pairs of bodies can be calculated. If we assume that the interaction takes place in vacuum, and that the interaction is non-retarded[4] and additive, the interaction energy can be found by summing the energies of all the atoms in one object with all the atoms in the other object. This procedure can be carried out for several geometries, and the result is given in terms of the Hamaker constant [23]

$$A = \pi^2 C \rho_1 \rho_2, \tag{2.2}$$

where ρ_i is the number density of body i, and C is a material coefficient related to the interatomic van der Waals pair potential of the form $w(r) = -C/r^6$.

The van der Waals interaction energy between two charges surfaces

For two surfaces separated by a distance D, the van der Waals interaction free energy per unit area becomes [25]

$$V_{vdW} = -\frac{\pi C \delta^2 \rho^2}{2D^4} \tag{2.3}$$

if the thickness δ of the plates is much smaller than the plate separation D, and

$$V_{vdW} = -\frac{\pi C \rho^2}{2D^2} \tag{2.4}$$

if $\delta > D$.

The Debye length

In 1923, Debye and Hückel presented a model in which the coulombic interactions of a weak electrolyte solution could be described in a quantitatively manner [39]. This theory aims to calculate the change in the Gibbs free energy G which results from the coulombic forces between the ions. Starting with the equation

$$\delta G = RT \ln \gamma_+ \gamma_- = \frac{1}{2} N_A e \overline{V}(0). \tag{2.5}$$

The activity coefficients $\gamma_\pm$ expresses the lowering of the Gibbs free energy, and determines the electric potential wihich is generated by all other ions at the place of a positive ion. The time-averaged

---

[4] i.e. the speed of light in the medium, if it is not vacuum, is still so high that the effect happens almost immediately after the cause.

potential $\overline{V}(0)$ is used as this potential is varying over time. The potential is determined by the charge distribution around a particular ion [39], and can be evaluated if the average charge distribution around the ion is known. The charge distribution $\overline{\nu}(r)$ around a positive ion is given by the pair distribution functions g_2^{-+} and g_2^{++}. They describe the density of negative and positively charged ions around our chosen positive ion, respectively. By solving the Poisson equation

$$\nabla^2 \overline{V}(\vec{r}) = -\frac{\overline{\nu}(\vec{r})}{\epsilon\epsilon_0}, \tag{2.6}$$

the potential $\overline{V}(0)$ can be determined. For an isotropic system, the following equation applies [39]

$$\frac{1}{r^2}\frac{\mathrm{d}}{\mathrm{d}r}\left(r^2\frac{\mathrm{d}}{\mathrm{d}r}\right)\overline{V}(r) = -\frac{\overline{\nu}(\vec{r})}{\epsilon\epsilon_0} \tag{2.7}$$

The pair distribution of liquids can not be found analytically, but Debye and Hückel chose an approach that was approximately of nature. They assumed that the particles were non-interacting, but instead exposed to an electric field $V(\vec{r})$. By establishing the particle density distribution as determined by Boltzmann statistics, the local densities $\rho_\pm$ is given as

$$\rho_\pm = \overline{\rho}_\pm \exp{[\mp\frac{e\overline{V}(\vec{r})}{k_\mathrm{B}T}]}, \tag{2.8}$$

so that the densities become alike for vanishing potentials. Then the charge density distribution is given as

$$\nu(\vec{r}) = e\overline{\rho}_+ \exp{[\frac{-e\overline{V}(\vec{r})}{k_\mathrm{B}T}]} - e\overline{\rho}_- \exp{[\frac{e\overline{V}(\vec{r})}{k_\mathrm{B}T}]}. \tag{2.9}$$

For large kinetic energies, at least compared to the potential energy, the following holds:

$$\frac{eV}{k_\mathrm{B}T} << 1. \tag{2.10}$$

Then linear approximation is possible, i.e.

$$\nu(\vec{r}) \approx -2e\overline{\rho}_+\frac{eV(\vec{r})}{k_\mathrm{B}T}. \tag{2.11}$$

Debye and Hückel used this equation for the charge distribution and the variation of potential in the vicinity of an ion, and found that it was able to describe the behaviour of such systems. A system of interacting particles had been reduced to a system of individual particles acting in a collective field.

By combining Eq. 2.7 and Eq. 2.11, and thus eliminating $\overline{\nu}(r)$, the following equation is obtained [39]:

$$\frac{1}{r^2}\frac{\mathrm{d}}{\mathrm{d}r}\left(r^2\frac{\mathrm{d}}{\mathrm{d}r}\right)\overline{V}(r) = \frac{1}{\lambda_D^2}\overline{V}(r), \tag{2.12}$$

where λ_D, the Debye length, is

$$\lambda_D = \left(\frac{\epsilon\epsilon_0 k_\mathrm{B}T}{2\overline{\rho}_+ e^2}\right)^{1/2}. \tag{2.13}$$

Eq. 2.12 can be solved exactly, resulting in the general solution

$$\overline{V}(r) = \frac{c_1}{r}\exp\left[-\frac{r}{\lambda_D}\right] + \frac{c_2}{r}\exp\left[\frac{r}{\lambda_D}\right]. \tag{2.14}$$

As $\overline{V}(r)$ has to approach zero for large values of r, the constant has to be equal to zero, which means that

$$\overline{V}(r) = \frac{c_1}{r}\exp\left[-\frac{c_1}{\lambda_D}\right]. \tag{2.15}$$

λ_D characterises the extension of the ion cloud around the ion in which we are interested, and it can be seen that the accumulation of ions around this ion leads to a screening effect that effectively reduces the strength of the coulombic interactions at distances large compared to the Debye length. Inspecting the expression for the Debye length, it becomes clear that both ionic concentration and temperature affects the behavior of screened systems like these. While an increase in temperature increases the Debye length, thus rendering the screening less effective, an increase of ion concentration has the opposite effect.

2.2.3 The electric double layer

There are not many systems in which the van der Waals forces alone determine the total interaction. In more complex systems, like saline solutions of clay nanoplatelets, long-range electrostatic forces must be included. Were the van der Waals force the only force, one would expect similar particles in a medium to aggregate and precipitate out of solution as a solid mass. However, when the surface of the particles are charged, electrostatic forces may keep the particles from aggregating. In overall neutral solution, the charged surfaces will be balanced by an equal but oppositely charged region of counterions. Some of these are, transiently or not, bound to the surface within what is usually called the *Stern* or *Helmholtz* layer, while others are forming an atmosphere of ions in rapid motion close to the surface. This is the diffuse *electric double layer* [23]. The ions in this layer will experience a net electric potential, which will lead to increased concentrations of the ions near the oppositely charged surfaces.

Now, the following question arise: How is the distribution of counterions between two charged surfaces? And how does this affect the forces between the surfaces? To answer this question, I will rely heavily on chapter 12 in Israelachvili [23].

When only counterions are present in a solution, the chemical potential μ of any ion can be written like [23]

$$\mu = ze\psi + k_B T \log \rho. \tag{2.16}$$

Here, ψ represent the electrostatic potential and ρ the number density of ions having valency z at any point between two surfaces. For convenience, $\psi_0 = 0$ at the midpoint between the two surfaces. At this point, we also note that $\rho = \rho_0$ and $\left(\frac{\mathrm{d}\psi}{\mathrm{d}x}\right)_0 = 0$ for symmetry reasons. In an equilibrium sitation, the chemical potential is uniform throughout the whole area being in equilibrium. Assuming this, we use Eq. 2.16 and find the Boltzmann distribution at any point x:

$$\rho = \rho_0 \exp \frac{-ze\psi}{k_B T}. \tag{2.17}$$

The Poisson equation is well known from electromagnetics[5]. In this setting, it can be written for the net excess charge density at x, giving

$$ze\rho = -\epsilon\epsilon_0 (\mathrm{d}^2\psi/\mathrm{d}x^2). \tag{2.18}$$

Combined with Eq. 2.17, this yields the so-called Poisson-Boltzmann equation:

$$\frac{\mathrm{d}^2\psi}{\mathrm{d}x^2} = -\frac{ze\rho}{\epsilon\epsilon_0} = -\frac{ze\rho_0}{\epsilon\epsilon_0} \exp -\frac{ze\psi}{k_B T}. \tag{2.19}$$

This equation can be solved in order to find the electric potential, and therefore also the electric field. As an example, the Poisson-Boltzmann equation can be solved to find the electric field E_s at the surfaces. To do this, two boundary conditions must be utilized. Firstly, the electric field in the midplane between the two surface $E_0 = \left(\frac{\mathrm{d}\psi}{\mathrm{d}x}\right)_0 = 0$. Secondly, the overall electroneutrality must be preserved. The surface charge σ must be balanced by an equal and

---

[5] See the Appendix.

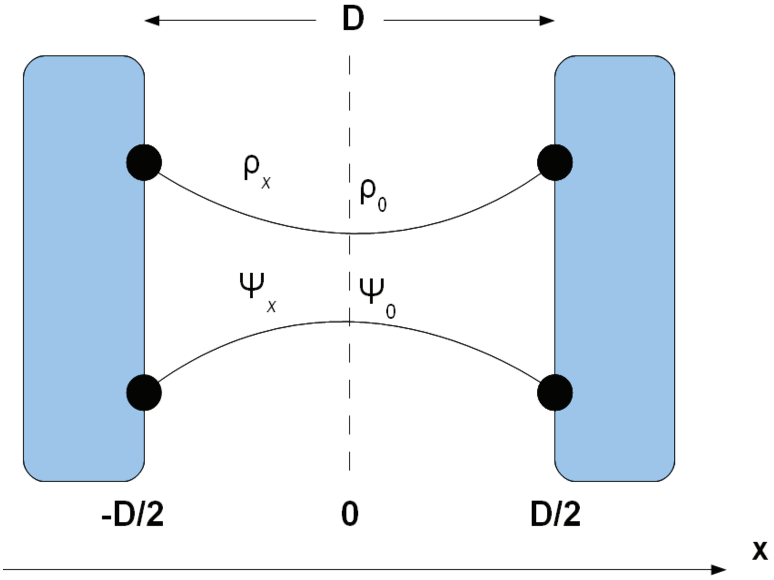

Figure 2.5: The counterion density profile ρ_x and the electrostatic potential ψ_x in the gap between two negatively charged surfaces.

opposite charge from the ions in the gap between the surfaces, i.e.

$$\sigma = -\int_0^{D/2} ze\rho \mathrm{d}x = \epsilon\epsilon_0 \int_0^{D/2} \frac{\mathrm{d}^2\psi}{\mathrm{d}x^2}\mathrm{d}x = \epsilon\epsilon_0 \left(\frac{\mathrm{d}\psi}{\mathrm{d}x}\right)|_0^{D/2} = \epsilon\epsilon_0 E_s. \tag{2.20}$$

This means that $E_s = \frac{\sigma}{\epsilon\epsilon_0}$, in other words, the electric field at the surface is given by the surface charge and the medium, and is independent of the gap distance D [23].

The ionic distribution between two surfaces

The ionic concentration at the midpoint is related to that at the surfaces. When differentiating Eq. 2.17 and using the PB equation,

$$\frac{\mathrm{d}\rho}{\mathrm{d}x} = -\frac{ze\rho_o}{k_BT}\exp\left(\frac{-ze\psi}{k_BT}\right)\frac{\mathrm{d}\psi}{\mathrm{d}x} = \frac{\epsilon\epsilon_0}{k_BT}\frac{\mathrm{d}\psi}{\mathrm{d}x}\frac{\mathrm{d}^2\psi}{\mathrm{d}x^2} = \frac{\epsilon\epsilon_0}{2k_BT}\frac{\mathrm{d}}{\mathrm{d}x}\left(\frac{\mathrm{d}\psi}{\mathrm{d}x}\right)^2, \tag{2.21}$$

one can see, after

$$\rho_x - \rho_0 = \int_0^x \mathrm{d}\rho = \frac{\epsilon\epsilon_0}{2k_BT}\int_0^x \mathrm{d}\left(\frac{\mathrm{d}\psi}{\mathrm{d}x}\right)^2 = \frac{\epsilon\epsilon_0}{2k_BT}\left(\frac{\mathrm{d}\psi}{\mathrm{d}x}\right)^2|_x \tag{2.22}$$

which leads to

$$\rho_x = \rho_0 + \frac{\epsilon\epsilon_0}{2k_BT}\left(\frac{\mathrm{d}\psi}{\mathrm{d}x}\right)^2|_x, \tag{2.23}$$

i.e. the number density at any point is given in terms of ρ_0, the midplane value, and $\left(\frac{\mathrm{d}\psi}{\mathrm{d}x}\right)^2$. Using $x = \pm\frac{D}{2}$ at the surfaces and the previously found surface value of the electric field, one obtains the surface value of the counterion density number:

$$\rho_s = \rho_0 + \frac{\sigma^2}{2\epsilon\epsilon_0 k_B T}. \tag{2.24}$$

How the potential and ionic concentrations vary away from a charged surface

The electrolyte ions of a solution containing charged surfaces have an important effect on the forces between the surfaces. To understand the double-layer interaction between two surfaces, the ionic distribution adjacent to the surfaces under consideration has to be determined. For an isolated surface in a solution containing an electrolyte, a situation which can represent two surfaces far enough apart from each other, we now set $x = 0$ at the surface. The relations previously derived are still valid for solutions containing different types of ions with valency $\pm z$, but this time the net charge density at x will be expressed as $\sum_i z_i e \rho_i$, and the total ionic number density, or concentration, as $\sum_i \rho_{xi}$ [23]. In doing so, the Boltzmann distribution from Eq. 2.17 becomes

$$\rho_{xi} = \rho_{\infty i} \exp \frac{-z_i e \psi_x}{k_B T}, \tag{2.25}$$

where $\rho_{\infty i}$ denotes the ionic concentrations of ion species i in the bulk at $x = \infty$, i.e. at a long distance away, where the presence of the surface is not felt because $\psi_\infty = 0$.
Then Eq. 2.23 can be written like

$$\sum_i \rho_{xi} = \sum_i \rho_{\infty i} + \frac{\epsilon\epsilon_0}{2k_B T}\left(\frac{\mathrm{d}\psi}{\mathrm{d}x}\right)^2. \tag{2.26}$$

In the case of a 1:1 electrolyte, like NaCl, this yields

$$\frac{\mathrm{d}\psi}{\mathrm{d}x} = \sqrt{\frac{8k_B T \rho_{\infty i}}{\epsilon\epsilon_0}} \sinh \frac{e\psi_x}{2k_B T}, \tag{2.27}$$

which through integration using the integral $\int \mathrm{csch} X \mathrm{d}X = \log\tanh X/2$ gives

$$\psi_x = \frac{2k_B T}{e} \log \frac{1 + \tanh\frac{e\psi_0}{4k_B T}\exp[-\kappa x]}{1 - \tanh\frac{e\psi_0}{4k_B T}\exp[-\kappa x]} \approx \frac{4k_B T}{e} \tanh \frac{e\psi_0}{4k_B T} \exp[-\kappa x]. \tag{2.28}$$

This is called Gouy-Chapman theory, and for high potentials the term $\tanh \frac{e\psi_0}{4k_BT} \rightarrow 1$, while it for low potentials reduces to the Debye-Hückel equation: $\psi_x \approx \psi_o \exp\left[-\kappa x\right]$ [23].

The double-layer interaction between two charged surfaces in electrolyte

The repulsive pressure P from the counterions at the position x from the centre is given by the relation $\left(\partial P/\partial x\right)_{x,T} = \rho\left(\partial \mu/\partial x\right)_{x,T}$ [23]. The chemical potential was given in Eq. 2.16, and using this calculating the change in pressure at x when bringing two plates together from far away, i.e. from infinity, to the separation $x' = D/2$, one obtains

$$P_x = -\int_{x'=\infty}^{x'=D/2} [ze\rho\left(\frac{\mathrm{d}\psi}{\mathrm{d}x}\right)_x \mathrm{d}x' + k_BT\mathrm{d}\rho_x], \tag{2.29}$$

where x' denotes the variable distance between the two plates. The term $ze\rho$ can be replaced using the Poisson equation, and when also using the mathematical relation

$$\frac{\mathrm{d}}{\mathrm{d}x}\left(\frac{\mathrm{d}\psi}{\mathrm{d}x}\right)^2 = 2\left(\frac{\mathrm{d}\psi}{\mathrm{d}x}\right)\left(\frac{\mathrm{d}^2\psi}{\mathrm{d}x^2}\right), \tag{2.30}$$

one finds that at any point x the pressure $P_x(D)$ is given by

$$P_x(D) - P_x(\infty) = -\frac{1}{2}\epsilon\epsilon_0\left[\left(\frac{\mathrm{d}\psi}{\mathrm{d}x}\right)^2\Big|_{x(D)} - \left(\frac{\mathrm{d}\psi}{\mathrm{d}x}\right)^2\Big|_{x(\infty)}\right] + k_BT\left[\sum_i \rho_{xi}(D)\right] - \sum_i \rho_{xi}(\infty). \tag{2.31}$$

Then, Eq. 2.23 is rewritten as

$$\sum_i \rho_{xi} = \sum_i \rho_{mi} + \frac{\epsilon\epsilon_0}{2k_BT}\left(\frac{\mathrm{d}\psi}{\mathrm{d}x}\right)^2\Big|_x \tag{2.32}$$

where $\sum \rho_{mi}$ is the total ionic concentration at the midplane where $x = D/2$. Because $P_x(D = \infty) = 0$, the uniform pressure across the gap can be written as

$$P_x(D) = k_bT[\sum_i \rho_{mi}(D) - \sum_i \rho_{mi}(\infty)]. \tag{2.33}$$

This pressure acts on the electrolyte ions and the surfaces [23]. For a 1:1 electrolyte this equation can be written as

$$P = k_BT\rho_\infty\left[\exp\frac{-e\psi_m}{k_BT} + 1 - \left(\exp\frac{+e\psi_m}{k_BT} + 1\right)\right] \approx \frac{e^2\psi_m^2\rho^2}{k_BT}. \tag{2.34}$$

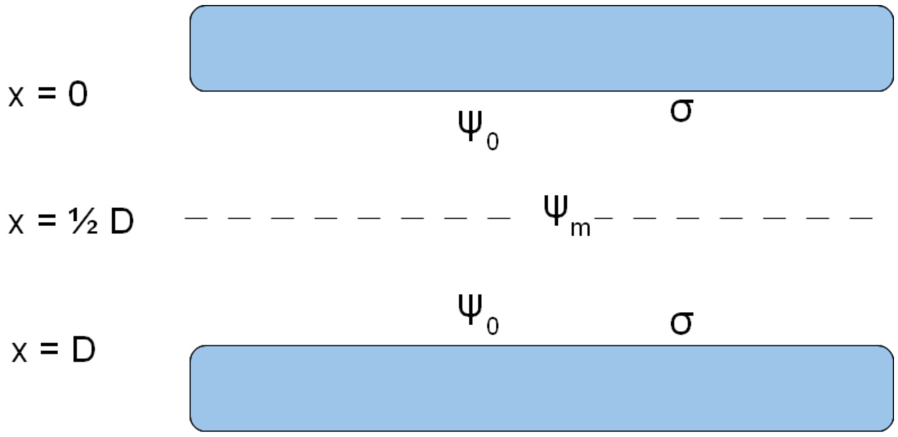

Figure 2.6: Two planar surfaces separated by a distance D. The solvent, containing ions, occupy the space between the surfaces.

Here, the first term in the bracket is due to the cations, while the second is due to the anions. Also, the midplane potential ψ_m is assumed to be the sum of the potentials from the two surfaces at the midplane. Then, finally, the pressure between two planar surfaces may be written as:

$$P = 64 k_B T \rho_\infty \tanh^2 \frac{ze\psi_0}{4k_B T} \exp\left[-\kappa D\right]. \tag{2.35}$$

The interaction free energy per unit area corresponding to this pressure can be found by integrating with respect to D, if wanted [23]. It should be stressed that the Poisson-Boltzmann equation is a mean-field theory, which means that it breaks down at small distances. In this regime, it can no longer describe the ionic distribution and forces between surfaces in a reliable way. If calculating that the distance between the charged surface and the double layer is very small, this fact should be kept in mind [23].

2.2.4 The total DLVO potential

When the electrostatic double layer interaction between two plates is added to the van der Waals forces acting between the same plates, the result is the so-called DLVO potential. The globally repulsive electrostatic forces are balanced by the attractive van der Waals

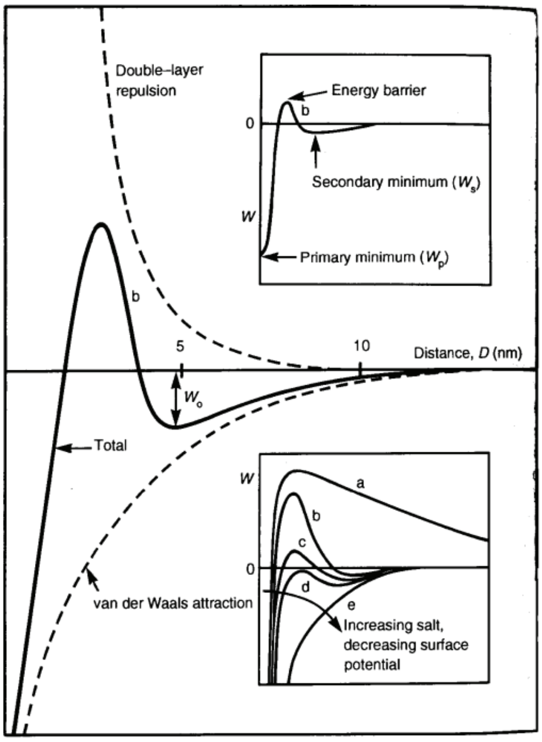

Figure 2.7: The total interaction energy versus distance calculated by means of the DLVO theory. The primary and secondary minimas are shown in the top inset, while the salt concentration effect on the potential profile is shown in the bottom inset. Figure from [23].

forces, thus creating a potential typically looking like the one in Figure 2.7. This theory has proved to be an effective way of describing the structure and stability of colloidal dispersions. The repulsion force between particles is strongest when the salt concentration is low, due to the screening effect being small. In this situation, the particles repel each other and continue their Brownian motion, and the dispersion is typically in a stable state [22]. When the salt concentration increases, the repulsive potential weakens. The consequence of this is that the particles could be having big enough thermal energy, of order k_BT, to fall into the primary minimum, thus leaving the particles strongly bound. This is an irreversible process called coagulation. However, there is another minimum, the secondary, which is very sensitive to the salt concentration. If the depth of this is larger than the thermal energy, the particles can flocculate and form colloidal crystallites. This flocculation process is reversible [22].

The DLVO theory is not universally accepted. It has some shortcomings, e.g. regarding salt-induced melting of colloidal crystals. For some range of salt-concentration, a transition from an ordered state to an unordered state has been observed upon increasing the salt concentration [17]. This observation can not be explained by the DLVO theory. However, the DLVO theory has proved to explain many aspects regarding colloidal dispersions, and is therefore regarded as a valuable tool when trying to understand such systems.

2.3 Liquid crystals

Liquids are always isotropic, i.e. in contrast to the case of crystals, their properties are not orientation dependent. That this is so is because the thermal motion has no orientational preference. Indeed while locally ordered structures are constantly formed, the alignment of the atoms, which form a shell around a particular atom, is completely arbitrary. For some molecules, an inner ordering spontaneously develops in the liquid phase such that a macroscopic anisotropy arises. Such molecules are called *nematogens* and the anisotropic phase is referred to as *nematic* [39].

2.3.1 Types of liquid crystals

There exist several liquid crystalline phases. Here, some of the most common phases will be discussed. In the case of rod-like molecules, the nematic phase is well-known. It materializes as a phase where the molecules, on average, point in a certain direction, whilst the centres of gravity of the molecules are evenly spread out. In other words, the nematic phase shows orientational anisotropy, but no positional anisotropy. The preferred orientation of the molecules is called the nematic director, which is a unit vector denoted $\vec{n}$. This orientation is not necessarily constant over the whole sample, but changes over macroscopic lengths. Physically, $\vec{n}$ determines the direction of the optical axis [39]. The nematic phase of a disc-like molecule, which can be considered as rod-like with the length L being much shorter than the diameter D, i.e. $L << D$, is illustrated in Figure 2.9.

Another common phase is the smectic phase, which has not only a directional anisotropy, but also a positional one. In the smectic phase the molecules tend to organize themselves in layers, as illustrated in Figure 2.10. In contrast to the case of nematogens, the class of molecules that are able to organize in a nematic manner, no

Figure 2.8: The microscopic order of the isotropic phase of a disc-like nematogen. There is no orientational or positional order.

significant technical use has been found so far for substances in the smectic phase [39].

Another phase is the *chiral nematic* phase. In this phase, the director field adopts, depending on the type, a left- or right-handed screw arrangement. For a more comprehensive review of the different liquid crystalline phases, see e.g. [4].

The phase behaviour of a liquid crystals depends primarily on temperature and concentration. If the temperature is the most important parameter, the liquid crystal is called *thermotropic*. On the other hand, if the concentration is more important, the liquid crystal is termed *lyotropic*. NaFh is the latter, as evident from Figure 2.4. However, in this thesis the aim is to investigate what role temperature may play, i.e. to what extent NaFh is a thermotropic liquid crystal as well as a lyotropic one.

2.3.2 The uniaxial ordering parameter

The nematic director $\vec{n}$ characterises, if any, the preferred direction of the molecules in a liquid. If the molecules are rodlike, it is the long axis which determines which way the molecules are oriented. Strobl introduces a function

$$w(\theta, \phi) \tag{2.36}$$

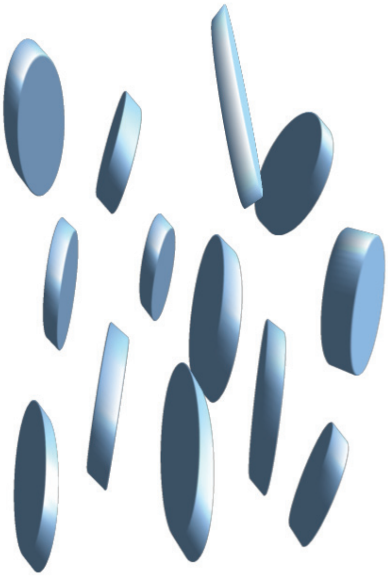

Figure 2.9: The microscopic order of the nematic phase of a disc-like nematogen. There is orientational order, but positional order is absent.

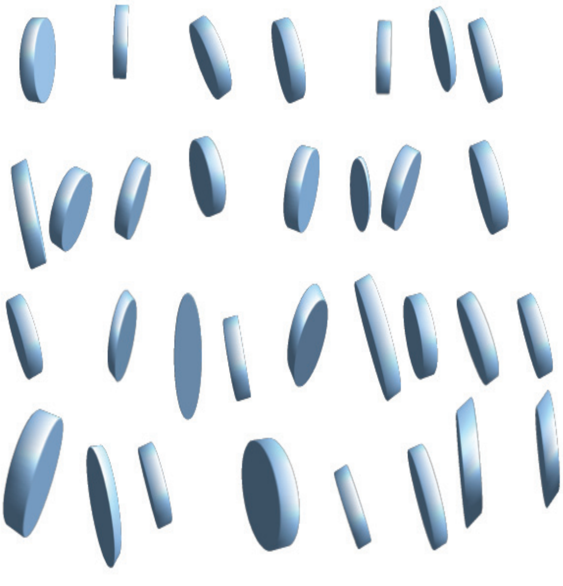

Figure 2.10: The microscopic order of the smectic phase of a disc-like nematogen. There is both orientational and positional order.

where

$$w(\theta, \phi) \sin(\theta) \mathrm{d}\theta \mathrm{d}\phi \tag{2.37}$$

gives the fraction of molecules whose long axis lay inside the the range of angles $\mathrm{d}\theta\mathrm{d}\phi$. If uniaxial symmetry is present, a function w' can be introduced, which is only dependent on θ. For a nematic phase, $w'(\theta) = w'(\pi - \theta)$. This means that $\vec{n}$ is not unique, it can also be chosen in the opposite direction. The $w'(\theta)$ can be expanded as a series of Legendre polynomials $P_l(\cos\theta)$

$$w'(\theta) = \sum_{l=0}^{\infty} \frac{1}{2}(2l+1) S_l P_l \cos\theta. \tag{2.38}$$

The Legendre polynomials are orthogonal to each other [39], i.e.

$$\int_0^{\pi} P_m(x) P_n(x) \mathrm{d}x = \frac{2}{2n+1} \delta_{mn} \tag{2.39}$$

Strobl shows that the series coefficient S_2 is very well suited to act as a nematic order parameter. S_2 describes the degree of orientation in a sample of rodlike molecules. For perfect orientation, $S_2 = 1$, while for isotropic orientation, $S_2 = 0$ [39]. It can be shown [39] that S_2 is proportional to the difference in refractive indexes, $\Delta n = n_{\parallel} - n_{\perp}$. Δn is often referred to as the effective birefringence.

The order parameter will usually vary from point to point in a liquid crystal, due to constraints imposed by limiting surfaces and external fields. The most important types of deformation is splay, bend and twist, shown in Figure 2.11. In a weakly distorted system[6], distorted states may be described in terms of a vector field [14].

2.3.3 Theoretical predictions of the nematic phase

The nematic phase has been predicted theoretically by different means. The Maier-Saupe theory states that the nematic phase is a result of a self-stabilizing process [39], and Onsager showed in 1949 that the nematic phase, for a rod-like nematogen, is an energetically favourable way to arrange the molecules [32]. Onsager tried to explain the isotropic-nematic phase transition by considering the competing effects of the orientational and the packing entropies of colloidal systems, and concluded that the packing entropy would dominate at high particle concentrations, thus making it favourable for the particles to give up orientational entropy for positional entropy. Onsager's proposition has later been confirmed by computer

---

[6] That is, a system where the order parameter changes significantly over distances much larger than the molecular dimensions.

simulations showing that systems of plate-like particles indeed can develop nematic ordering [8, 41]. The analytical results obtained for monodisperse platelets, with only short-range interactions taken into account, can not be expected to be equally valid for the highly irregularly shaped and polydisperse NaFh-platelets. In addition to the differences due to the irregular form, the long-range interactions from the surface charge of the platelets further complicates analytical treatment for the case of fluorohectorite.

2.3.4 The optics of liquid crystal textures

The texture of a liquid crystal between two substrates is a complicated, inhomogeneous distribution of the director, which can include defects. The texture is usually observed under the microscope. This does not give direct access to director data, but if the sampled is placed between crossed polarisers, colours and zones of different intensity can be seen. This results from the fact that the nematic director, and hence the optical axis, is varying over the sample. In conventional polarising microscope observations, the main challenge is interpreting the images in the 'language' of liquid crystal physics to determine the texture, hence the local orientation of the director [37].

In a uniform state, a liquid crystal has a structure characterised by position-independent order parameters. In real experiments, constraints like surfaces and external fields will affect the molecules, and the liquid crystal structure becomes deformed. Deformations cost energy, as they are accompanied by restoring forces opposing the deformations. The constant of proportionality between a deformation and its restoring force is called an elastic constant. In a solid crystal, the material undergoes homogeneous strain under deformation and a restoring force arises to oppose the change in distance between neighboring points. In a positionally disordered system, like a liquid, this can not happen. However, if the material is orientationally ordered, restoring forces may arise to oppose the orientational deformations. Liquid crystals influenced by external fields exhibit phenomena usually distinguished by the following characteristics [37]:

- The energy involved per molecule in producing these effects is small compared to the strength of intermolecular interaction.

- The characteristic distances involved in these phenomena are large compared to molecular distances.

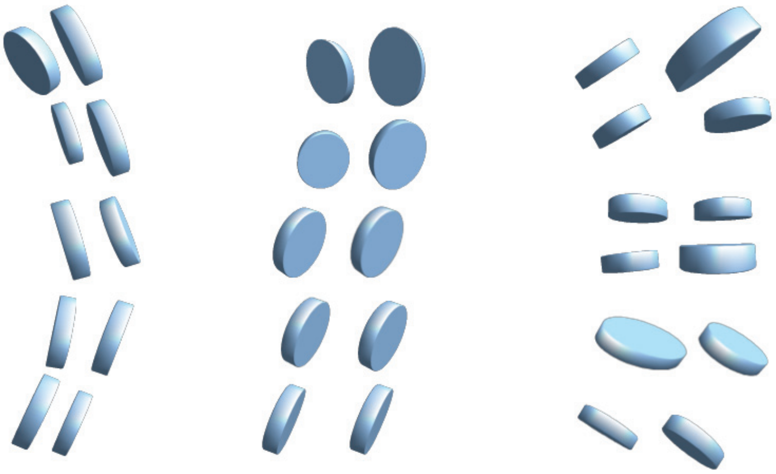

Figure 2.11: The three basic distortions modes of disc-like liquid crystal molecules. From left to right: splay, twist and bend.

When describing long distance phenomena like these, it is convenient to regard the liquid as a continuum with a set of elastic constants rather than on a molecular basis. The elastic constants appear in the description of virtually all phenomena where the variation of the director is manipulated by confinements and external fields. The elastic constants are related to the three fundamental modes of distortion in a liquid crystal: splay, twist and bend. These distortions are shown in Figure 2.11. The elastic constants also provide unusually sensitive probes of the microscopic structure of the ordered state. Knowledge of the elasticity of liquid crystals is also necessary for the study of order parameter fluctuations and defect stability in them.

2.3.5 Polarised light

A normal beam of light in an isotropic material consists of many individual waves, each vibrating in a direction perpendicular to its path, as illustrated in Figure 2.12. Measureable intensities therefore refer to a superposition of many millions of waves. Normally, the vibrations of each ray have different orientations with no favoured direction. In some cases, however, all the waves in a beam vibrates in the same direction. Such light is said to be polarised, i.e to have a directional characteristic. More specifically, it is linearly polarised, to distinguish it from circularly and elliptically polarised light. Light from familiar sources, like the Sun or a light bulb, is unpolarised, but can easily become polarised as it interacts with matter. Reflection,

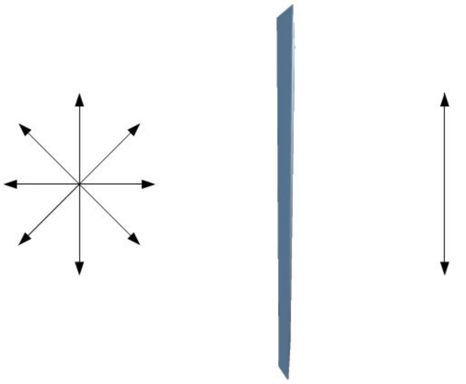

Figure 2.12: The electric field of unpolarised light, to the left, vibrates in every direction perpendicular to its path. After passing through the polariser, the light becomes linearly polarised, i.e. the electric field vibrates in one particular direction. The light travels from left to right. The $\vec{E}$ fields are seen directly from behind.

refraction, transmission, and scattering all can affect the state of polarisation of light [37].

Polarisers

Polarisers are essential elements for optical studies of liquid crystals. The most widely used material is the Polaroid film [37]. It selectively absorbs light from one plane, typically transmitting less than 1 %. It may transmit more than 80 % of light in the perpendicular plane. The word 'Polaroid' usually refers to a polariod H-sheet, which is a sheet of iodine-impregnated polyvinyl alcohol [37]. A sheet of polyvinyl alcohol is heated and stretched in one direction while softened, which has the effect of aligning the long polymeric molecules in the direction of stretch. When dipped in iodine, the iodine atoms attach themselves to the aligned chains. Light waves with electric fields parallel to these chains are strongly absorbed because of dissipative effects of the electron motion in the chains. The direction perpendicular to the polyvinyl alcohol chains is the 'pass' direction [37]. For practical purposes, it suffices to say that a linear polarizer provide linearly polarised light when unpolarized light is sent through it.

Transmitted intensity between crossed polarisers

There are two polarising filters in a polarising microscope or camera set-up: the polariser and the analyser. The polariser is situated before the specimen stage, usually with its permitted vibration direction rotable through 360°. The analyser is placed on the other side of the specimen, and can in the same way be rotated a full 360°. Under standard observation conditions, when both the analyser and the polariser is in the optical path, they are usually positioned with their permitted vibration directions at right angles to each other. They are said to be *crossed*. No light passes through the system and a dark field of view is present in the eyepieces or at the position of the camera. If an anisotropic specimen illuminated by white light is viewed with the crossed polarisers off the extinction position, colours, known as interference colours, will be seen. These colours result from unequal transmission by the analyser of the various components of white light. What wavelengths are seen depends on the retardation or path difference produced in the crystal for each of the wavelengths. To understand colour generation it is sufficient to discuss the case of uniaxial materials [37]. The basic equation for light transmittance of uniaxial anisotropic materials between crossed polarisers reads

$$I = \frac{I_0}{2} \sin{(2\phi)}^2 \sin\left(\frac{\pi \Delta n(\lambda) d}{\lambda}\right)^2 . \qquad (2.40)$$

Here $\Delta n(\lambda)$ is the effective birefringence of the material under observation, λ is the wavelength of light, d is the thickness of the sample, and ϕ is the angle that the optical axis of the uniaxial material makes with the polariser [37].

2.3.6 Wall alignment

It is well known that the bulk alignment of a liquid-crystal film can be controlled by surface treatment [14]. This is technologically important, e.g. it is essential for the construction of liquid crystal display devices, where a combination of surface alignment and an externally controlled electric field is responsible for which pixels turn out light or dark.

Near the walls, the molecules tend to arrange themselves with the nematic director either parallel or orthogonal to the walls. These wall arrangements are referred to as planar and homeotropical alignment, respectively. It is possible, by treating the surface of the walls, to obtain planar or homeotropical alignment [14].

The effects of wall alignment for NaFh in saltwater solutions have been investigated [21]. It was found from analyzing small-angle scattering x-ray (SAXS) diffractograms that the platelets lie face against wall.

2.3.7 The liquid crystalline nature of saline solutions of NaFh

It has been mentioned that the gravitational settling of saline solutions of sodium-fluorhectorite results in a rich phase behaviour. An example of the time evolution of such a solution is shown in Figure 2.13. Immediately after preparing the solution, there is no order of the platelets. However, this changes rapidly, as evident from the figure. For this 2 w/w% NaFh, and 10 mM salt solution, the largest particles sediments rapidly during the first hours. After a week, a nematic phase starts to appear above the sediment. In the latter stages of the evolution shown in this picture, at least four distinct phases are visible: The sediment at the bottom, two nematic phases on top of each other and, on top, an isotropic phase.

2.4 X-rays

X-rays are electromagnetic waves, exhibiting the wave-particle duality. When referring to x-rays as particles, the particles are usually called *photons*. In this text, the wave nature of the x-rays will be given most attention.

The scattering of x-rays by atoms, ions and electrons can only be correctly described by a quantum mechanical treatment, particularly at short wavelengths, as was demonstrated by Compton [5]. However, for the purpose of this thesis, a classical approach is sufficient.

Wilhelm Röntgen discovered in 1895 that a screen coated with barium platino-cyanid fluoresced near a discharge tube, even when a shield opaque to light was between the tube and the screen [30]. He traced this effect to some unknown radiation, which he called x-rays. The x-rays came from a spot on the wall of the discharge tube, opposite to the cathode, which had a greenish glow under high vacuum. The glow was caused by radiation from the cathode, which he called cathode rays. Later, it was realised that these rays consisted of electrons. Röntgen studied the newly discovered x-rays, and was able to describe many properties of the x-rays in a paper. He found that [30]

1. All substances are transparent to x-rays, but to different degrees. A thick book was a scarcely noticable hindrance, wood somewhat more opaque, while aluminum weakened the intensity of the rays considerably. He also found that bones in the hand had different transparancy from that of the tissue around,

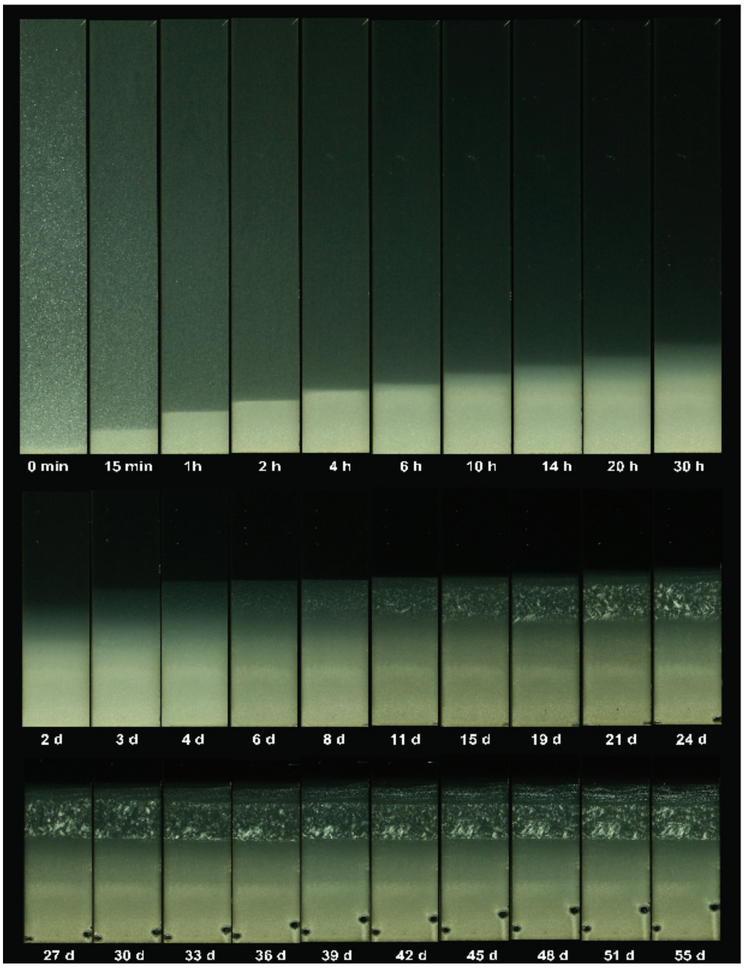

Figure 2.13: The time progress of 55 days for a 2 w/w% uncrushed NaFh powder at 10^{-3} M salt concentration. The solution sediments very rapidly during the first hours after preparation. After two days, a second sedimentation layer forms above the first sediment. Around two to four days a new layer has settled above the sediment. This layer is considered to be more or less isotropic. After six days some birefringence is beginning to appear in the isotropic phase, and over the following days, a transition from isotropic to nematic ordering takes place. Eventually, after around 27 days, another nematic phase is formed above the first one. Retrieved from [35].

which has of course had huge impact in the medical science.

2. Other compounds, like calcite, uranium glass, rock salt etc., fluoresce as well.
3. Photographic films are susceptible to x-rays, making them valuable tools in order to record the effects.
4. X-rays did not refract or reflect to a degree that he could measure, meaning that the index of refraction could not be higher than 1.05.
5. X-rays are not deflected by magnetic fields, and are therefore not charged.
6. X-rays are generated when cathode rays hit a solid body, with the tendency of heavier elements being more efficient than lighter ones.
7. Charged bodies in air are discharged if x-rays fall upon them.

Röntgen discovered the x-rays using a primitive vacuum tube. He used a pear-shaped glass tube with two conducting terminals, called the anode and cathode, respectively. Across these terminals, a large induction coil was connected, and as a result, the residual gas provided some electrons and some positive ions. The ions accelerated towards the cathode, which in turn emitted electrons. These electrons were then attracted to the anode, from which the x-rays eventually emitted.

X-rays interact by elastic and inelastic scattering and by photoelectric absorption, the relative amount of each being material and wavelength dependent. Two processes contribute to elastic scattering: Thomson scattering which occurs from single atomic electrons which may be considered to be free, and Rayleigh scattering which is a coherent process occuring from strongly bound electrons. Inelastic scattering, also called Compton scattering, occurs from loosely bound electrons and involves a transfer of energy from the incident x-ray photon. Photoelectric absorption occurs when an x-ray photon tranfer its energy to a bound atomic electron, ionising the atom. The cross section for this process has a series of jumps at absorption edges, where the x-ray has sufficient energy to remove an electron from a particular atomic energy level [30].

2.4.1 Crystals

To describe the structure of matter can be a difficult task. However, the description of crystalline structures is simplified because

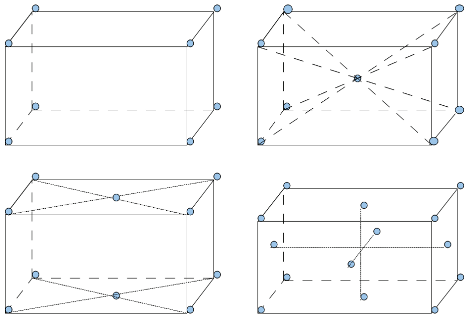

Figure 2.14: Various unit cells. From the top left corner and following the clock: Primitive (P), body-centred (I), face-centred (F) and at the centre of opposite faces, i.e. side-centred (C).

the crystal has translational periodicity, i.e. a crystal looks the same if it is translated a certain length in some direction. This will be presented in a more mathematical way shortly. A perfect 3D crystal, obviously a mathematical construction, can be generated by assigning each point in an appropriate lattice with the same basis, i.e. an atom or a group of atoms. A lattice in this context can be thought of as an infinite array of mathematical points in 3D space. Such a lattice has the translational periodicity characteristic of a crystal. In order to describe the lattice, one needs only three vectors, namely the fundamental vectors of the given lattice. These will be termed $\vec{a}$, $\vec{b}$ and $\vec{c}$. In this way, it is possible to connect two lattice points by a translation vector

$$\vec{R} = u\vec{a} + v\vec{b} + w\vec{c}, \tag{2.41}$$

where u, v and w are integers. The translation vectors can be chosen in many ways, but those for which Eq. 2.41 is valid are called primitive. The geometric object spanned by the primitive axis is termed the unit cell, and its volume is given by

$$V = \vec{a} \cdot (\vec{b} \times \vec{c}). \tag{2.42}$$

There exists a variety of unit cells, depending on the relative positions of lattice points within the cell. For example, there can be lattice points only at the corners, in which case the cell is termed primitive (P). Other examples include lattice points in the centre of the cell (I), at the centre of opposite faces (C) and at the centre of all faces (F), see Figure 2.14. The variables that can be altered when constructing a unit cell is the lengths of the fundamental vectors, and the angles between them, see Figure 2.15. There are fourteen

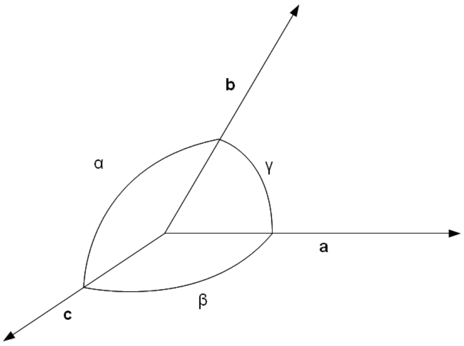

Figure 2.15: The relationships between the unit-cell vectors $\vec{a}$, $\vec{b}$ and $\vec{c}$ and the intervector angles α, β and γ.

Table 2.1: The seven 3D crystal systems and properties of their unit cells.

Crystal system	Unit-cell coordinates	Bravais lattices
Cubic	$a = b = c$; $\alpha = \beta = \gamma = 90^\circ$	P, F, I
Tetragonal	$a = b \neq c$; $\alpha = \beta = \gamma = 90^\circ$	P, I
Orthorombic	$a \neq b \neq c$; $\alpha = \beta = \gamma = 90^\circ$	P, F, I, C
Hexagonal	$a = b \neq c$; $\alpha = \beta = 90^\circ$, $\gamma = 120^\circ$	P
Trigonal	$a = b \neq c$; $\alpha = \beta = 90^\circ$, $\gamma = 120^\circ$	P
Monoclinic	$a \neq b \neq c$; $\alpha = \beta = 90^\circ$, $\gamma \neq 90^\circ$	P, C
Triclinic	$a \neq b \neq c$; $\alpha \neq \beta \neq \gamma$	P

3D crystal lattices with different symmetries, and they are called the Bravais lattices [7]. These can be subdivided into seven crystal systems, each of which have one or more different types of unit cells, see table 2.1.

To understand the structure of matter, one need to know the atomic positions, usually in three dimensions. Crystal structures, for example, can be characterized in terms of lattice-translation vectors $\vec{R}_{uvw}$ of the Bravais lattice. Then $\vec{R}_{uvw} = u\vec{a} + v\vec{b} + w\vec{c}$, where u, v and w are integers and $\vec{a}$, $\vec{b}$ and $\vec{c}$ can be vectors defining the unit cell.

Nomenclature of crystal directions and planes

When referring to a vector direction in a crystal, or to a plane of atoms, a convention which is general and valid for all crystal types is needed. For the directional case, consider a vector $\vec{z}$, which connects the origin O with a point P, see Figure 2.16. This vector makes projections u', v' and w' on the unit cell axes $\vec{a}$, $\vec{b}$ and $\vec{c}$, respectively. When u', v' and w' are divided by the highest common denominator, they are reduced to a set of smallest integers, namely u, v and w. The direction of $\vec{z}$ is then denoted $[u\ v\ w]$. Should the projection

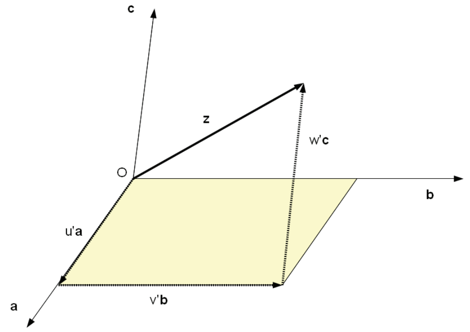

Figure 2.16: A representation of the directions in a crystal. The vector $\vec{z}$ makes projections on the unit cell axes $\vec{a}$, $\vec{b}$ and $\vec{c}$ of u', v'and w', respectively.

of $\vec{z}$ along a unit cell axis be negative, the corresponding integer will be distinguished by a bar on top, e.g. $\bar{u}$. A complete set of equivalent directions in a crystal is denoted $<uvw>$. For a cube crystal system this means that the edges of the cube can be described as the complete set <100>.

Atomic planes in crystals are labelled in a similar way. A general plane intersecting the unit cell axes at $u'\vec{a}$, $v'\vec{b}$ and $w'\vec{c}$, see Figure 2.17. The reciprocals $1/u'$, $1/v'$ and $1/w'$ are then transformed to the three smallest integers possible, denoted h, k and l. They have of course the same ratios. The plane would then be denoted as (h k l). E.g. if a plane intersected the unit cell axes at the three points [400], [020] and [003], the reciprocals would be 1/4, 1/2 and 1/3 respectively. The smallest three integers having the same ratios are then 3, 6 and 4, meaning that the plane is denoted (3 6 4). In the same way there was complete sets of equivalent directions, there are sets of equivalent planes. Again, the cube faces serve well as an example. The top side of a cube is denoted (0 0 1), and the set of equivalent planes is denoted $\{\ h\ k\ l\ \}$, and include the other five faces (1 0 0), (0 1 0), ($\bar{1}$ 0 0), (0 $\bar{1}$ 0) and (0 0 $\bar{1}$). For cubic crystal systems, the direction of [h k l] is orthogonal to the plane (h k l). It is not necessarily so for the other crystal systems [7]. The system of indexing, which is called the Miller-index system, makes it easy to calculate the spacings between adjacent planes. This distance is important when it comes to diffraction of x-rays, as we will see later in section 2.4.2. For a cubic crystal system with unit-cell dimension a, the spacing d_{hkl} between the planes[7] $\{\ h\ k\ l\ \}$ is given as

$$d_{hkl} = \frac{a}{\sqrt{h^2 + k^2 + l^2}}. \tag{2.43}$$

---

[7] In order to be precise, I point out that I mean between two adjacent planes with parallel normals.

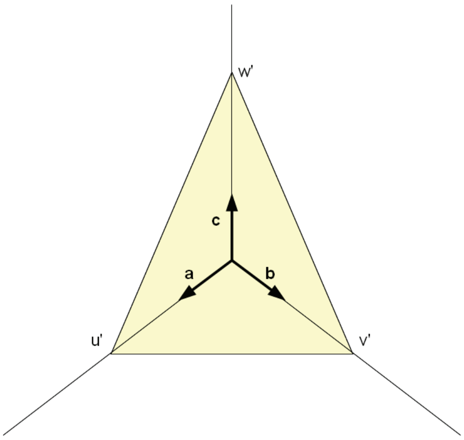

Figure 2.17: A representation of an atomic plane in a crystal. The plane intersects the unit cell axes at *u*', *v*'and *w*', respectively. The reciprocal quantities are converted into the smallest possible set of integers, which are then used to denote the plane (hkl).

2.4.2 Bragg's law

To understand the physical behaviour of a material, it is vital to have some knowledge of its atomic structure. For crystalline materials, the structure can be determined by means of diffraction experiments. For materials with a larger degree of disorder, diffraction can at best give partial information about the structure. It is then necessary that other experimental methods can provide further information in order to determine the structure. As we saw in section 2.3, in the case of NaFh, optical birefringence experiments is one such complementary method.

When waves meet an obstacle, they can diffract, leading to interference. The pattern created by the interference is a result of the constructive and destructive interference of wavefronts originating from different parts of the obstacle that causes the diffraction. The pattern can be interpreted to give information of the structure of the diffracting material. In general, diffraction is most effective when the wavelength of the incident radiation is comparable to the size of the diffractive object [7].

An equation that can be used to find the distance between two atomic planes can be found by assuming that the x-rays (or possibly other waves, like neutrons or electrons) reflect specularly from such planes. Constructive and destructive interference occurs when the path difference between two rays, i.e. $2d\sin\theta$, equals an integer

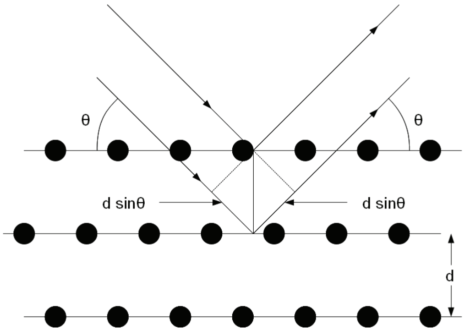

Figure 2.18: Bragg diffraction: The incident rays diffract from lattice planes of spacing d, subtending an angle of 2θ. The path difference between the two rays is, as indicated, $2d\sin\theta$.

number of wavelengths:

$$2d\sin\theta = n\lambda, \tag{2.44}$$

where θ is the angle of reflection. Hence is the angle subtended by the incident and the diffracted rays 2θ, as illustrated in Figure 2.18.

2.4.3 Reciprocal space

As we have seen, the structure of a solid can be discussed in terms if the atomic positions of the solid. Crystal structures, for example, can be characterized by lattice-translation vectors $\vec{R}_{uvw}$ of the Bravais lattice, that is

$$\vec{R}_{uvw} = u\vec{a} + v\vec{b} + w\vec{c} \tag{2.45}$$

where u, v and w are integers, and $\vec{a}$, $\vec{b}$ and $\vec{c}$ are the vectors defining the unit cell. Now, it is possible to describe this crystal structure by other means. One could wonder why this is necessary, but the structural description soon to be discussed has proven to be very useful. Instead of a description using atomic positions, associated with lattice points, it is convenient to the describe the same structure in terms of crystal planes. In a structure where all lattice points can be constructed by starting with one lattice point, and then adding lattice points at all combinations of u, v and w (from Eq. 2.41), that is at every lattice-translation vector $\vec{R}_{uvw}$, it is intuitively obvious that it is possible to construct a plane from any three lattice points, and that these three lattice points are not in any way the only lattice points which lies in that very plane.[8] Now, this plane has

---

[8] If one consider point 1, 2 and 3, and calls the translational vectors between the points $\vec{R}_{12}$, $\vec{R}_{13}$ and $\vec{R}_{23}$ it should be noted that the plane containing all points will not be unambiguously

a normal vector $\vec{n}_{hkl}$. However, there are other planes that share this normal vector as well. Such a plane can easily be found, e.g. by means of translating all the points constituting one plane the same distance in the same direction. This plane will obviously have the same normal vector as the previous plane. The process can be repeated as many times as one which, and this means that there are infinitely many planes that share the same normal vector (at least in an infinite crystal). The shortest spacing between two planes sharing the direction of their normal vectors is called d_{hkl}. Now, it can be proved that the entire crystal structure can be described in terms of the set of values $\vec{n}_{hkl}, d_{hkl}$[7]. To describe a crystal structure like this is not very useful, but a more useful representation can be found by defining the vector

$$\vec{G}_{hkl} = 2\pi \frac{\vec{n}_{hkl}}{d_{hkl}}. \tag{2.46}$$

These vectors define the so-called reciprocal space, and have the dimension of inverse length. They are central when it comes to understanding diffraction by crystals of waves. In this way, we now seen that a crystal structure has both a real-space lattice and a reciprocal lattice, both an equally valid description of the structure. Each point in the reciprocal lattice correspond to a family of planes in the real-space lattice. It should be noted that these crystal planes do not necessarily correspond to real atomic planes in the real-space structure.

Another way of defining the reciprocal lattice vector $\vec{G}_{hkl}$ is in terms of the basis vectors $\vec{a}^*$, $\vec{b}^*$ and $\vec{c}^*$ of the reciprocal lattice, i.e.

$$\vec{G}_{hkl} = h\vec{a}^* + k\vec{b}^* + l\vec{c}^*. \tag{2.47}$$

The vector $\vec{a}^*$ is given in terms of the real-space basis vectors

$$\vec{a}^* = 2\pi \frac{\vec{b} \times \vec{c}}{\vec{a} \cdot (\vec{b} \times \vec{c})}, \tag{2.48}$$

and the corresponding expressions for $\vec{b}^*$ and $\vec{c}^*$ are given by cyclic permutation.[9] The following relationships between the real-space and the reciprocal lattice vectors follows as an immediate consequence:

$$\vec{a} \cdot \vec{a}^* = 2\pi \tag{2.49}$$

---

given if all vectors are parallel and/or anti-parallel.

[9] This means that $\vec{b}^*$ can be found by utilizing the expression for $\vec{a}^*$, and replacing $\vec{a}$ with $\vec{b}$, $\vec{b}$ with $\vec{c}$, and finally $\vec{c}$ with $\vec{a}$.

and

$$\vec{a} \cdot \vec{b}^{*} = 0, \tag{2.50}$$

i.e. the vector product of one real-space and one reciprocal lattice vector is 2π if the vectors are reciprocal of each other, and zero otherwise.

Now the vector product of the real-space lattice-translation vector $\vec{R}_{uvw}$ and the reciprocal lattice $\vec{G}_{hkl}$ becomes

$$\vec{R}_{uvw} \cdot \vec{G}_{hkl} = 2\pi(hu + kv + lw), \tag{2.51}$$

and one can then state that some vector $\vec{k} = k_1\vec{a}^{*} + k_2\vec{b}^{*} + k_3\vec{c}^{*}$ in reciprocal space is a reciprocal-lattice vector if

$$\exp\left[i\vec{k} \cdot \vec{R}_{uvw}\right] = \exp\left[i\vec{G} \cdot \vec{R}_{uvw}\right] = 1. \tag{2.52}$$

This happens when the coefficients k_i are integers, and in this case $\vec{k}$ is a reciprocal-lattice vector.

The Laue formulation of diffraction

We have already seen that a vector $\vec{k}$ in reciprocal space is a reciprocal-lattice vector if $\exp[i\vec{k} \cdot \vec{R}_{uvw}] = 1$. Now, a collimated, monochromatic beam is considered, incident on an object from which is diffract. Von Laue assumed that each site, e.g. in the Bravais lattice of a crystal, would radiate the incident radiation in all directions, at the same frequency. This would then be generating constructive interference in specific directions. If the incident beam is represented as a plane wave, written as $\exp[i\vec{k}_1 \cdot \vec{r}]$, and the diffracted beam as $\exp[i\vec{k}_2 \cdot \vec{r}]$, where $\vec{k}_1$ and $\vec{k}_2$ are the respective wavevectors, another vector $\vec{q}$ can be constructed. This vector is often called the scattering vector, and relates to vector $\vec{k}_1$ and to $\vec{k}_2$ according to

$$\vec{q} = \vec{k}_2 - \vec{k}_1. \tag{2.53}$$

In other words, the scattering vector is simply the difference between the diffracted and the incident wavevectors, see Figure 2.19. If the scattering is to considered elastic, which is a *very* good approximation when it comes to x-rays, no energy is exchanged between the scatterer and the wave. Then $|\vec{k}_1| = |\vec{k}_2| = \frac{2\pi}{\lambda}$, and from geometrical considerations it become clear that the magnitude of the scattering vector is given by

$$\vec{q} = \frac{4\pi}{\lambda}\sin\theta. \tag{2.54}$$

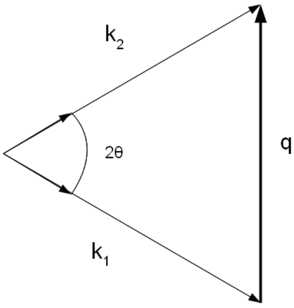

Figure 2.19: The scattering vector $\vec{q} = \vec{k}_2 - \vec{k}_1$.

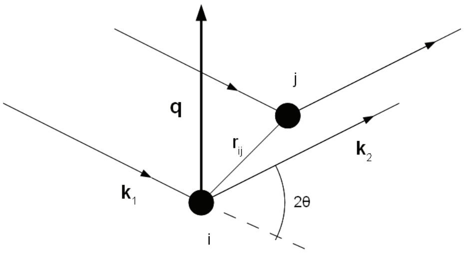

Figure 2.20: The path difference from two scattering centres i and j, separated by the distance $\vec{r}_{ij}$. The incident wavevector $\vec{k}_1$, the diffracted wavevector $\vec{k}_2$ and the scattering vector $\vec{q}$ are all shown.

2.4.4 Scattering theory

A large number of methods can be utilized in order to investigate condensed matter. Of particular importance are methods which involves scattering experiments. These are extensively applicable and requires no special preparation procedures. Even though particles like neutrons or electrons can be used, such experiments are usually undertaken using electromagnetic radiation. The same principal set-up is employed in all cases, see Figure 2.21. The incoming radiation is generated in a radiation source and characterised by a frequency ω, a wavevector $\vec{k}$ and an intensity I_0. This radiation hits the sample, and interactions between the radiation and the sample generates spherical scattering waves. The resulting intensity I, measured by a detector D a distance R away from the sample, generally depends on the observation direction. The change in angle upon scattering is expressed as 2θ, where θ is referred to as the Bragg scattering angle. In order to obtain information about the microscopic strucure of a sample, it is necessary to use a wavelength of the employed radiation of the same, or nearly the same, order of magnitude as the length-scale of the sample under investigation [39]. The information of the sample structure can be extracted from the change in intensity as the observation direction changes. The changes result from the interference of the scattered waves arising from the different particles in the sample.

Monochromatic radiation is usually employed in x-ray scattering experiments [39]. The incoming radiation can be described as a plane wave of amplitude E_0:

$$E_0 \exp\left[i(\vec{k}\cdot\vec{r}-\omega t)\right]. \tag{2.55}$$

This wave hits the particles, atoms or molecules, and excites dipolar vibrations. The interference of scattered waves from two particles at different locations is illustrated in Figure 2.20. If the sample-to-detector distance is large compared to the sample diameter, the wavevectors of the two scattered waves are parallel. In general, there will be a phase shift between the scattered waves from the particles. The phase delay of the scattered wave from particle 2 is given by

$$i\Delta\phi_2 = i\vec{r}_2(\vec{k}_1-\vec{k}_2) \tag{2.56}$$

Strobl shows that the amplitude of the electric field at the detector follows the equation

$$E'(\vec{q}) \propto \sum_j f_j \exp\left[-i\vec{q}\cdot\vec{r}_j\right], \tag{2.57}$$

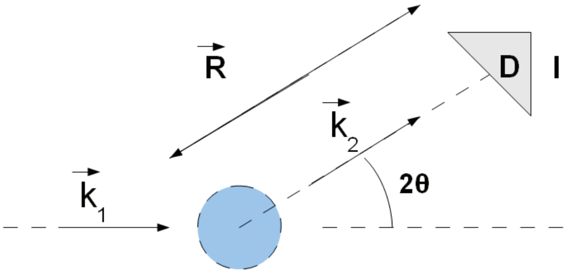

Figure 2.21: Principal set-up for a scattering experiment. The detector D measures the scattered intensity I at a distance R from the sample.

where the scattering vector

$$\vec{q} = \vec{k}_2 - \vec{k}_1 \tag{2.58}$$

is the decisive variable as regards the result of the scattering experiment. f_j is the atomic or molecular form factor. The detector measures intensity, not the amplitude of the electric field. The relation between the amplitude and the intensity is

$$I(\vec{q}) = \left\langle \left| E'(\vec{q}) \right|^2 \right\rangle \propto \left\langle \sum_{j,k} f_j f_k \exp\left[-i\vec{q}(\vec{r}_j - \vec{r}_k)\right] \right\rangle , \tag{2.59}$$

where the triangular brackets denotes time-average. Time-averaging is necessary as the experimental measurements require a finite amount of time, and because the particles in the sample, in general, are moving, so that the scattered intensity also fluctuates over time. In diffraction experiments where the sample consists of only one type of particles, the atomic or molecular form factors f_j are all the same and do not need to be considered further. Now, only the sum over all phase terms is important

$$C(\vec{q}) = \sum_j \exp\left[-i\vec{q} \cdot \vec{r}_j\right], \tag{2.60}$$

and the following equation holds for the scattered intensity:

$$I(\vec{q}) \propto \left\langle \left| C(\vec{q}) \right|^2 \right\rangle . \tag{2.61}$$

The scattered intensity is proportional to the number of scatterers in the sample, N, and it can be useful to introduce the reduced function

$$S(\vec{q}) = \frac{1}{N} \left\langle \left| C(\vec{q}) \right|^2 \right\rangle = \frac{1}{N} \sum_{j,k}^{N} \left\langle \exp\left[-i\vec{q}(\vec{r}_j - \vec{r}_k)\right] \right\rangle . \tag{2.62}$$

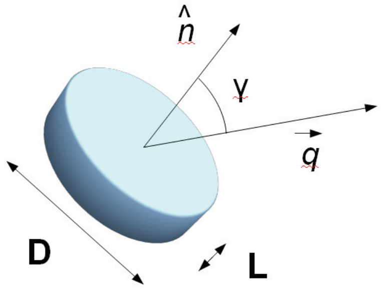

Figure 2.22: A model platelet of length L and diameter D. γ is the angle between the scattering vector q and the normal of the disc $\vec{n}$.

The function $S(\vec{q})$ is a well-defined function, and appears in the literature under names as e.g. the interference function, the scattering function or the structure function. Because the atomic and molecular form factors are no longer included in the expression, it follows that the type of radiation used is no longer relevant. It needs only to be considered in the evaluation of experimental data [39].

Power decay in a model platelet system

The form factor $P(q)$ of a cylinder, whose characteristics is given by the length L and the diameter D, is given as [10, 16]

$$P(q,\gamma) = \rho V \frac{\sin(w)}{w} \frac{2J_1(x)}{x}, \tag{2.63}$$

where

$$w = qL\cos\gamma/2 \tag{2.64}$$

Table 2.2: Expected power-law behaviour of a model platelet system. Inspired by [10].

Non-interacting monodisperse discs	Low q	Medium q	High q
Randomly oriented		q^{-2}	q^{-4}
Highly oriented $\vec{q} \perp \vec{n}$		q^{-3}	q^{-3}
Highly oriented $\vec{q} \parallel \vec{n}$			q^{-2}

and

$$x = q\frac{D}{2}\sin\gamma. \tag{2.65}$$

γ is the angle between the scattering vector $\vec{q}$ and the normal of the disc $\vec{n}$. V is the volume of the cylinder, ρ is the electronic density difference between the particle and the medium, and J_1 denotes the first order Bessel function of the first kind. If one assume that the particles do not interact, the structure factor $S(q)$ can be neglected, i.e. set to 1. Such a simplification of the calculation is not expected to be totally valid; nevertheless, the calculation should be able to point out important properties of such a system. In a monodisperse system, where discs are all of the same size, the scattered intensity can be written

$$I(q) = K\left\langle |P(q)|^2 \right\rangle_\gamma, \tag{2.66}$$

where K is an experimental constant and $\langle\rangle_\gamma$ means averaging over all orientations. For thin platelets, i.e. $D >> L$, the term in x in Eq. 2.63 falls off much faster than the term dependent on w. Then only small values of x will contribute to the average. Thus Eq. 2.66 can be written as

$$I(q)_{\text{isotropic}} \approx KA\frac{2\pi}{q^2}\left(\frac{\sin(qL/2)}{qL/2}\right)^2. \tag{2.67}$$

The scattered intensity can be seen to obey a q^{-2} power law. In the limit of high q the scattered intensity obeys a q^{-4} power law. At low q, the x values become significant, thus rendering Eq. 2.67 not valid. In [10], this is done in a more rigorous manner, and it is shown that the expected power-law behaviour of such systems can be summarized by table 2.2.

2.4.5 X-ray sources

X-rays are produced in two main types of processes; acceleration of charged particles and when an electron changes from an atomic or ionic energy level to a lower one. Synchrotron radiation and bremsstrahlung are examples of the first type. These normally gives continuous spectra, but it is possible to obtain quasi-monochromatic lines from insertion devices, like undulators in synchrotron sources. The second type of process occurs when electrons bombard a low atomic number target or when a plasma is formed from a low atomic number material [30].

Copper x-ray sources

Before synchrotron radiation became widely used, bombarding solid targets with electrons was the most important method of generating x-rays. In order to avoid loss of electrons, this happened in vacuum. Modern sources for generation of x-rays using this principle developed from those used in the earlier experiments, as in the experiments of Röntgen. The emisson of x-rays from an electron beam incident on a positively charged anode happens by two processes. Bremsstrahlung is the process in which the incident electrons radiates a continuous spectrum of x-rays through the deceleration caused by coulombic interactions, while the other process is caused by the removal of an inner-level atomic electron followed by relaxation of the atom with emission of an x-ray. This x-ray has a well-defined energy, resulting in a line-spectrum characterised by the target material. The energy of the x-rays is limited by the energy of the incident electrons. The maximum energy results from an electron losing all its energy in one collision. However, the electron is likely to lose its energy over the course of several collisions, generating a distribution of x-ray wavelengths.

The labelling of x-ray lines is largely historical. The spectral series K, L, M etc. arise when an electron fills a vacant level with principal quantum number $n = 1, 2, 3...$ [30]. The strongest line is termed the α line, the next strongest the β line, and so on. Further, these lines are split according to their orbital and total angular momentum quantum numbers l and j, producing lines like α_1, α_2, β_1, β_2, etc.

The efficiency of production of continuum and characteristic x-rays is low [30]. To generate a high x-ray flux, the current of electrons need to be high. This could cause problems coupled with the high voltage, since most of the electrons in fact do not produce x-rays, but is dissipated as heat. Too much heat will deform the target, rendering it useless. Ways of avoiding this problem is to [30]

1. Use a target material with high conductivity and thermal capacity. The characteristics of copper is good concerning these problems.

2. Use a large, thin area target with low thermal capacity, so that

the temperature loss is kept low by the high rate of heat loss.

3. Use of extensions to the target. These will be outside the copper, and may also be cooled, in order to lead heat away efficiently.
4. Use direct cooling of the target by a flowing liquid, like water.
5. Use a moving target to spread the heat load over a larger area. A rotating anode is an example of this.

A combination of the above mentioned methods is of course possible.

Synchrotron radiation sources

It is well-known that a moving electrically charged particle experiences a force when subjected to a magnetic field perpendicular to its path. This force causes the particle to move in a circular path. The particle is thus accelerated, and so emits electromagnetic radiation. If the particle is accelerated to relativistic velocities, a Lorentz boost in the direction of instantaneous velocity shows that the radiation is very strongly peaked in the forward direction, with an angular divergence $\Delta\theta \approx \gamma^{-1}$, where $\gamma = \frac{E}{m_0 c^2}$. E is the total energy, and m_0 is the rest mass. The total power radiated in one revolution is proportional to γ^4 [30], which means that synchrotron radiation is most important for high energy and small mass particles, like electrons and positrons.

The first synchrotron sources used dipole bending magnets with fields of about 1.2 - 1.5 T to constrain the stored electron beam to roughly circular orbits. The spectrum from such a source is a continuum over a large wavelength range. The continuum is produced by the merging of a very large number of harmonics of the relativistic orbital frequency of the electrons.

Synchrotron radiation is elliptically polarised, except in the orbital plane, where it is linearly polarised [30]. This is an important property in many applications. A problem with synchrotrons is that they usually are remote from the laboratories of their users. Experimental time has to be booked in advance, and this can cause problems in the planning of the experiments, especially so for the biologial ones.

Chapter 3

Experiment

This chapter will present the equipment and procedures used for both making and investigating the samples. Other than that, the in-house x-ray system and the x-ray system at the ESRF will be documented, as well as the in-house imaging equipment. The copper capillary holder and other equipment used in the heating process of the different samples will be presented, as well as the software used in the process of writing this thesis.

3.1 The samples and how they were investigated

The samples investigated in this thesis were made by mixing NaFh with water. Usually, the salt NaCl was also added to this mix. The notable exception was for sample C4, where no salt was added. However, ions dissolved from the clay particles themselves are responsible for the *pH* being at approximately 10 [31]. The most important parameters of the investaged samples are given in table 3.1.

The temperature range that the samples were exposed to is given in table 3.2. Sample C1 has been investigated a bit more thorough. Two scans were made for 57 degrees, one some time after the other, in order to trace possible dynamics. Also, the sample was again scanned approximately one day after heating it to the maximum

Table 3.1: Important parameters of the samples investigated.

Sample parameter	C1	C3	C4	C5
Salt contents (mM NaCl)	10	1	0.1	10
NaFh contents ($\frac{w}{w\%}$)	3	3	3	3
Time from preparation (days)	34	11	11	11
Capillary diameter (mm)	2	1	1	1

temperature of 75 degrees, to check if the sample had changed after cooling to room temperature. All samples were scanned from close to or at the bottom of the capillary and upwards. Also, the scans are always as close to the long axis of the capillary as possible. In the plots of the results section, frame 1 will refer to the lowest position in the sample that was scanned. From this position, a motor vertically moved the sample down in steps of 1 or 2 millimeters, thus making the beam scatter from a position higher in the capillary. Because there is some uncertainty as to where each scan started, i.e. at what height above the bottom the first frame was positioned, I have chosen to refer to the scans as frame 1, frame 2, etc. Using table 3.3, it is possible to calculate at what height above the capillary each scan of each sample is. It should be noted that the author was not present during the experiments. However, a detailed journal and access to the participants of the experiment during the writing of the thesis secured that the necessary information regarding the experiment was available. However, even as these resources were available, some problems regarding the motor that moved the samples in the x-ray chamber at ESRF, could not be fully accounted for. The problems meant to the motor, sometimes, apparently moved a bit later than it was meant to. E.g. for the last series of experiments for sample C1, at 24 degrees following the heating and subsequent cooling the previous day, it could look like the motor started moving too late, meaning that frame 2 of this sample corresponds to frame 1 of the other series of experiments on this sample. In the same way, frame 2 could correspond to frame 3, etc. A similar problem could also be responsible for the somewhat odd behaviour shown by the 57 degrees series of sample C4. However, even if this was what probably happened, what really happened can not be said, and I will therefore try not to make any strong statements based on these series. In the data analysis, I have treated these series as if the motor problems was not there.

3.1.1 The powder

Synthetic Li-Fluorohectorite clay was purchased in powder form from Corning Inc., New York, and later ion-exchanged to produce Na-Fluorohectorite. The ion-exchange process consisted of adding 70 g of the purchased Li-intercalated fluorohectorite to 1000 ml distilled and de-ionized water, where it was dissolved and stirred by shaking for 2 days using an incubator at 300 rpm. Sodium ions were added as 60 g NaCl, which corresponds to about 10 times the known layer charge per unit cell. The suspension was further shaken

Table 3.2: The temperatures (in °C) investigated for the different samples.

C1	C3	C4	C5
24.0	24.0	24.0	24.0
38.3	38.4	38.4	38.4
47.4	47.7	47.7	47.7
56.8	57.1	57.0	57.1
56.8	-	57.1	-
66.1	-	-	-
75.3	75.7	75.8	75.6
-	87.8	87.7	87.7
24.0, 24 hours later	-	-	-

Table 3.3: Parameters of the scans from the ESRF SAXS experiments.

Info	C1	C3	C4	C5
Number of frames	21	16	16	15
Counting time	60 s	60 s	60 s	60 s
Vertical step size	1 mm	2 mm	2 mm	2 mm
Scan area	Bottom up	Bottom up	Bottom up	Bottom up

at 300 rpm for 2 weeks. Cl-ions were removed by dialysis, where the Cl-content was checked regularly using a standard silver nitrate procedure. NaFh powder was obtained by drying the resultant solution at 105 °C for about 3 days. A mortar and pestle was used before the NaFh powder was further pulverized using a milling machine (IKA A11 basic) [36].

To make the colloidal clay-saltwater solutions, this NaFh powder was mixed with solutions of varying content of NaCl as well as distilled water. Around half the salt solution was filled into a glass container, before the clay powder was weighed in. Finally, the rest of salt solutions was weighed in in order to obtain the desired amount of clay in the final product. After this, the clay-saltwater solution was shaken mechanically for some time, and eventually filled into their final destination, be it a 1 mm or 2 mm diameter glass capillary Hilgenberg Mark tube. These have a wall thickness of approximately 10 μm, and are made of borosilicate glass.

3.1.2 The sample holder

In order to heat the samples containing the various clay-saltwater solutions, a capillary holder of copper was utilized. The copper of this holder surrounded the vertically oriented capillary from below and above, and also on the sides except for a small opening for the x-ray beam. The copper holder was in thermal contact with another bit of copper through thermal paste. Water, coming from a water bath connected to a pump and a temperature controlling unit, ran through this second copper part, via plastic pipes. In this way, the first copper part obtained almost the same temperature as the water. The difference in temperature between the water and the first copper part was measured to be increasing with increasing temperature. This could be due to heat loss to the environment, but also the fact that different thermometers were used to measure the temperatures of the copper and the water could have had an effect. It was also found that the temperature measured decreased further for the contents of the capillary inside the copper capillary holder. To estimate the temperature of the clay-saltwater solutions, thermocouples were connected to both the capillary holder and to a water-containing 2 mm capillary, assuming that the water behaves more or less as a NaFh-clay-saltwater solution. In this way, it was possible to keep track of the approximate temperature of the samples investigated by x-rays.

Still, the temperatures given in this thesis are by no means very accurate, as the experimental methods used to measure them involved large uncertainties. They can only be used as an indicator. Yet another uncertainty comes from a teflon part of the sample holder, which purpose was to minimize the heat loss from the sample holder to the surroundings. Unfortunately, this design may have lead to the sample holder moving slightly when heating, probably due to the thermal expansion of this teflon part.

3.2 The optical birefringence setup

The NaFh dispersions were prepared with varying clay and salt concentrations and allowed to settle under the influence of gravity for weeks in 1 and 2 mm glass capillaries. The birefringence pictures taken were recorded with the samples placed between crossed polarizers and illuminated with a screen sending out diffuse, white light. The images was captured with a Canon EOS 350 D camera. A polarizing microscope was also used trying to reveal what effects heating of the samples lead to. The schematical setup was similar for both the camera connected to a microscope and the one not connected to a microscope.

However, the usefulness of the pictures was limited as it was difficult to monitor how the sample changed as the temperature was increased. In order to do this, one would have had to take the capillaries out of the sample holder and place it in the optical bire-

Table 3.4: Some relevant parameters of the x-ray experiments at NTNU.

Parameter	Value
Wavelength	1.5418 Å
Detector size	1024 × 1024 pixels
Pixel size	100 μm × 100 μm
Sample-to-detector distance	$\approx$ 1 m
beam size	400 μm × 400 μm

fringence set-up before taking pictures. Doing this, the temperature of the capillary would drop, and this time-consuming fact together with the difficulties of placing the capillary in the exact same spot in the capillary holder after taking it out, meant that this part of the experiment did not produce much useful information. However, this does not mean that no useful information can be gained from the use of crossed polarizers.

3.3 X-ray facilities

The x-ray scattering studies of the 1 mm and 2 mm glass capillaries, filled with a NaFh clay-saltwater solution, were conducted at two places. The in-house Bruker system, at NTNU, and at the Dutch-Belgian beamline (DUBBLE) at the European Synchrotron Radiation Facility (ESRF) in Grenoble, France. In the following, the characteristics of the two x-ray sources will be given.

3.3.1 In-house Bruker system

The Bruker NanoStar Saxs system delivers $\mathrm{Cu}_{K\alpha}$ radiation at a wavelength of 1.5418 Å. In the scattering experiments described in this thesis the sample-to-detector distance was approximately 1 meter. This means that the scattering angle was relatively small, making this a small angle x-ray scattering (SAXS) study. The relevant parameters are listed in table 3.4. More on this system can be found in e.g. [3]. The detector used to record the scattered intensity was a 2D HiStar detector.

3.3.2 ESRF

The European Synchrotrone Radiation Facility in Grenoble, France, facilitates a great radiation source for x-ray experiments. In this experiment, the DUBBLE beamline was used. The relevant parameters for this experiment is given in table 3.5, and the interested reader can find more on DUBBLE in [6].

Table 3.5: Some relevant parameters for x-ray experiments at ESRF.

Parameter	Value
Wavelength	1.24 Å
Detector size	512 × 512 pixels
Pixel size	$260 \times 260\ \mu\text{m}^2$
Sample-to-detector distance	≈ 7.6 m
beam size (hori vs. vert)	$300\mu\text{m} \times 200\ \mu\text{m}$

3.4 Data analysis

In this thesis, I have used Fit2D, Origin and MATLAB to analyze the x-ray diffractograms from the experiments. Fit2D has been used to import the raw diffractograms of the data from the experiment in Grenoble. These data has been reduced and normalized by subtracting the background scattering from a 2 mm capillary containing water and taking into account the variation of the intensity of the beam according to

$$I_s^{cor} = \frac{I_s}{M_{1s}} - \frac{T_s}{T_{c,w}} \frac{I_{c,w}}{M_{1c,w}}, \tag{3.1}$$

where I is intensity. I_s^{cor} denotes the corrected intensity of the sample. M_1 and M_2 are measures of the intensity of the beam before and after hitting the sample, respectively. T denotes the transmission of the samples, and is calculated as $\frac{M_2}{M_1}$. The subscripts s and c, w denotes sample, capillary and water.

The sensitivity of the pixels of the detector might respond to being hit by photons in a different manner. Therefore, the reduced data was divided by a diffractogram that was made from exposing the detector to an isotropic radiation source, i.e. a radioactive source that in theory should send out equal amounts of radiation in all directions. The diffractogram provided by DUBBLE did not seem to produce very good normalized diffractograms. They looked better than the unnormalized ones, but there were still some artifacts visible, e.g. in the form of vertical stripes of the normalized diffractograms that in my opinion are not very likely to be caused by something actual going in the sample. However, of the diffractograms available, I chose the one that seemed best. The reduced and normalized files was then integrated according to what I wanted to find. MATLAB has been used to run a script that finds a quasi-ellipse where the intensity of a diffractogram was equal to a selected intensity. For isotropic diffractograms, this procedure leads to ellipses that are close to circular, while the semi-major axis can be much larger than semi-minor axis for anisotropic diffractograms. The script has been

created by D. Fonseca, and was used by Fonseca *et al* in [9, 10]. Origin has mainly been used to plot the results.
The data from NTNU was also treated using Fit2D, but not in the same manner, e.g. scattering from the capillary and water was not subtracted before integrating. Nevertheless, the scattered intensity from a capillary filled with water revealed much lower intensity than that of a capillary with water and clay. Therefore, I believe that the plots made from these data sufficed very well as a first approximation of what heating of such samples lead to. Studying data from the DUBBLE experiment without subtracting the scattering from the capillary with water revealed that the main characteristics of the plot remained the same, even though there of course might have been differences that were hard to spot by eye. The results of the NTNU experiment will not be given in this thesis, but they were indeed important in the process of designing the DUBBLE experiment.

Integration of subtracted and normalized diffractograms

In order to calibrate the distance and other important parameters, a standard collagen rat tail sample was used. After subtraction of the scattering from a capillary with water and no clay, and the following normalization process by dividing by the abovementioned isotropically exposed diffractogram, the resulting files was treated in basically three ways. First, in order to make plots of the scattered intensity vs. the azimuthal angle, I used Fit2D to divide the diffractograms into one radial bin and 400 azimuthal bins. The integration took place over all available q-range, i.e. $0 < q < 0.44$ nm^{-1}. The lower boundary could of course have been increased, as the beamstop is likely to have occupied most of the area in the low q-range. However, the subtraction and normalization process described above should lead to this method giving an acceptable accuracy.
Concerning the plots of scattered intensity vs. q, these were made in a similar fashion. This time the integration involved one azimuthal bin and 300 radial bins. The q-range started this time at 0.08 nm^{-1}. The anisotropic samples was integrated radially in the 30 degrees that had the highest intensity. The borderline between anisotropic and isotropic was not always very clear, but comparing both isotropic and anisotropic radial integration, and trying to find for what degree of anisotropicity the two methods yielded different results, I believe that I have integrated most of the diffractograms in a sound fashion. However, it should be noted that there could be some anisotropically integrated diffractograms that should have

been integrated isotropically, even if this of course should result in the same plot if the sample really was isotropic, and vice versa.
The same subtracted and normalized diffractograms used in the integration described above was used for the making of spread sheets later utilized in the fitting of isointensity ellipses. The script generates a text file containing the size of both semi-major axis a and semi-minor axis b, thus making the eccentricity $e = \frac{\sqrt{a^2-b^2}}{a}$ easy to find. More on this script and how it works can be read in [9].

Chapter 4

Results and Discussion

The effects of heating a NaFh clay-saltwater solution inside 1 mm and 2 mm glass capillaries have been investigated using small angle x-ray scattering (SAXS). The experiment took place at ESRF in May 2010. In the following, the four investigated samples will be treated one by one. The plots will be accompanied by comments, before a discussion of the possible implications of the results will take place in the discussion section.

4.1 Results

C1

A montage of all the diffractograms from sample C1, except the last series for T = 57 °C, is shown in Figure 4.1. It reveals that peaks are appearing when the temperature is increased from 38 to 47 degrees. This is most visible in the frames that are recorded around 5 - 10 mm above the bottom of the capillary, but this feature can be seen for frames at other heights as well. Also worth noting is that the frames that are recorded approximately 11 - 16 mm above the bottom seem to be somewhat anisotropic. That these frames indeed are anisotropic is confirmed in the plot of the scattered intensity as a function of the azimuthal angle for all the heights in Figure 4.2. The same frames in the far right of the montage, showing what the diffractograms looked like approximately 24 hours after heating the sample to 75 degrees and subsequently cooling it to 24 degrees, indicates that the anisotropicity is, to some extent, less prominent. This is confirmed in Figure 4.3. The plots of the scattered intensity vs. azimuthal angle for all the heights at 47, 66 and 75 degrees in Figures 4.4, 4.5 and 4.6 indicate that most of the changes in the azimuthal distribution of the scattered intensity have taken place

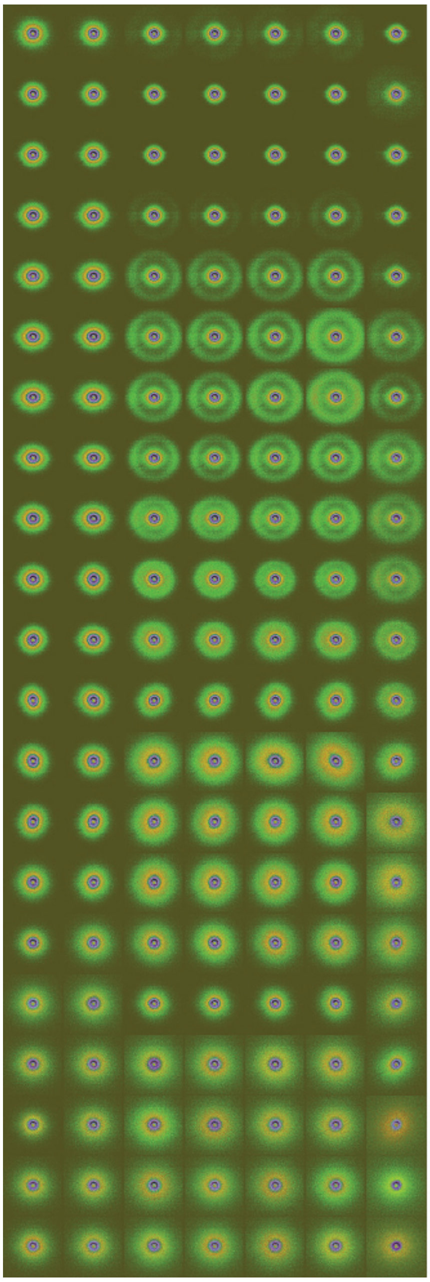

Figure 4.1: This is a montage of the diffractograms from sample C1. They are scaled and normalized in order to try and show the emerging peaks. The coloumns are representing one temperature each. From left to right: 24, 38, 47, 57, 66 and 75 degrees. To the right are the diffractograms of the sample at 24 degrees, 24 hours after heating it. Vertically, the topmost frames are frame 1, i.e. around the bottom at the capillary. Going down the coloumn corresponds to going up in the capillary. The vertical step size is 1 mm, thus making the frame at the bottom of the figure approximately 21 mm above the bottom of the capillary.

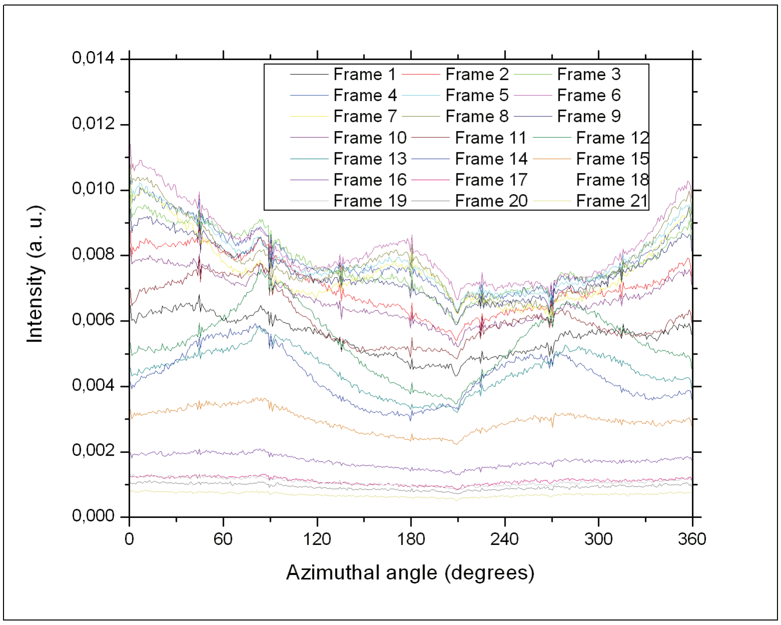

Figure 4.2: Azimuthal variations of the scattered intensity of sample C1 at 24 degrees.

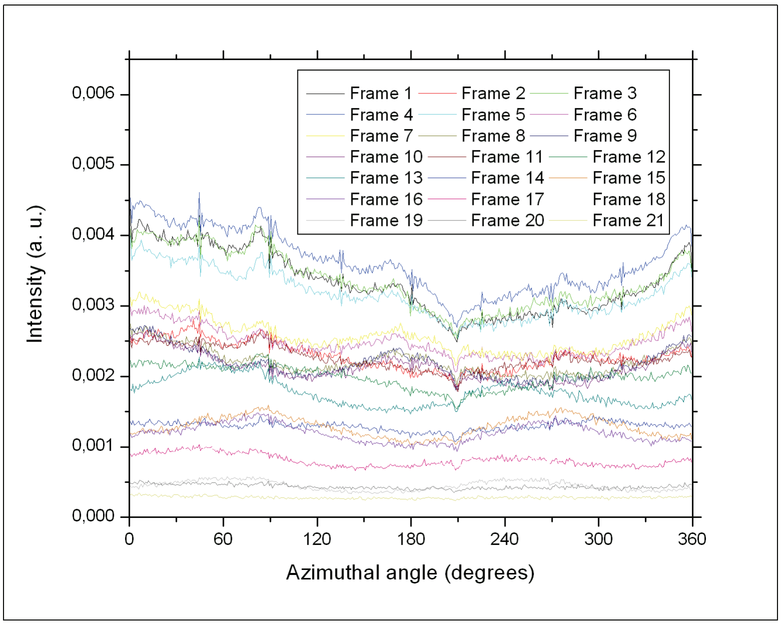

Figure 4.3: Azimuthal variations of the scattered intensity of sample C1 at 24 degrees, around one day after heating it to 75 degrees.

before the temperature reached 47 degrees.

In Figure 4.7, the scattered intensity vs. the scattering vector is shown for all the heights of the sample before heating, i.e. at 24 degrees. It can be seen that the slopes are steeper than q^{-2} for the lowest q-values, and that the slopes become somewhat less steep than q^{-2} as q increases. This seems to be the general trend, but it should be noted that frame 1, which is approximately 1 mm above the bottom of the capillary, behaves different than the others. The difference between this plot and Figure 4.8, which is found for the sample 24 hours after, after heating and subsequent cooling, is striking. The intensity of the lowest q-values are much smaller for the frames near the bottom of the capillary. When looking at higher q-values, they intensity actually increases for some of the heights, while for others, the slopes become less steep. In Figures 4.9, 4.10, 4.11 and 4.12, similar plots show the behaviour for the sample having temperatures of 38, 47, 57 and 75 degrees, respectively. It is hard to tell a lot from these plots, as there are many curves in them, but note how the intensity drops, seemingly for all heights, when the temperature increases. The peaklike characteristic of the curves seem to be much more prominent for the frames near the bottom of the capillary.

Figure 4.13 shows the scattered intensity vs. q for all the temperatures of frame 2, i.e. at approximately 2 mm above the bottom. Note how the intensity drops as the temperature is increases, and how this feature seems to be more pronounced for q-values below ≈ 0.3 nm^{-1}. As the scattering vector approaches the maximum value studied in this experiment, the intensity of the higher temperature curves appoach that of the 24 degrees curve. Figure 4.14 shows this behaviour in a log-log plot of the intensity multiplied by q^2 vs. q. The same plots for frame 4, shown in Figures 4.15 and 4.16, reveal the same behaviour. That the slopes at low q-values becomes less steep as higher positions in the capillary are investigated, is evident from Figures 4.17 to 4.24, which shows the same plots as described above for 6, 10, 14 and 18 mm above the bottom of the capillary. This seems to hold for both the frames recorded at 24 degrees and the frames recorded at higher temperatures.

All heights in the capillary at 38 and 47 degrees, in addition to both series at 57 degrees, have had their subtracted and normalized diffractograms fitted to iso-intensity ellipses, as described in the experimental section. The most striking feature is the change in eccentricity for frames 13 - 17 when heating the sample from 38 to 47 degrees. This is shown in Figure 4.25. The ellipses fitted to the diffractograms recorded at 57 degrees reveal that changes have

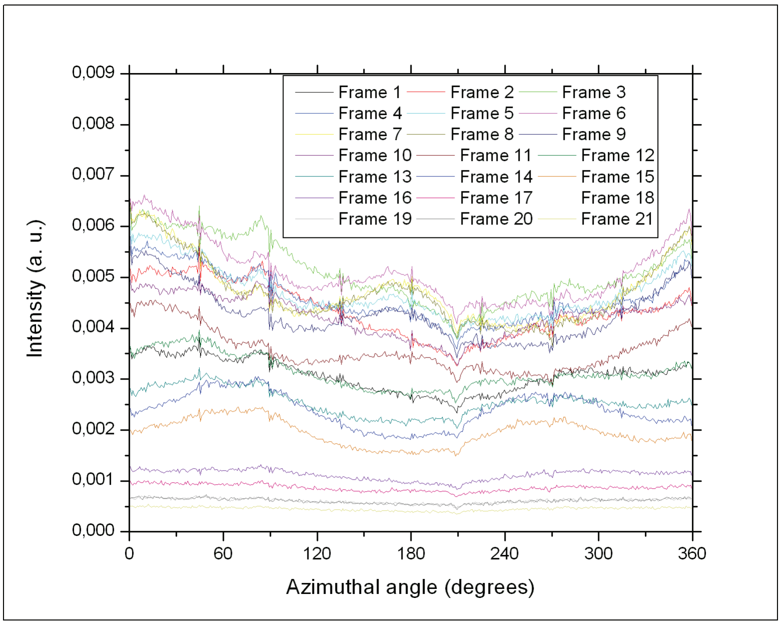

Figure 4.4: Azimuthal variations of the scattered intensity of sample C1 at 47 degrees.

occured, both when going from 47 to 57 degrees, and between the two series at 57 degrees. However, the changes are not as dramatic as they were when increasing the temperature from 38 to 47 degrees.

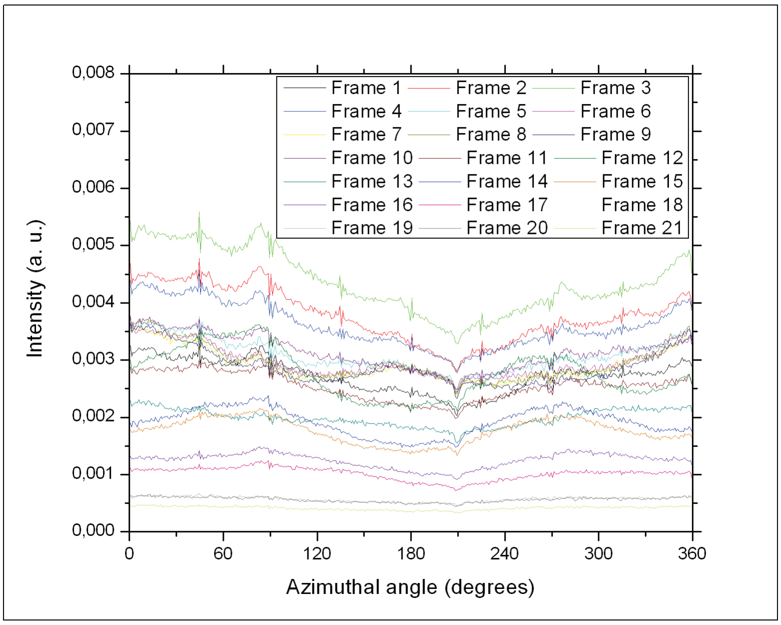

Figure 4.5: Azimuthal variations of the scattered intensity of sample C1 at 66 degrees.

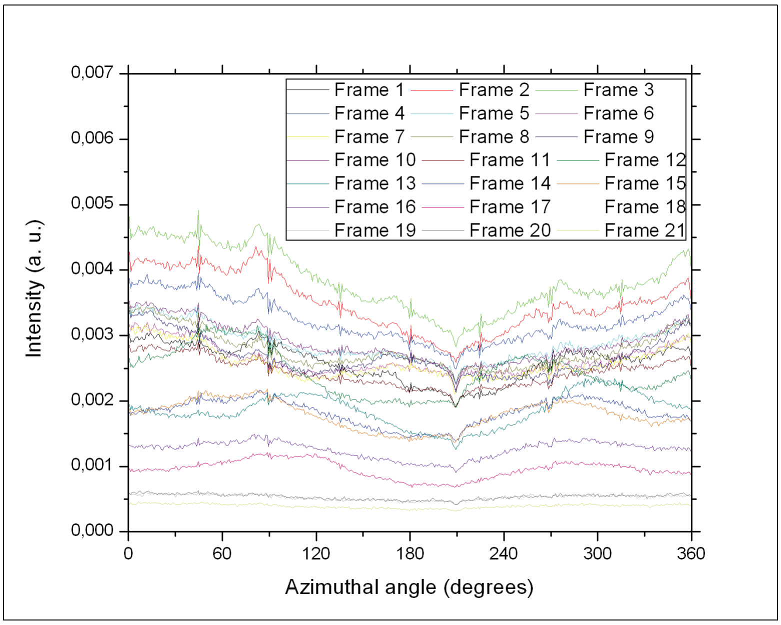

Figure 4.6: Azimuthal variations of the scattered intensity of sample C1 at 75 degrees.

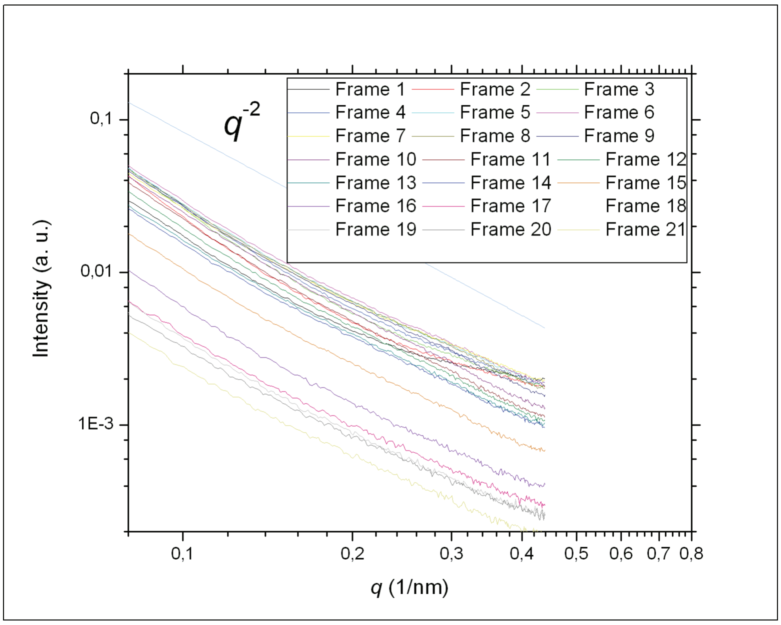

Figure 4.7: The scattered intensity vs. the scattering vector q of sample C1 for various heights. The sample held a temperature of 24 degrees.

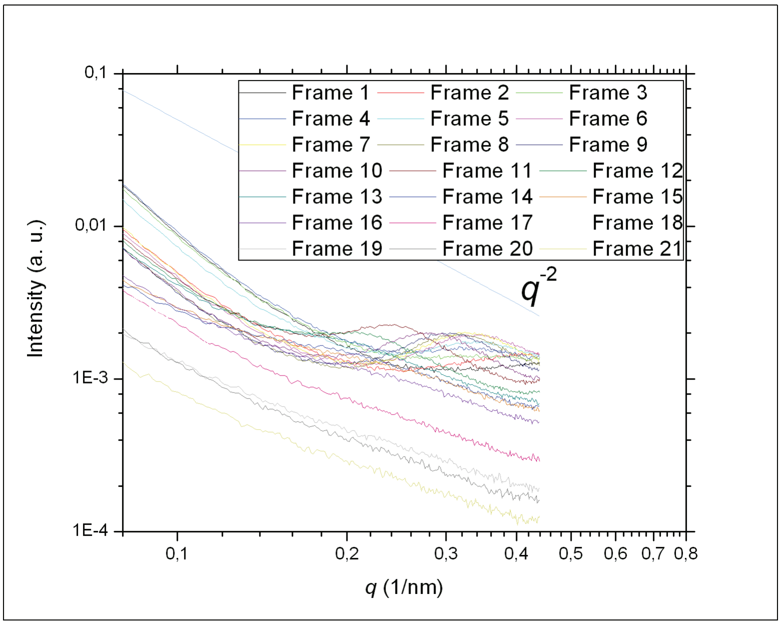

Figure 4.8: The scattered intensity vs. the scattering vector q of sample C1 for various heights. The sample held a temperature of 24 degrees, this time around one day after heating the sample to 75 degrees.

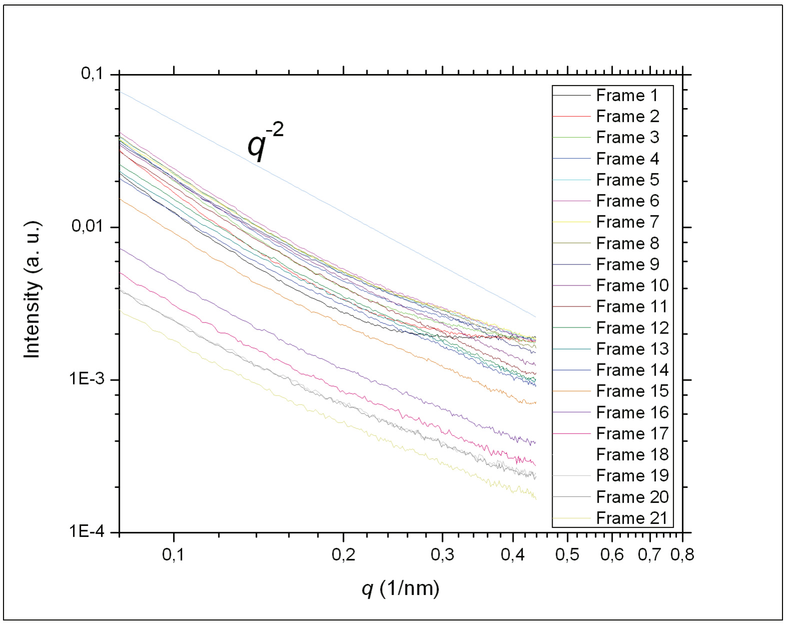

Figure 4.9: The scattered intensity vs. the scattering vector q of sample C1 for various heights. The sample held a temperature of 38 degrees.

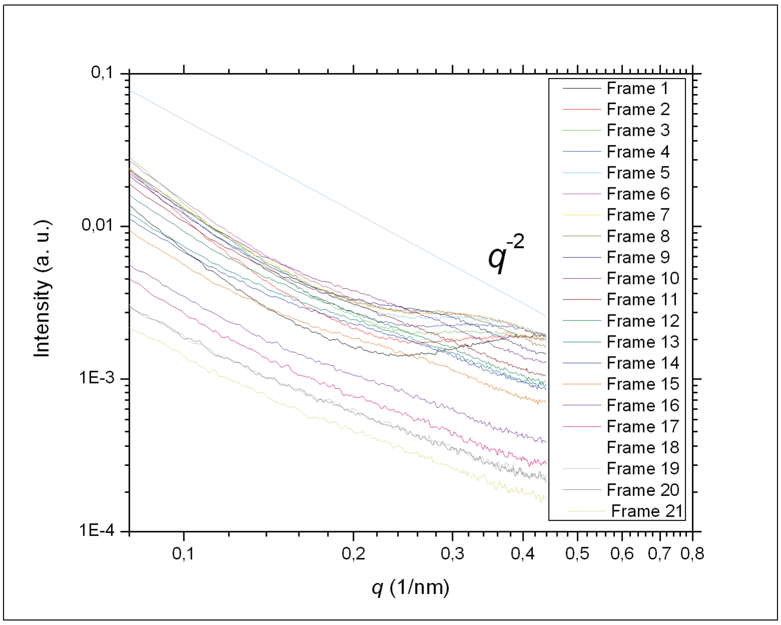

Figure 4.10: The scattered intensity vs. the scattering vector q of sample C1 for various heights. The sample held a temperature of 47 degrees. Emerging peaks can clearly be seen.

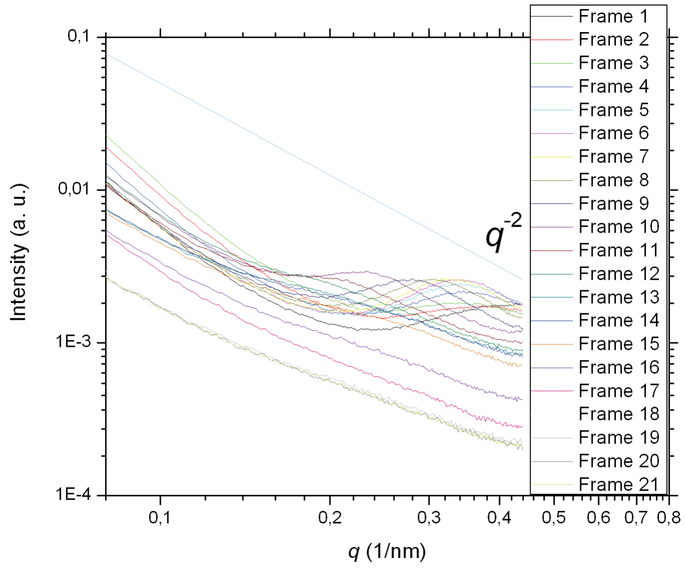

Figure 4.11: The scattered intensity vs. the scattering vector q of sample C1 for various heights. The sample held a temperature of 57 degrees.

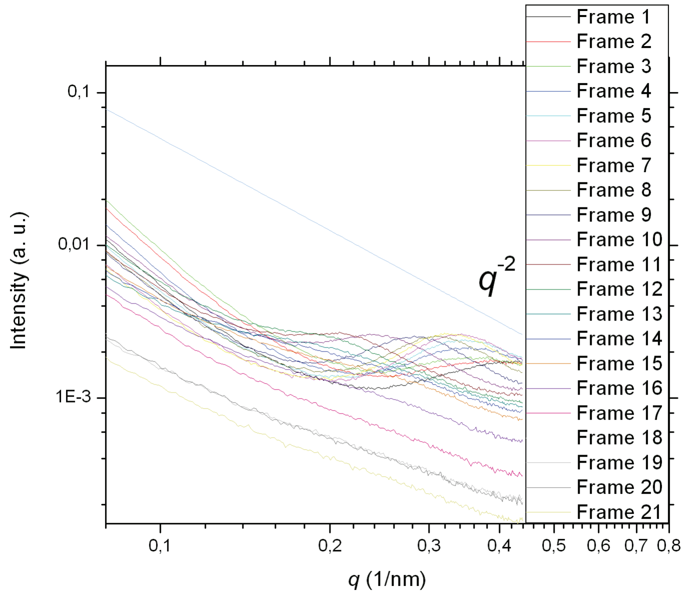

Figure 4.12: The scattered intensity vs. the scattering vector q of sample C1 for various heights. The sample held a temperature of 75 degrees.

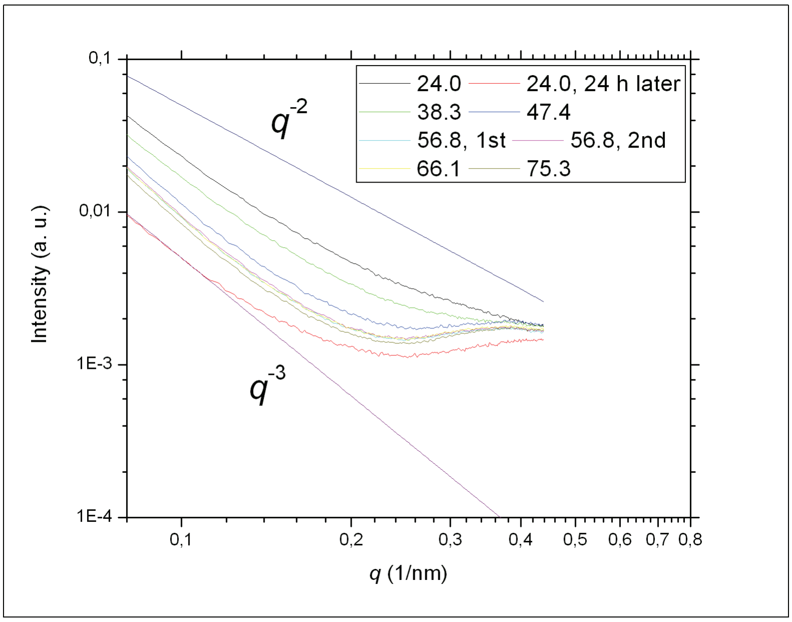

Figure 4.13: The scattered intensity vs. the scattering vector q of sample C1 for different temperatures. This is frame 2, approximately 2 mm above the bottom of the capillary.

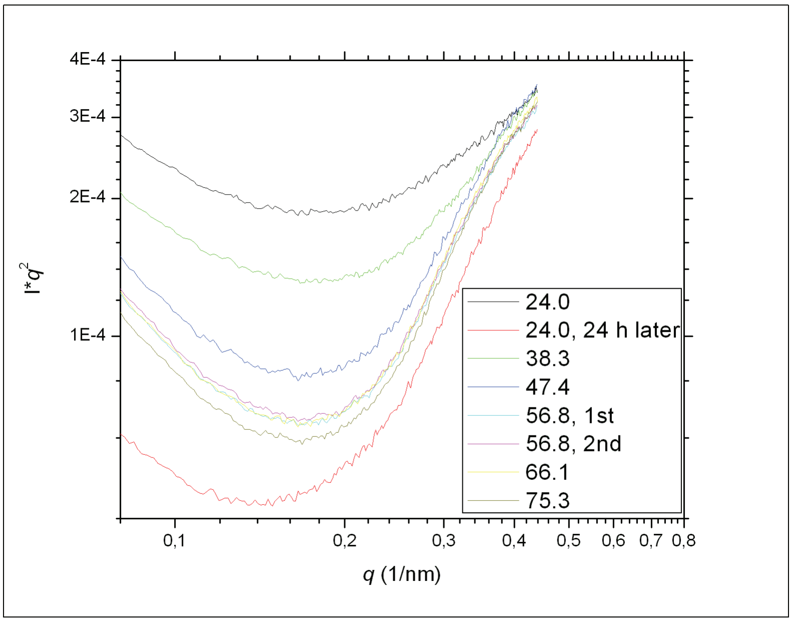

Figure 4.14: The scattered intensity multiplied by q^2 vs. q of sample C1 for different temperatures. This is frame 2, approximately 2 mm above the bottom of the capillary.

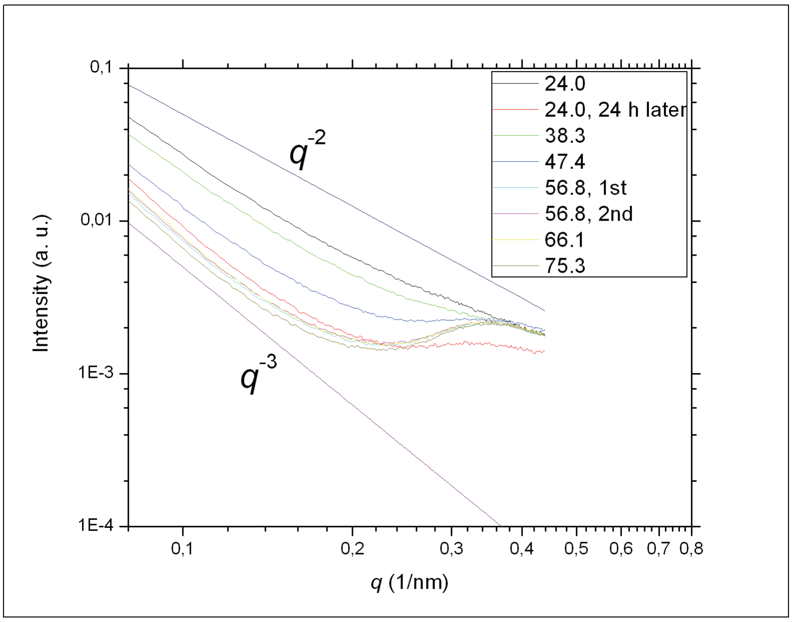

Figure 4.15: The scattered intensity vs. the scattering vector q of sample C1 for different temperatures. This is frame 4, approximately 4 mm above the bottom of the capillary.

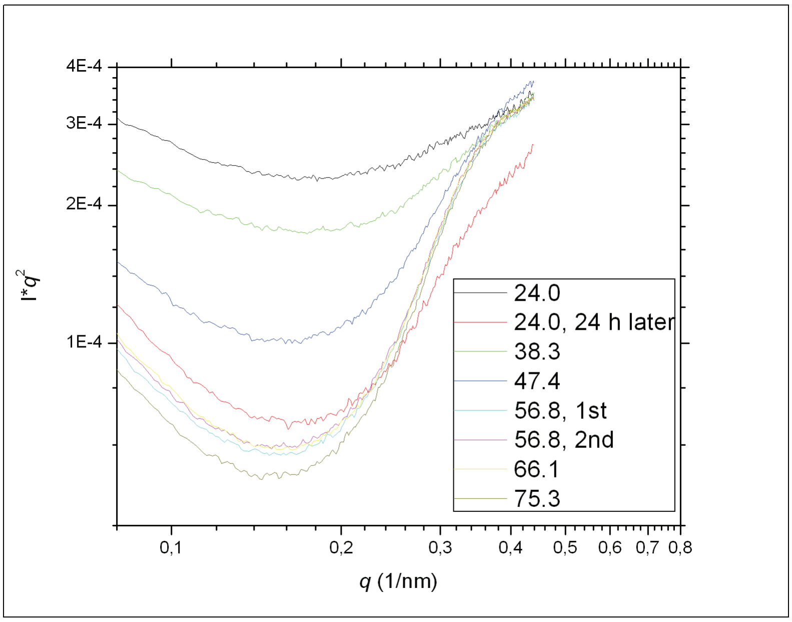

Figure 4.16: The scattered intensity multiplied by q^2 vs. q of sample C1 for different temperatures. This is frame 4, approximately 4 mm above the bottom of the capillary.

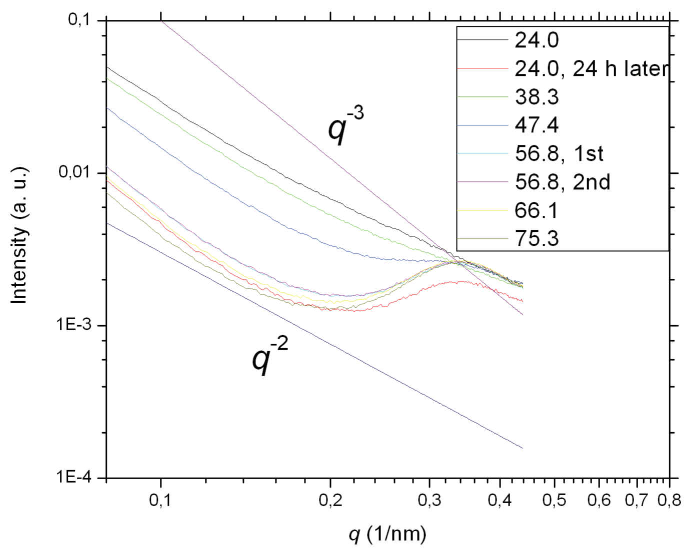

Figure 4.17: The scattered intensity vs. the scattering vector q of sample C1 for different temperatures. This is frame 6, approximately 6 mm above the bottom of the capillary.

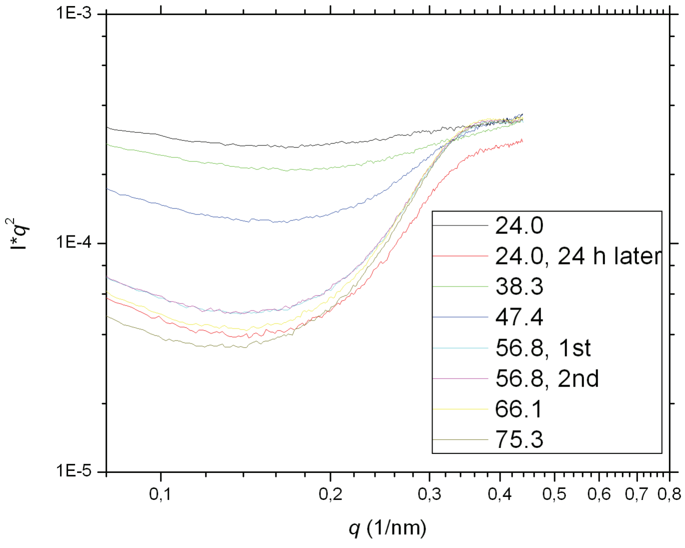

Figure 4.18: The scattered intensity multiplied by q^2 vs. q of sample C1 for different temperatures. This is frame 6, approximately 6 mm above the bottom of the capillary.

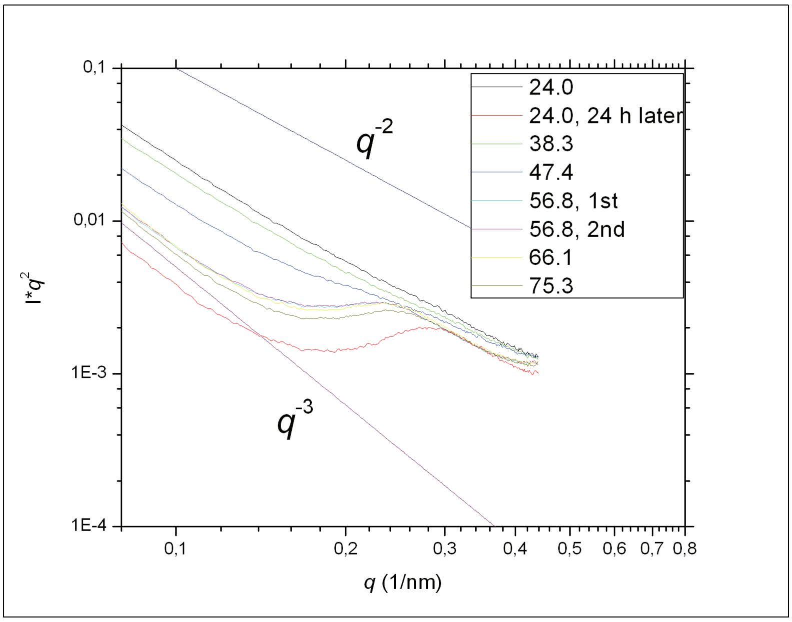

Figure 4.19: The scattered intensity vs. the scattering vector q of sample C1 for different temperatures. This is frame 10, approximately 10 mm above the bottom of the capillary.

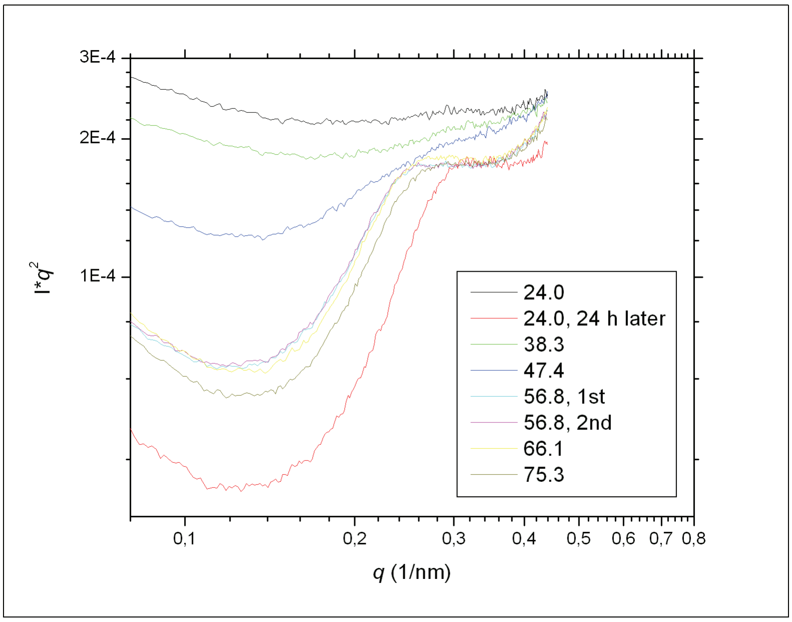

Figure 4.20: The scattered intensity multiplied by q^2 vs. q of sample C1 for different temperatures. This is frame 10, approximately 10 mm above the bottom of the capillary.

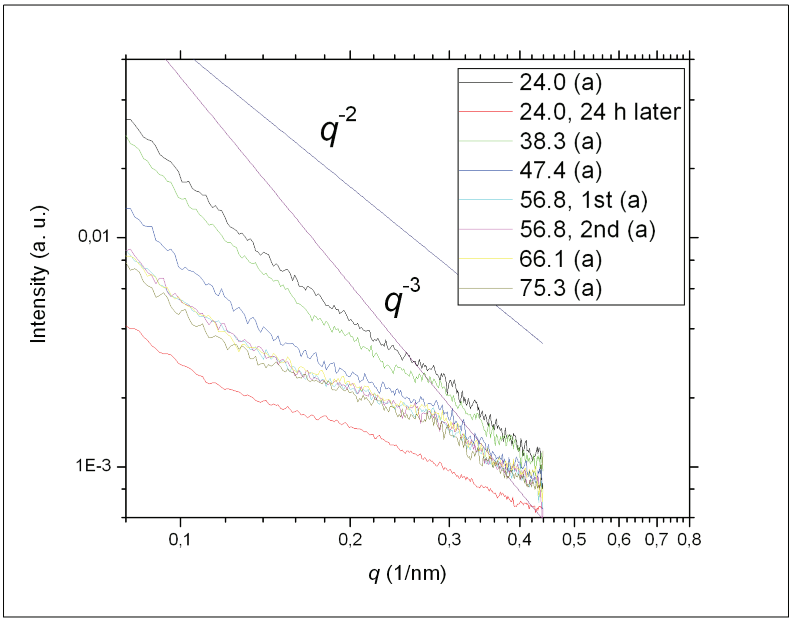

Figure 4.21: The scattered intensity vs. the scattering vector q of sample C1 for different temperatures. This is frame 14, approximately 14 mm above the bottom of the capillary. Anisotropically integrated frames are marked with (a).

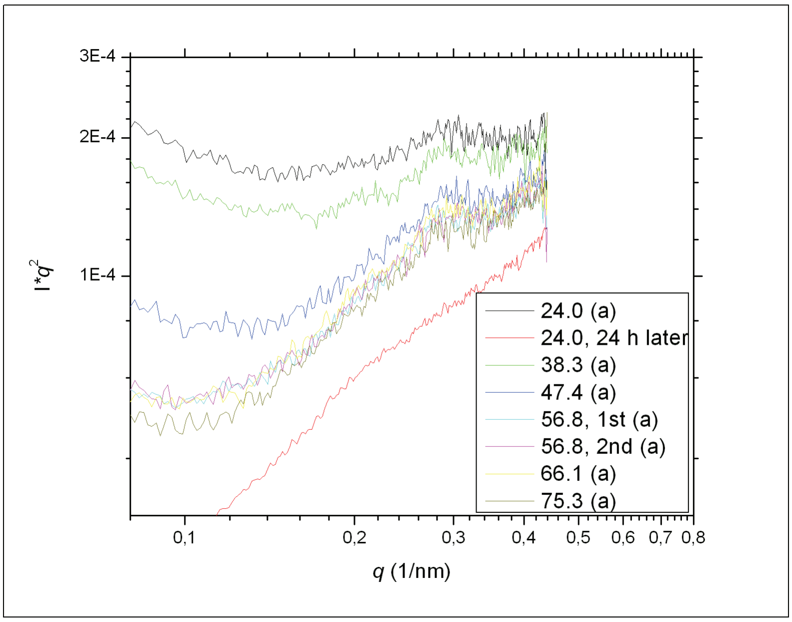

Figure 4.22: The scattered intensity multiplied by q^2 vs. q of sample C1 for different temperatures. This is frame 14, approximately 14 mm above the bottom of the capillary.

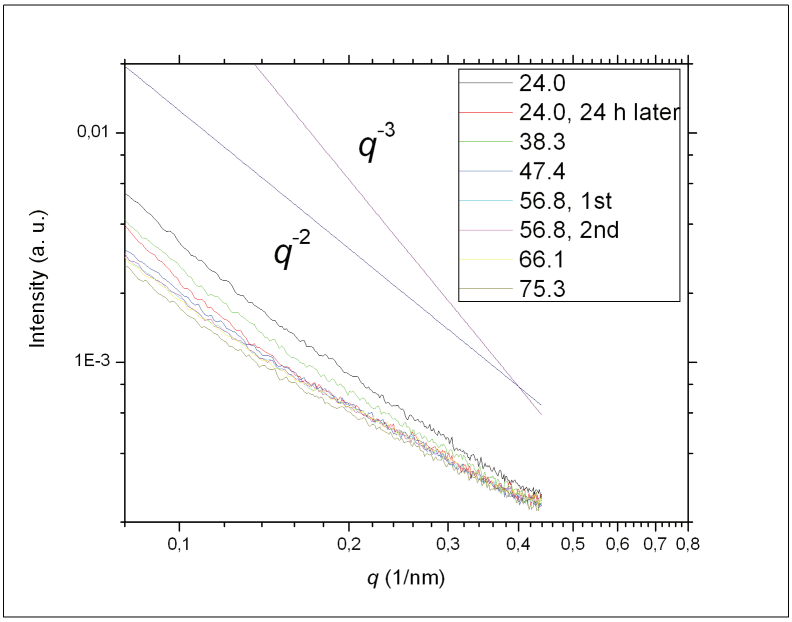

Figure 4.23: The scattered intensity vs. the scattering vector q of sample C1 for different temperatures. This is frame 18, approximately 18 mm above the bottom of the capillary.

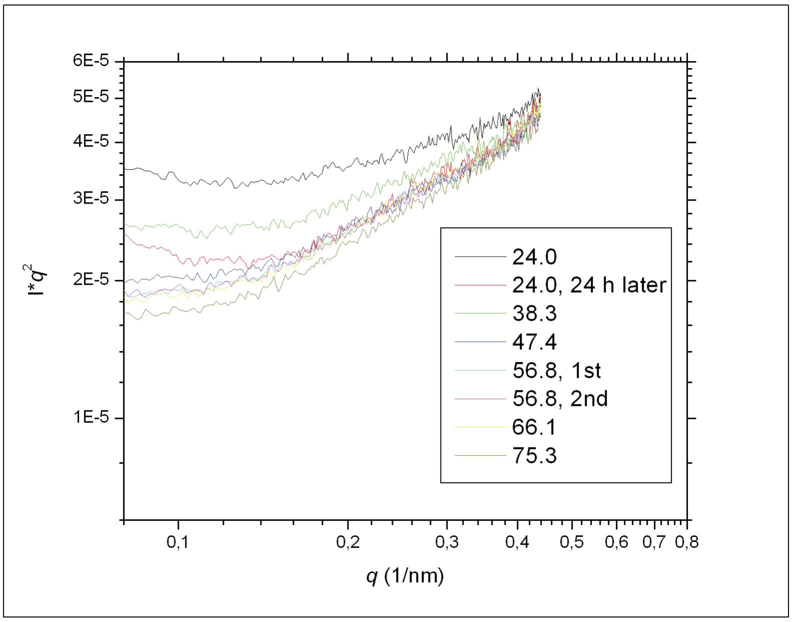

Figure 4.24: The scattered intensity multiplied by q^2 vs. q of sample C1 for different temperatures. This is frame 18, approximately 18 mm above the bottom of the capillary.

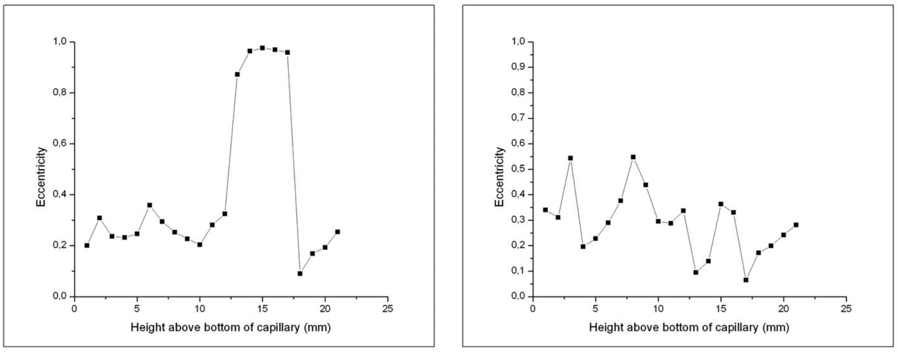

(a) 38 degrees.

(b) 47 degrees.

Figure 4.25: The eccentricity of the iso-intensity ellipses of sample C1 as a function of height above the bottom of the capillary.

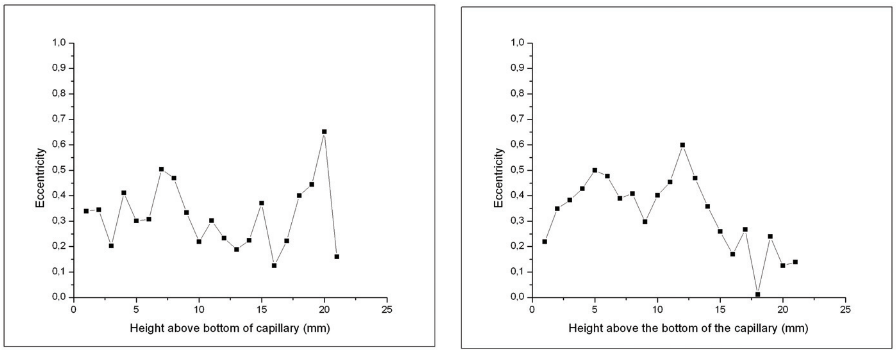

(a) 57 degrees.

(b) 57 degrees, some time later.

Figure 4.26: The eccentricity of the iso-intensity ellipses of sample C1 as a function of height above the bottom of the capillary.

C3

Figure 4.27 shows sample C3 between crossed polarizers before heating. A montage of all the diffractograms recorded of this sample is shown in Figure 4.28. The emerging peaks in this sample are not as readily seen as they were for sample C1, as least not from the diffractograms. What is easiest recognized is how the samples in the bottom of the montage, i.e. from frame 11 to 16 (approximately 21 - 31 mm above the bottom), produce very anisotropic diffractograms. The anisotropicity of these diffractograms are easily recognized in the plots showing the scattered intensity as a function of azimuthal angle, as seen in Figures 4.29, 4.30 and 4.31 for temperatures of 24, 76 and 88 degrees, respectively. Also, the montage reveals that the

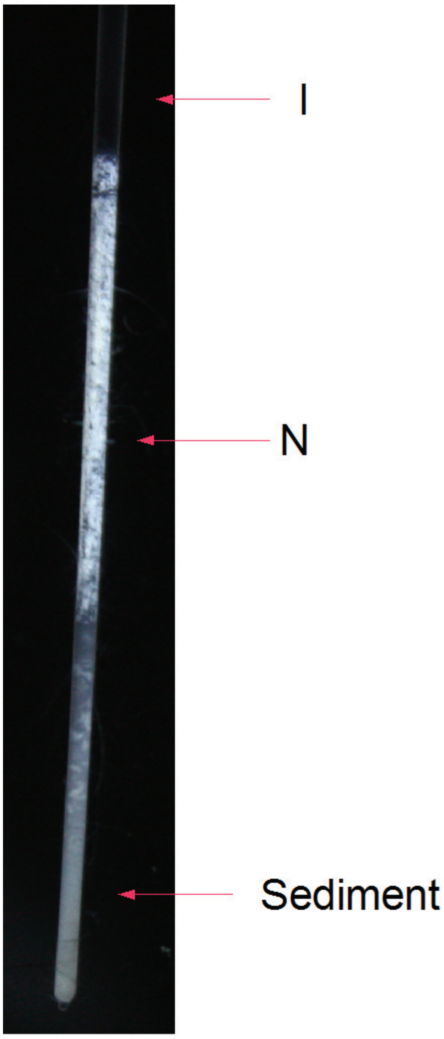

Figure 4.27: Picture of sample C3 between crossed polarizers. The isotropic (I) and nematic (N) phases are indicated, as well as the sediment.

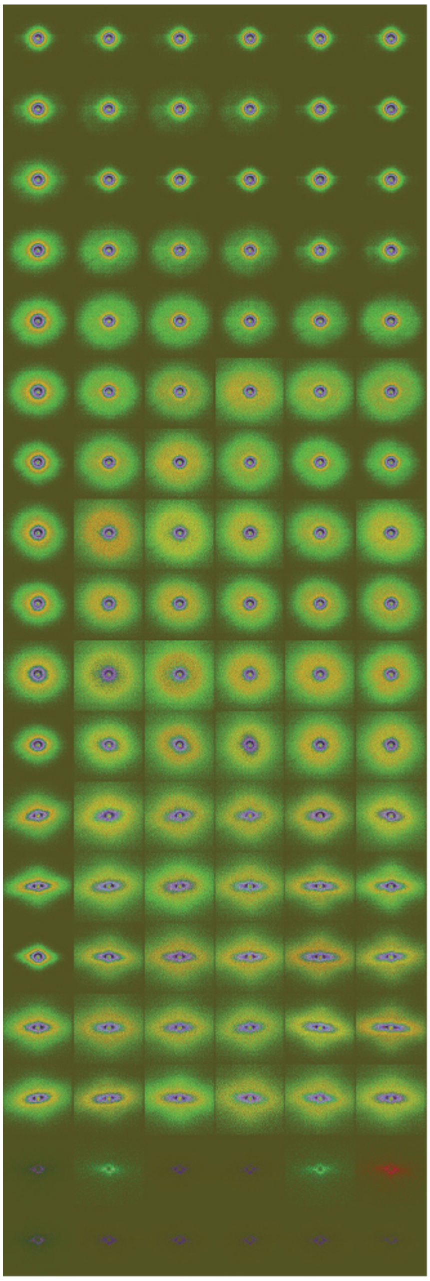

Figure 4.28: This is a montage of the diffractograms from sample C3. They are scaled and normalized in order to try and show the emerging peaks. The coloumns are representing one temperature each. From left to right: 24, 38, 48, 57, 76 and 88 degrees. Vertically, the topmost frames are frame 1, i.e. around the bottom at the capillary. Going down the coloumn corresponds to going up in the capillary. The vertical step size is 2 mm, thus making the frame at the bottom of the figure approximately 35 mm above the bottom of the capillary. The two rows at the bottom of this montage have been omitted in the analysis.

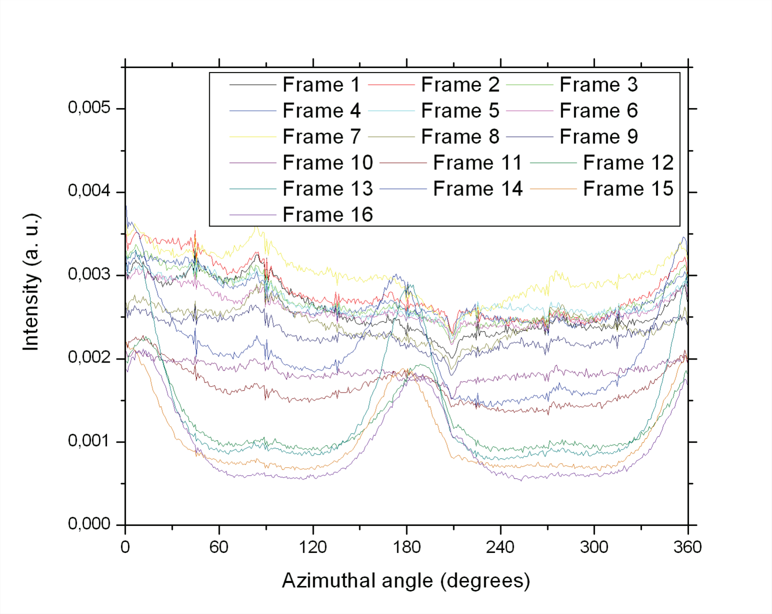

Figure 4.29: Azimuthal variations of the scattered intensity of sample C3 for different heights. The sample held a temperature of 24 degrees.

azimuthal angle of maximum intensity seems to be tilting for some frames for the highest temperatures.

The plots of the scattered intensity vs. the scattering vector for all the frames for temperatures of 24, 38 and 88 degrees are shown in Figures 4.32, 4.33 and 4.34, respectively. It is evident that the slopes of some of the curves become less steep for increasing q-values as the temperature is increased - in other words, they have a peaklike characteristic. To see this clearer, it is easier to consider one frame at the time as the temperature is increased. The intensity, both multiplied by one and q^2 as a function of q, is shown for frame 3 in Figures 4.35 and 4.36. Here, the most noteable feature is how the intensity of the 24 degrees curve does not drop like that of the higher temperature curves for $q \approx 0.1 - 0.2$ nm^{-1}. However, this drop is not as marked as it was for frame 4 (Figure 4.15) of sample C1, which was at a similar height. That these samples behave differently is no wonder considering that age, salt concentration and capillary diameter all are different. Figures 4.37 and 4.38 shows the same plots for frame 6. Here, the drop of intensity for ≈ 0.15 nm$^{-1} > q >\approx 0.30$ nm^{-1} for the higher temperatures compared to the 24 degrees curve is more pronounced. This also seem to be the case for frame 10, as evident from Figures 4.39 and 4.40, but this time the drop in intensity seems to be at somewhat lower q-values. For frame 14, seen

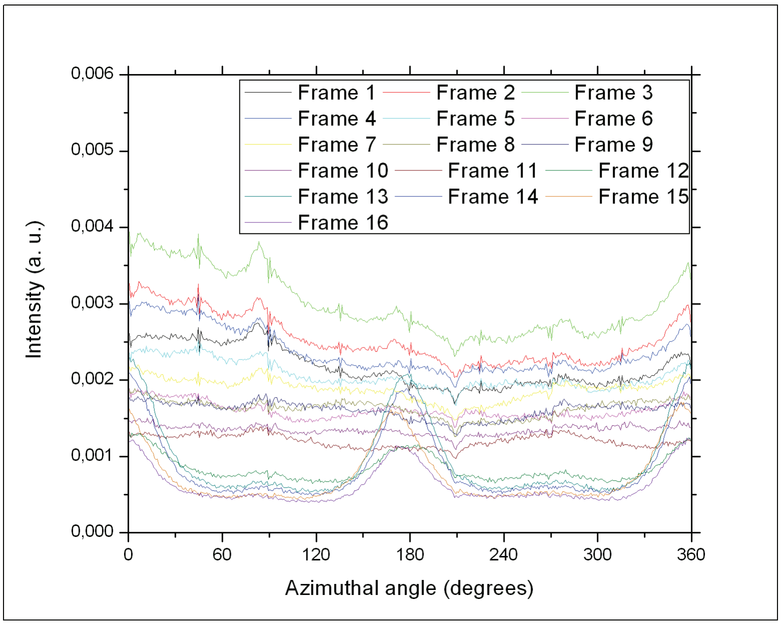

Figure 4.30: Azimuthal variations of the scattered intensity of sample C3 for different heights. The sample held a temperature of 76 degrees.

in Figures 4.41 and 4.42, the 24 degrees curve again acts in another way than the other temperatures, falling off very much like q^{-2}, while the others indeed fall off more slowly. The q^{-2} slope of the 24 degrees curve for frame 14 in Figure 4.42 could mean that the platelets are highly oriented, with the normal vector parallel to the scattering vector. This is consistent with the diffractogram in Figure 4.28, which indicates that the scattering particles are standing, i.e. have their normal vectors almost perpendicular to both the cylinder axis and the beam. As the temperature is increased, the anisotropicity seems to still be present, as evident from the diffractograms and the azimuthal plots. However, the slope become less steep for the heated curves.

For the scattered intensity of sample C3 vs. q for various temperatures, there seems to be gradual changes between the plots shown here.

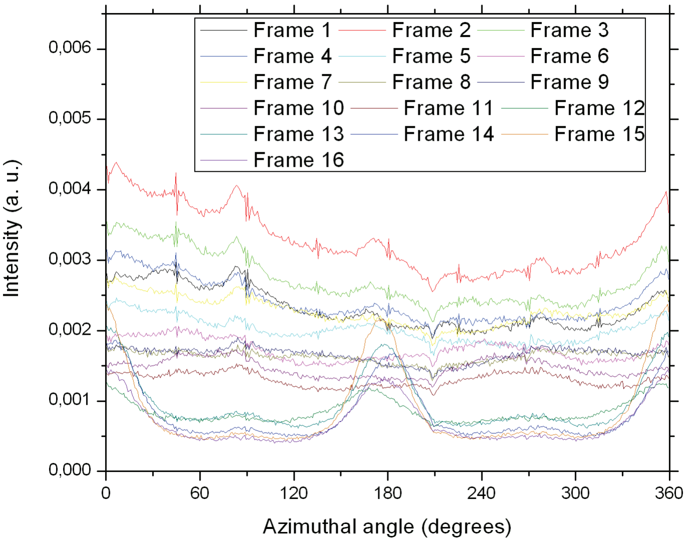

Figure 4.31: Azimuthal variations of the scattered intensity of sample C3 for different heights. The sample held a temperature of 88 degrees.

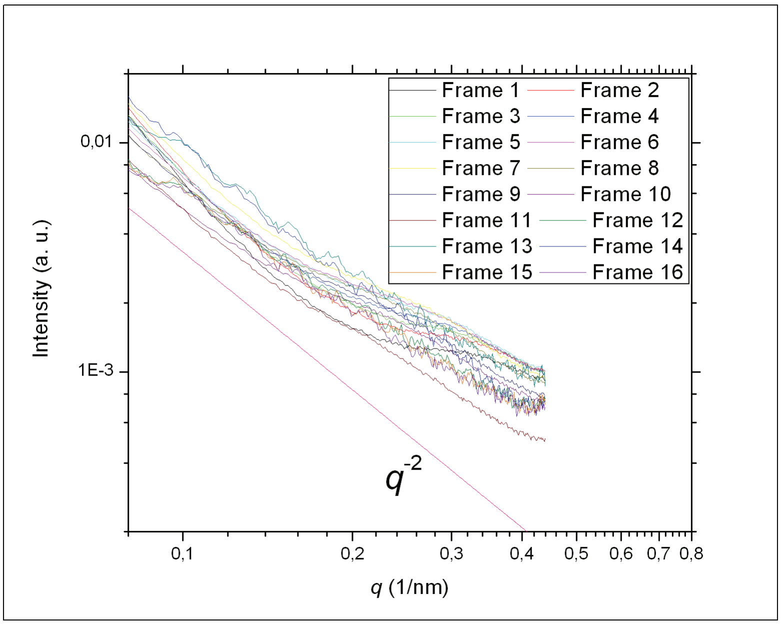

Figure 4.32: The scattered intensity of sample C3 vs the scattering vector q. The sample held a temperature of 24 degrees. Frames 12-16 have been anisotropically integrated. Frame 1 is approximately 1 mm over the bottom of the capillary. The other frames are recorded going stepwise towards the top of the capillary, 2 mm per step.

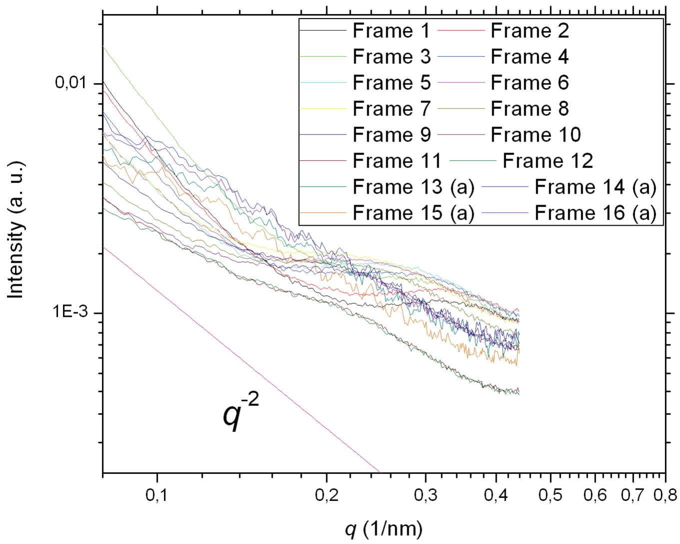

Figure 4.33: The scattered intensity of sample C3 vs the scattering vector q. The sample held a temperature of 38 degrees. The frames that are marked with (a) are anisotropically integrated. Frame 1 is approximately 1 mm over the bottom of the capillary. The other frames are recorded going stepwise towards the top of the capillary, 2 mm per step.

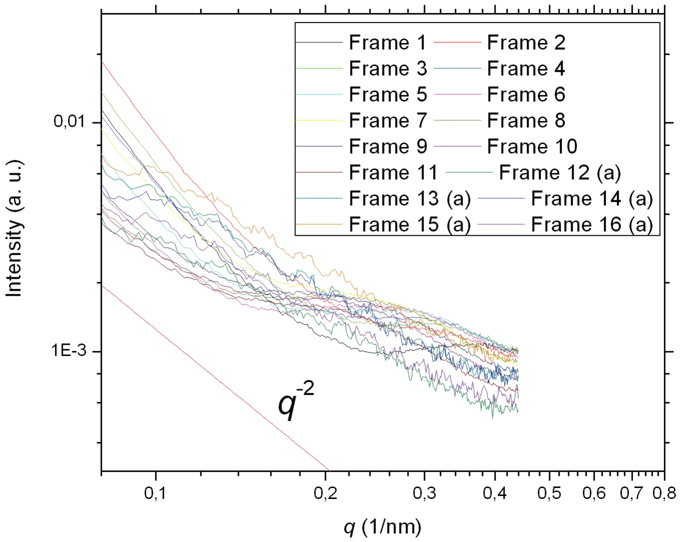

Figure 4.34: The scattered intensity of sample C3 vs. the scattering vector q for various heights. The sample held a temperature of 88 degrees. The frames that are marked with (a) are anisotropically integrated. Frame 1 is approximately 1 mm over the bottom of the capillary. The other frames are recorded going stepwise towards the top of the capillary, 2 mm per step.

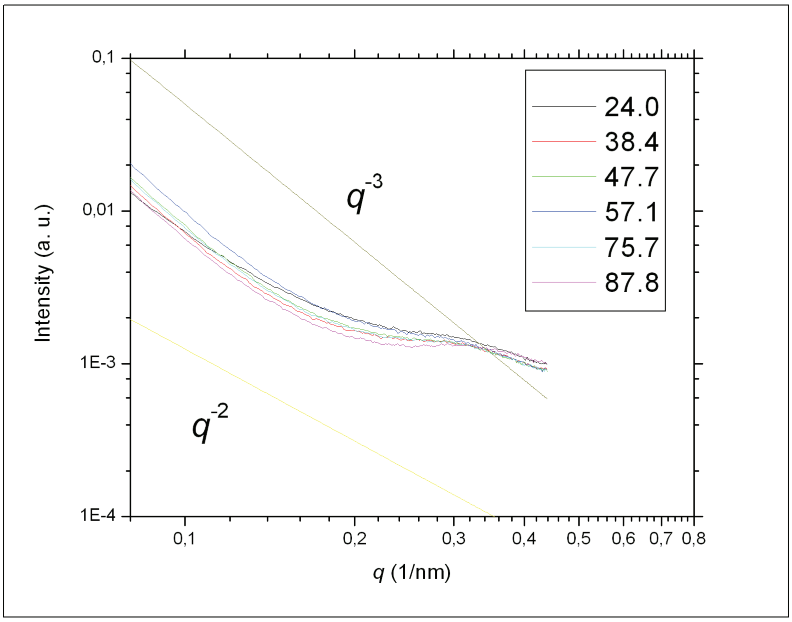

Figure 4.35: The scattered intensity vs. the scattering vector q of sample C3 for various temperatures. This is frame 3, approximately 5 mm above the bottom of the capillary.

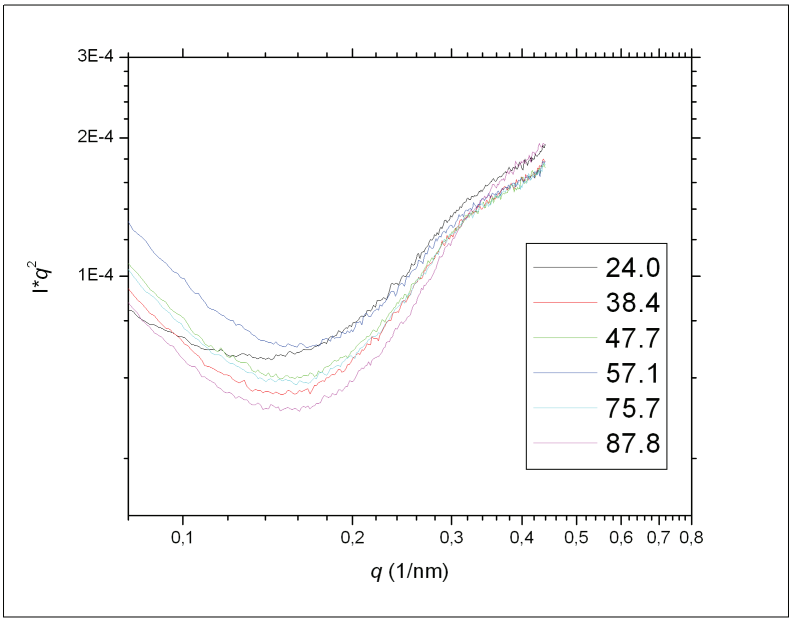

Figure 4.36: The scattered intensity multiplied by q^2 vs. q of sample C3 for various temperatures. This is frame 3, approximately 5 mm above the bottom of the capillary.

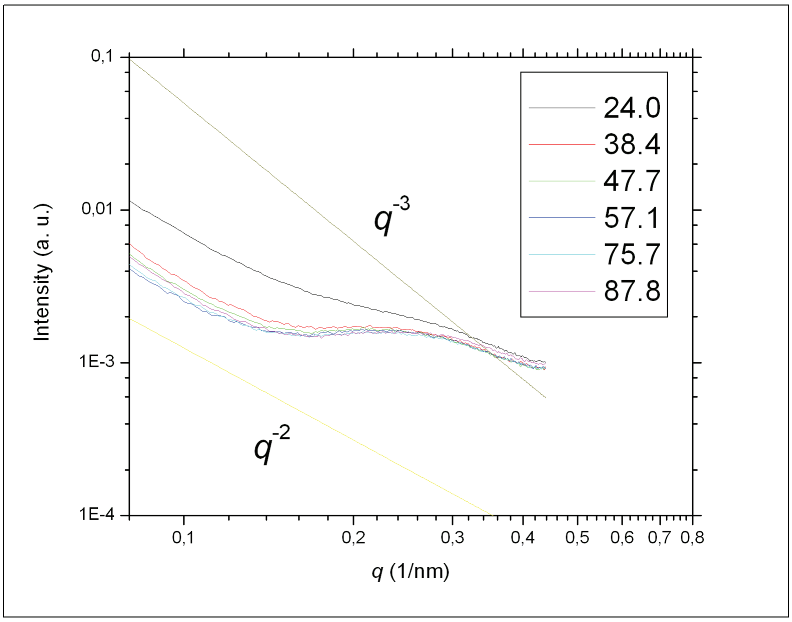

Figure 4.37: The scattered intensity vs. the scattering vector q of sample C3 for various temperatures. This is frame 6, approximately 11 mm above the bottom of the capillary.

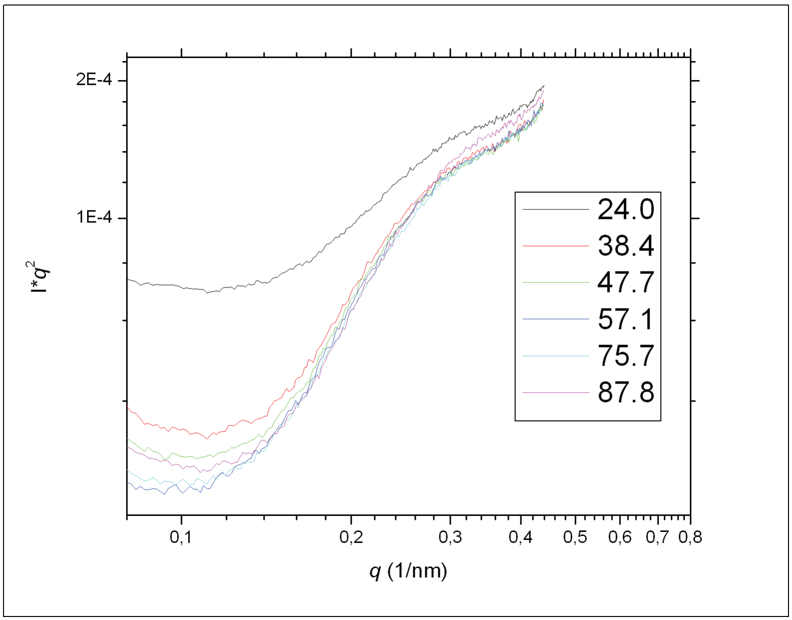

Figure 4.38: The scattered intensity multiplied by q^2 vs. q of sample C3 for various temperatures. This is frame 6, approximately 11 mm above the bottom of the capillary.

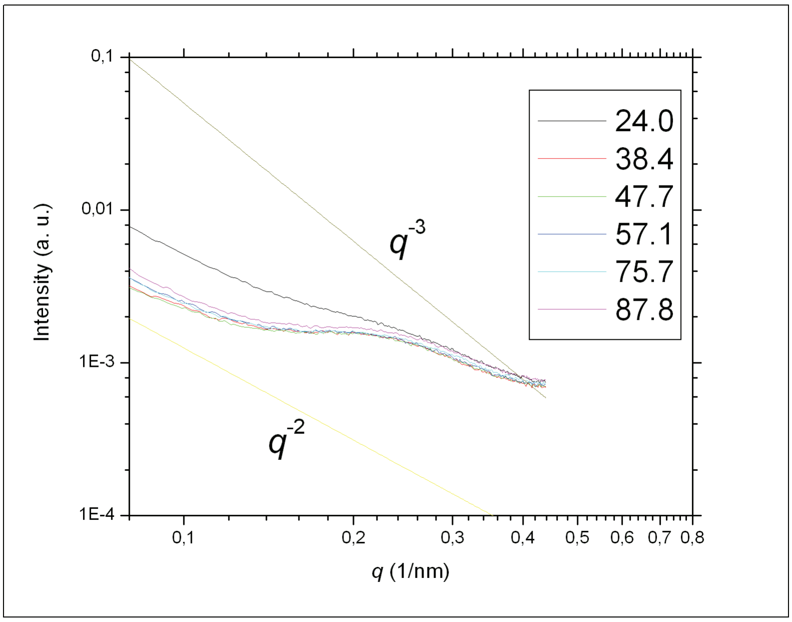

Figure 4.39: The scattered intensity vs. the scattering vector q of sample C3 for various temperatures. This is frame 10, approximately 19 mm above the bottom of the capillary.

C4

All the diffractograms of sample C4 are in the montage in Figure 4.43. This montage does not behave as well as the others, as both the coloumns and the rows show irregular patterns. E. g. coloumn 4 and 5 look different than other coloumns for several rows. This could be due to the motor trouble mentioned in the experimental section, but there is of course possible that the behaviour reflects actual changes in the sample. No matter how the motor was or was not troubled, it could look like the difference in appearance from one diffractogram to the next, in the vertical direction, is bigger for this sample than for the others.

There are several anisotropic patterns in this montage, and it is noteworthy that the anisotropicity seemingly increases for frame 16, at the bottom of the montage, when the temperature is increased. The plot of scattered intensity vs. azimuthal angle for all heights at 38 degrees in Figure 4.44 indicates that none of the frames are very anisotropic. That some of the frames have become more anisotropic after heating is confirmed by the corresponding plot at 76 degrees in Figure 4.45.

Figure 4.46 and 4.47 indicates that temperature does not alter the

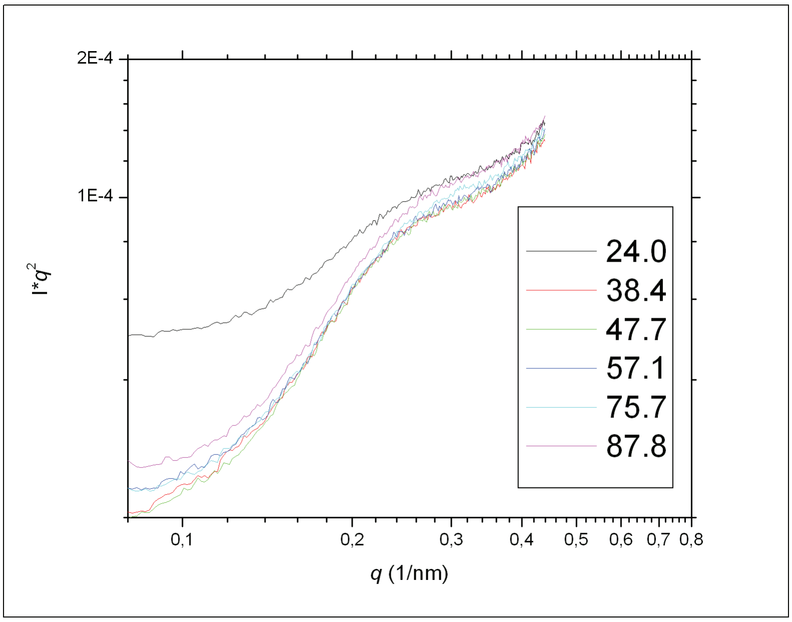

Figure 4.40: The scattered intensity multiplied by q^2 vs. q of sample C3 for various temperatures. This is frame 10, approximately 19 mm above the bottom of the capillary.

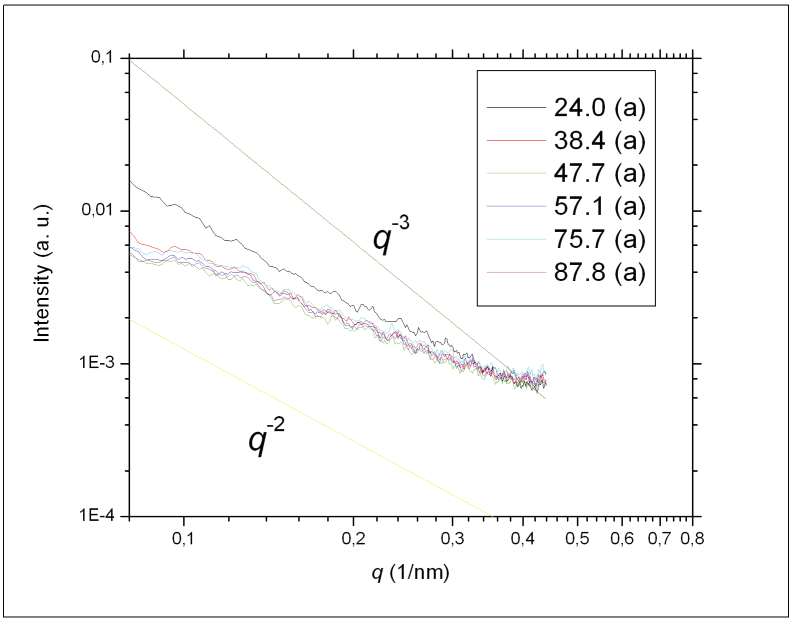

Figure 4.41: The scattered intensity vs. the scattering vector q of sample C3 for various temperatures. This is frame 14, approximately 27 mm above the bottom of the capillary.

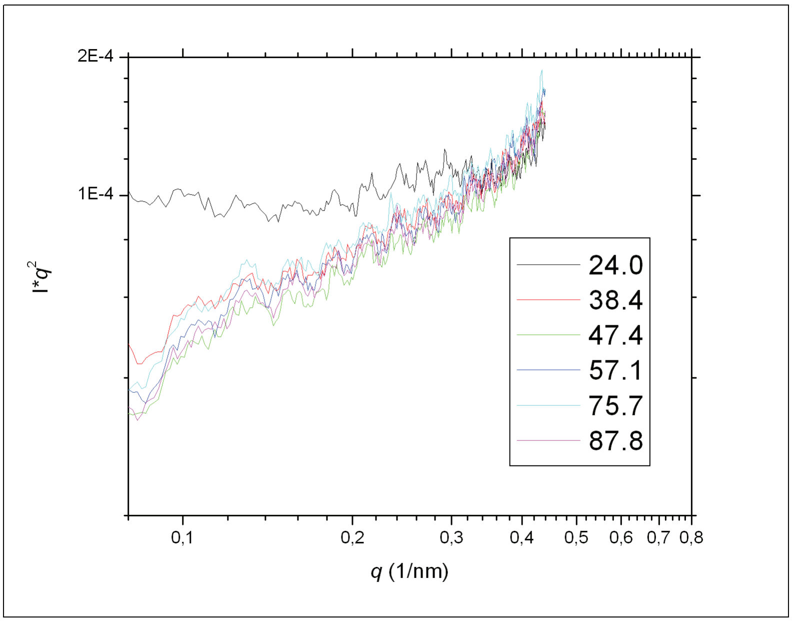

Figure 4.42: The scattered intensity multiplied by q^2 vs. q of sample C3 for various temperatures. This is frame 14, approximately 27 mm above the bottom of the capillary.

behaviour of the intensity as a function of the scattering vector as dramatic as for samples C1 and C3, except for the two curves representing 57 degrees. As the question regarding the possible motor trouble is unanswered, it is hard to conclude whether this behaviour is real or not. The corresponding plots for frame 4 in Figures 4.48 and 4.49 does not indicate large temperature effects. The most interesting feature of these plots for frame 7, shown in Figures 4.50 and 4.51 is that the slope of the 24 degrees curve is less steep than the others for $q > 0.16$ nm^{-1}. As indicated in the montage, the 57 degrees diffractograms are not like the others. Figures 4.52 and 4.53 reveals this by showing how the intensity falls off slower for this temperature. This plot also reveals that the intensity does not drop in the same, systematic manner as samples C1 and C3. Whether this is due to the lower salt concentration, motor trouble, or something else, is hard to say with the evidence at hand.

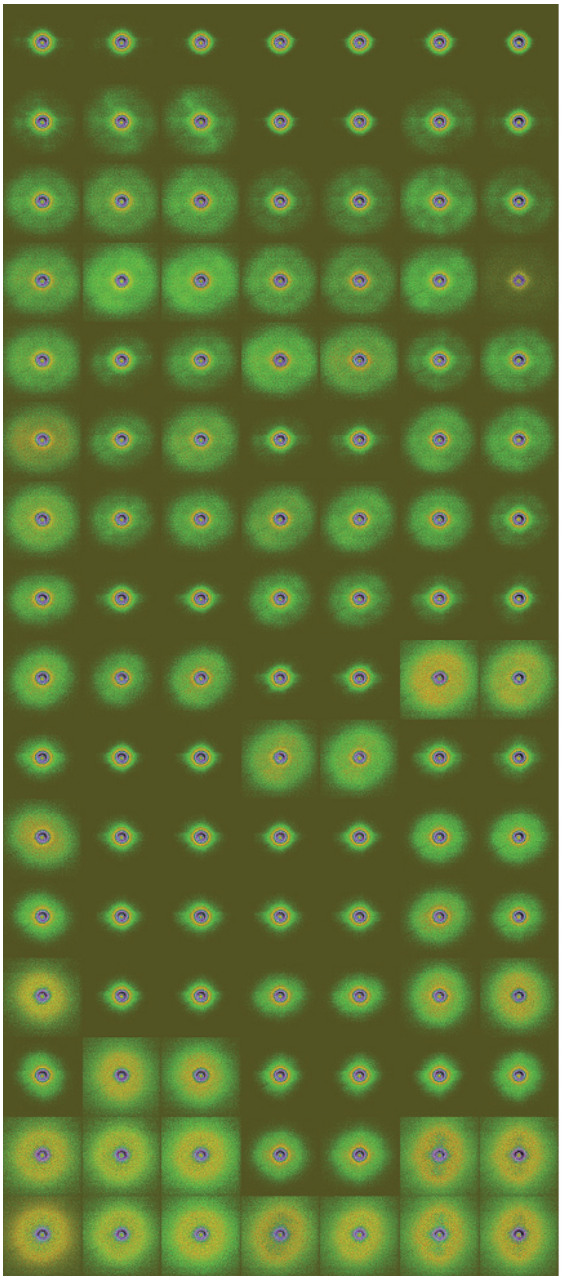

Figure 4.43: This is a montage of the diffractograms from sample C4. They are scaled and normalized in order to try and show the emerging peaks. The coloumns are representing one temperature each. From left to right: 24, 38, 48, 57, 57, 76 and 88 degrees. Vertically, the topmost frames are frame 1, i.e. around the bottom at the capillary. Going down the coloumn corresponds to going up in the capillary. The vertical step size is 2 mm, thus making the frame at the bottom of the figure approximately 31 mm above the bottom of the capillary.

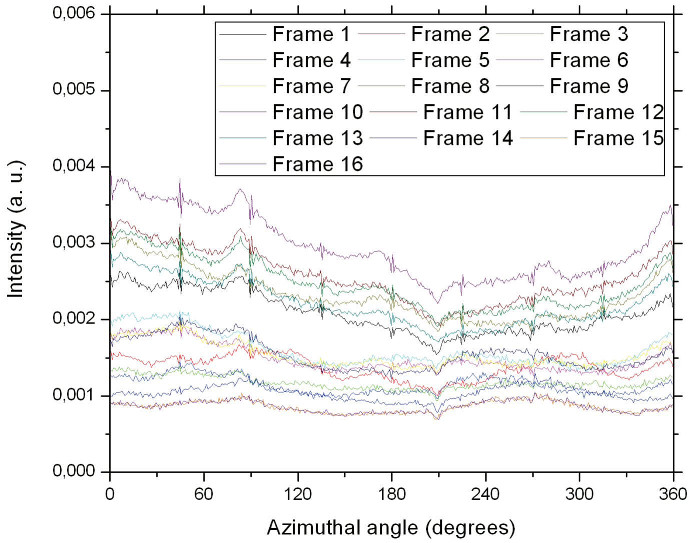

Figure 4.44: Azimuthal variations of the scattered intensity of sample C4 for various heights. The sample held a temperature of 38 degrees. Frame 1 is approximately 1 mm above the bottom of the capillary. The other frames are recorded going stepwise towards the top of the capillary, 2 mm per step.

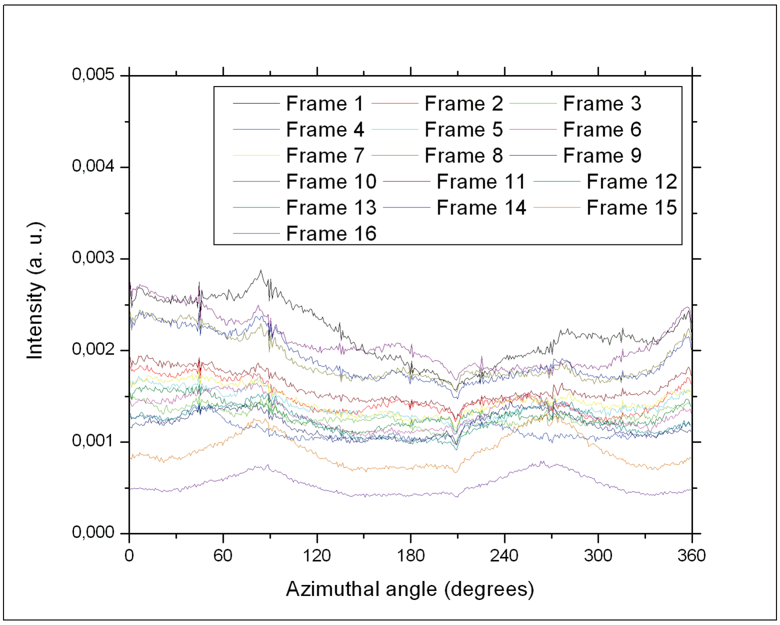

Figure 4.45: Azimuthal variations of the scattered intensity of sample C4 for various heights. The sample held a temperature of 76 degrees. Frame 1 is approximately 1 mm above the bottom of the capillary. The other frames are recorded going stepwise towards the top of the capillary, 2 mm per step.

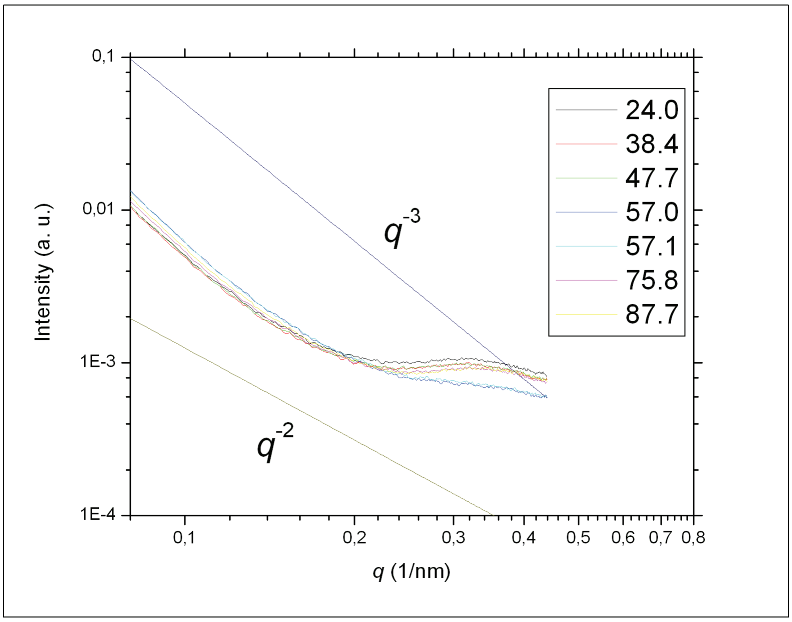

Figure 4.46: The scattered intensity vs. the scattering vector q of sample C4 for various temperatures. This is frame 1, approximately 1 mm above the bottom of the capillary.

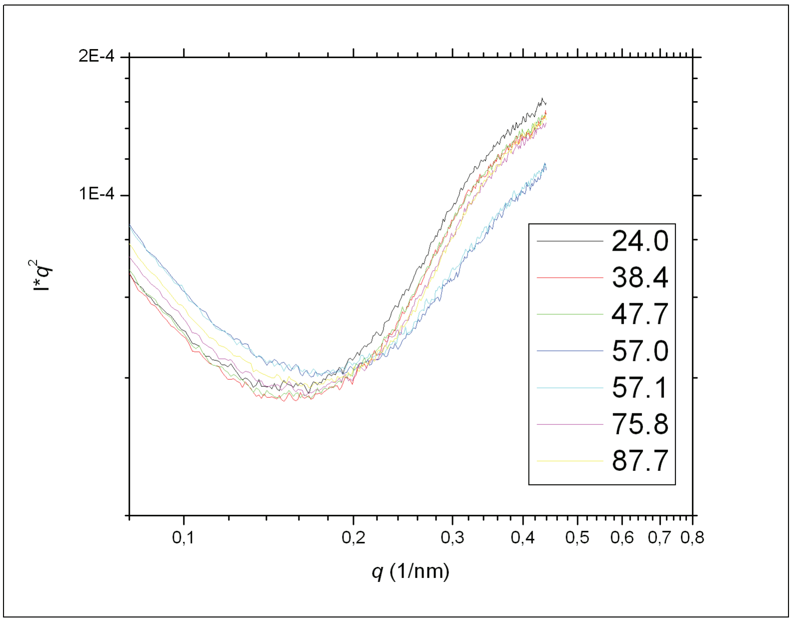

Figure 4.47: The scattered intensity multiplied by q^2vs. the q of sample C4 for various temperatures. This is frame 1, approximately 1 mm above the bottom of the capillary.

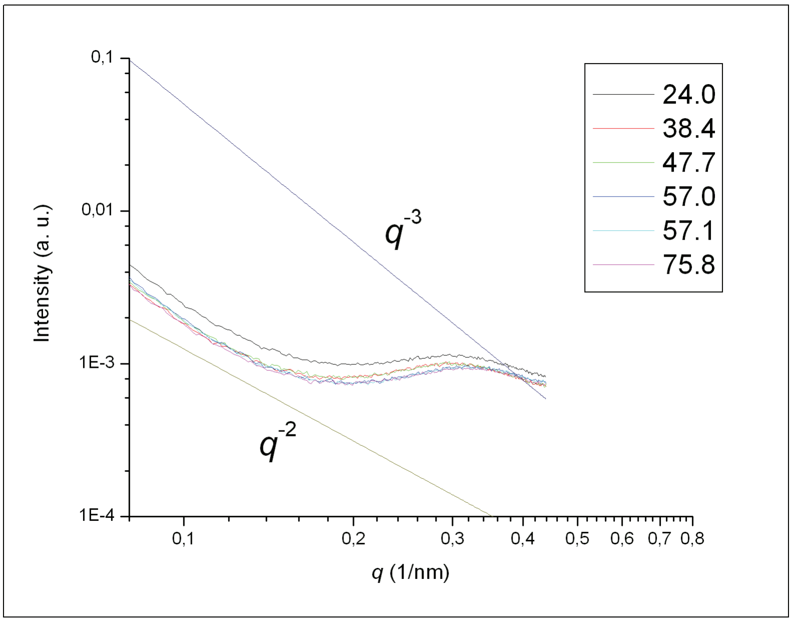

Figure 4.48: The scattered intensity vs. the scattering vector q of sample C4 for various temperatures. This is frame 4, approximately 7 mm above the bottom of the capillary.

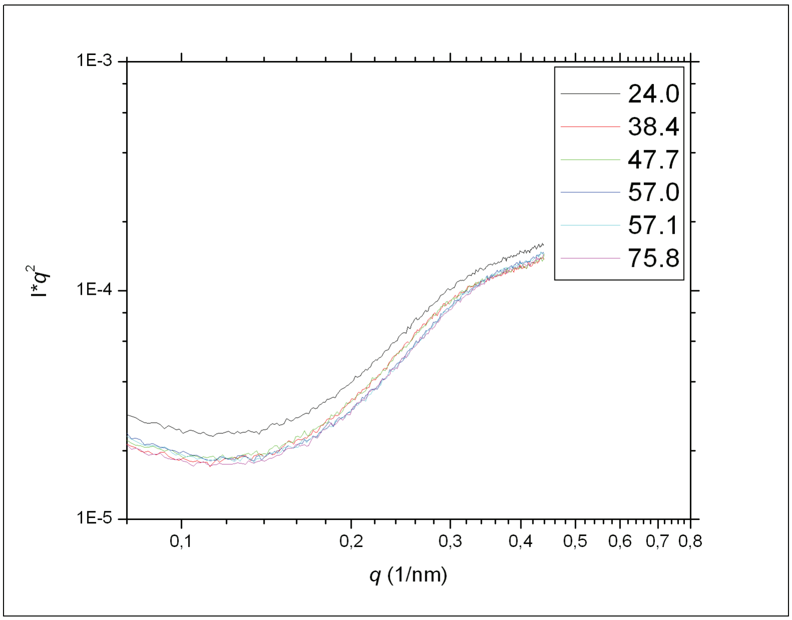

Figure 4.49: The scattered intensity multiplied by q^2vs. the q of sample C4 for various temperatures. This is frame 4, approximately 7 mm above the bottom of the capillary.

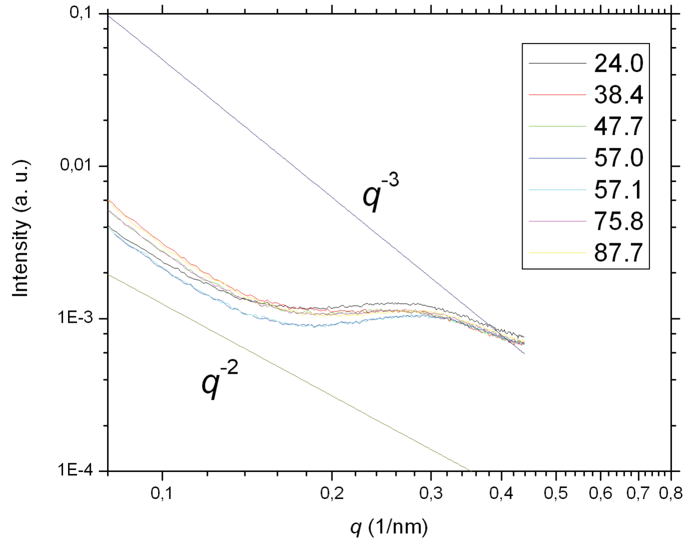

Figure 4.50: The scattered intensity vs. the scattering vector q of sample C4 for various temperatures. This is frame 7, approximately 13 mm above the bottom of the capillary.

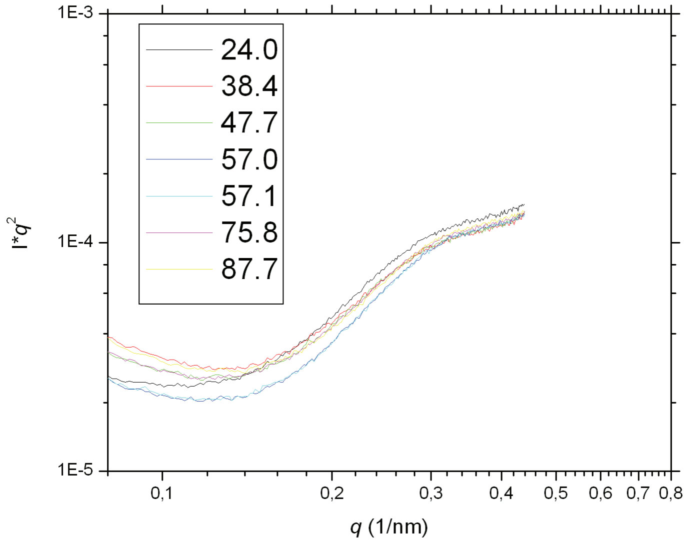

Figure 4.51: The scattered intensity multiplied by q^2vs. the q of sample C4 for various temperatures. This is frame 7, approximately 13 mm above the bottom of the capillary.

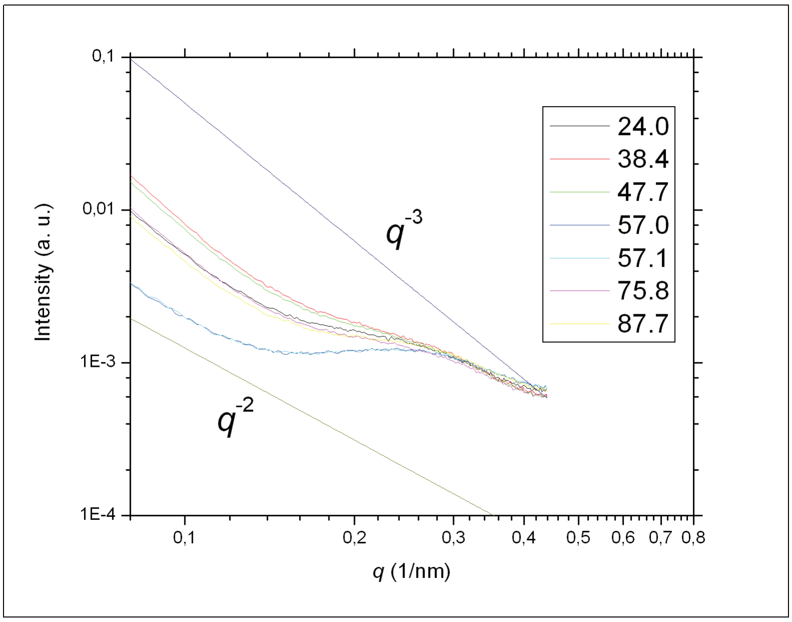

Figure 4.52: The scattered intensity vs. the scattering vector q of sample C4 for various temperatures. This is frame 10, approximately 19 mm above the bottom of the capillary.

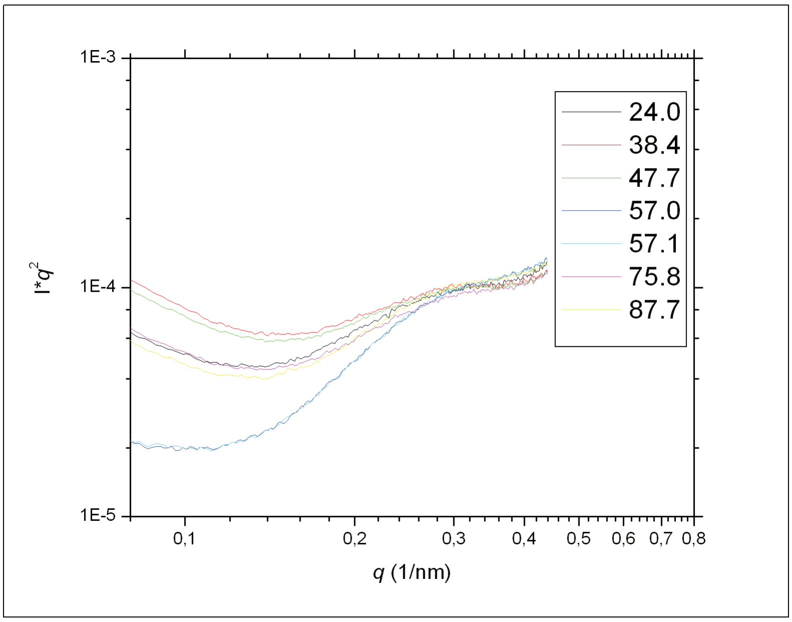

Figure 4.53: The scattered intensity multiplied by q^2vs. the q of sample C4 for various temperatures. This is frame 10, approximately 19 mm above the bottom of the capillary.

C5

Figure 4.54 shows sample C5 between crossed polarizers before heating. It is evident that the sample becomes more isotropic as one progress towards the top, as a smaller amount of light passes through the crossed polarizers from this area. Looking at the montage in Figure 4.55, this seem to hold quite well, as none of the diffractograms in the far left coloumns seem to be very anisotropic. However, it seems to be the case that e.g. frame 15, at the bottom of the montage, develops some kind of anisotropicity as the sample is heated from 24 degrees to 38 and 48 degrees. Interestingly, when the sample is heated further, it looks more isotropic.

The plots of the scattered intensity vs. the azimuthal angle for this sample support that the sample is more anisotropic before heating, as evident from Figures 4.56 and 4.57, which represents the lowest and highest temperature investigated, respectively. Looking exclusively at the temperature development of the azimuthal distribution of scattered intensity for frame 4, in Figure 4.58, it seems that only the two lowest temperatures shows any clear anisotropicity.

Plots of the scattered intensity vs. the scattering vector q in Figure 4.59 indicates that the intensity follows q^{-2} quite closely. When the temperature is increased, this behaviour is interrupted somewhere beween $q \approx 0.1$ - 0.2 nm^{-1}, as evident from Figures 4.59, 4.61 and 4.62. Now, consider the log-log plot of the scattered intensity multiplied by q^2 vs. q for sample C5, frame 2, at 88 degrees, from Figure 4.64. It seems to be the case, as it was for sample C1, that the intensity drops in the lower q-range studied when the temperature is increased. In the high-end q-range, the intensities of the different temperature curve seem to be almost the same. The drop in intensity is also more prominent in the lower frames, as evident from Figures 4.63 to 4.72.

Figure 4.54: Picture of sample C5 between crossed polarizers.

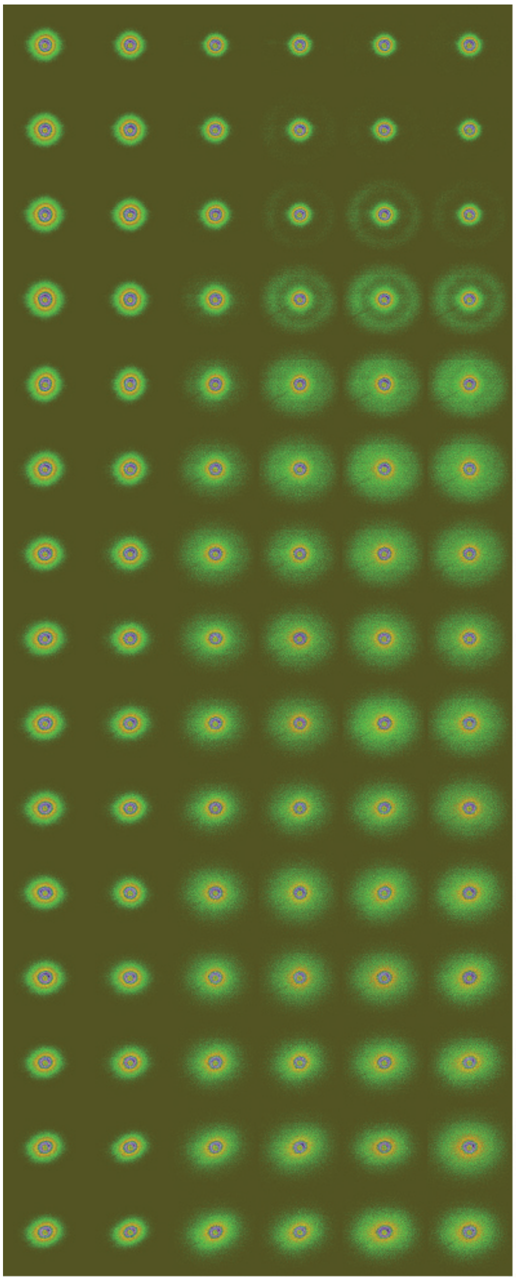

Figure 4.55: This is a montage of the diffractograms from sample C5. They are scaled and normalized in order to try and show the emerging peaks. The coloumns are representing one temperature each. From left to right: 24, 38, 48, 57, 76 and 88 degrees. Vertically, the topmost frames are frame 1, i.e. around the bottom at the capillary. Going down the coloumn corresponds to going up in the capillary. The vertical step size is 2 mm, thus making the frame at the bottom of the figure approximately 29 mm above the bottom of the capillary.

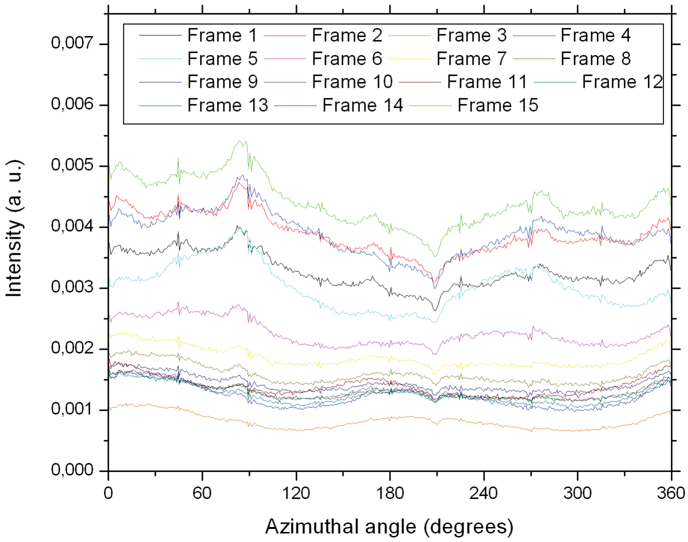

Figure 4.56: Azimuthal variations of the scattered intensity of sample C5 for different heights. The sample held a temperature of 24 degrees.

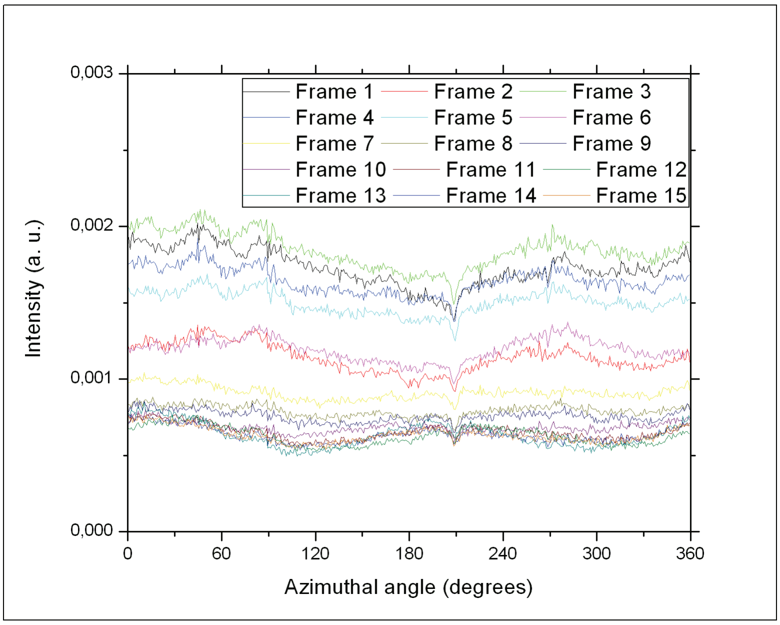

Figure 4.57: Azimuthal variations of the scattered intensity of sample C5 for different heights. The sample held a temperature of 88 degrees.

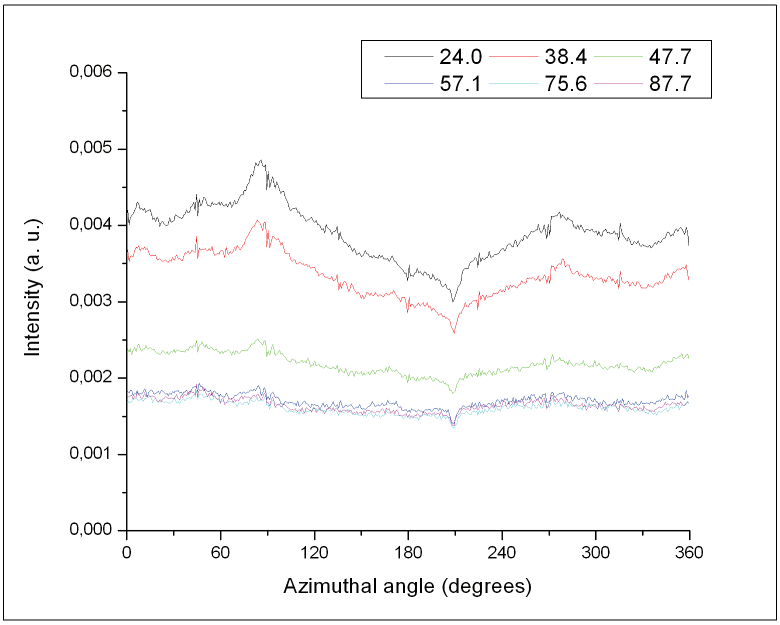

Figure 4.58: Azimuthal variations of the scattered intensity of sample C5 for different temperatures. This is frame 4, approximately 7 mm above the bottom of the capillary.

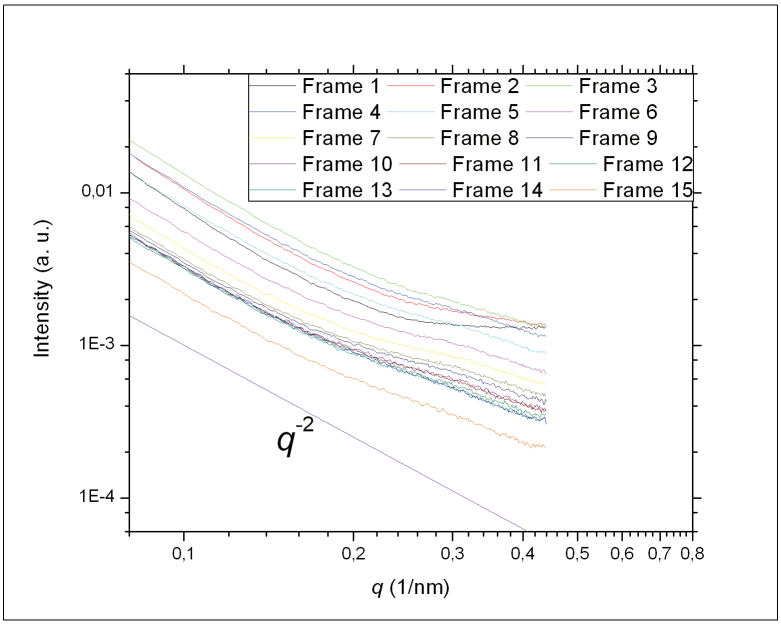

Figure 4.59: The scattered intensity of sample C5 vs. the scattering vector q for various heights. The sample held a temperature of 38 degrees. Frame 1 is approximately 1 mm over the bottom of the capillary. The other frames are recorded going stepwise towards the top of the capillary, 2 mm per step.

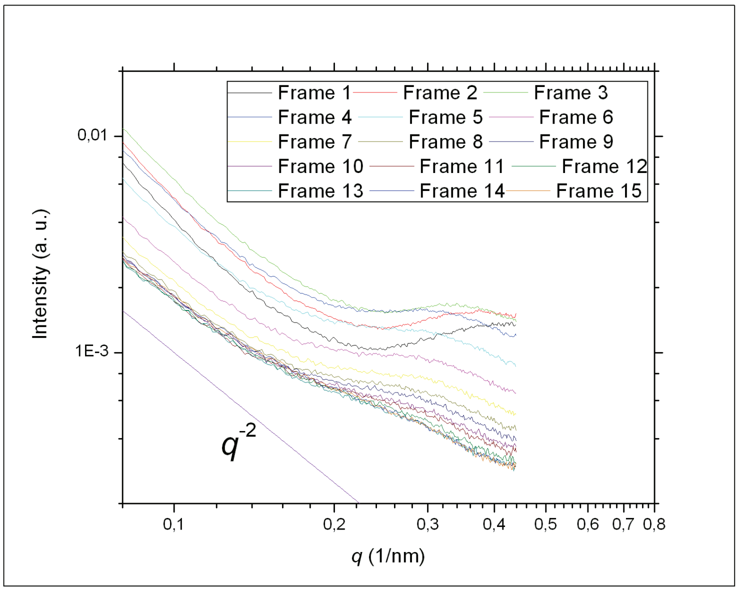

Figure 4.60: The scattered intensity of sample C5 vs. the scattering vector q for various heights. The sample held a temperature of 48 degrees. Frame 1 is approximately 1 mm over the bottom of the capillary. The other frames are recorded going stepwise towards the top of the capillary, 2 mm per step.

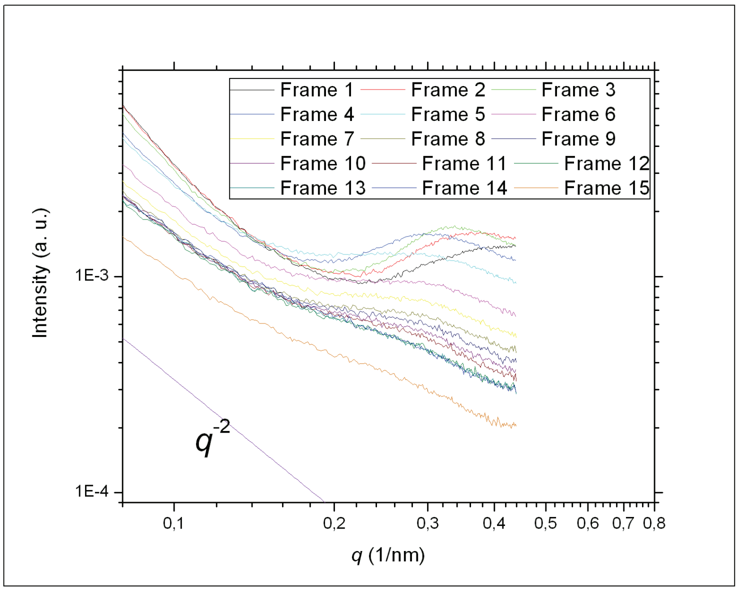

Figure 4.61: The scattered intensity of sample C5 vs. the scattering vector q for various heights. The sample held a temperature of 57 degrees. Frame 1 is approximately 1 mm over the bottom of the capillary. The other frames are recorded going stepwise towards the top of the capillary, 2 mm per step.

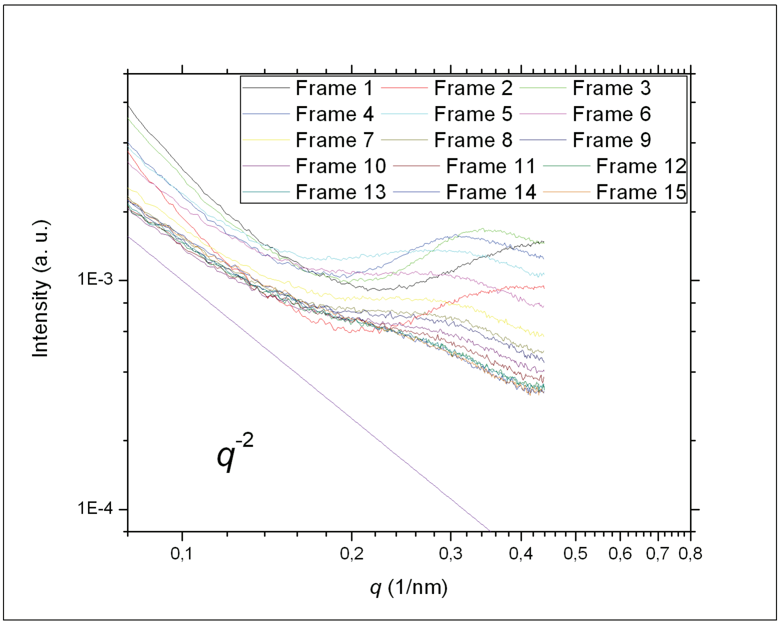

Figure 4.62: The scattered intensity of sample C5 vs. the scattering vector q for various heights. The sample held a temperature of 88 degrees. Frame 1 is approximately 1 mm over the bottom of the capillary. The other frames are recorded going stepwise towards the top of the capillary, 2 mm per step.

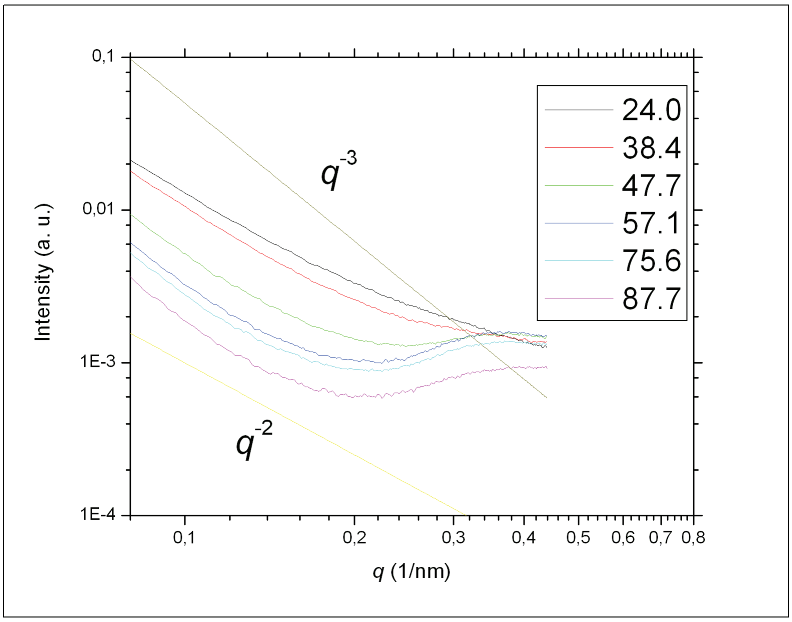

Figure 4.63: The scattered intensity vs. the scattering vector q of sample C5 for various temperatures. This is frame 2, approximately 3 mm above the bottom of the capillary.

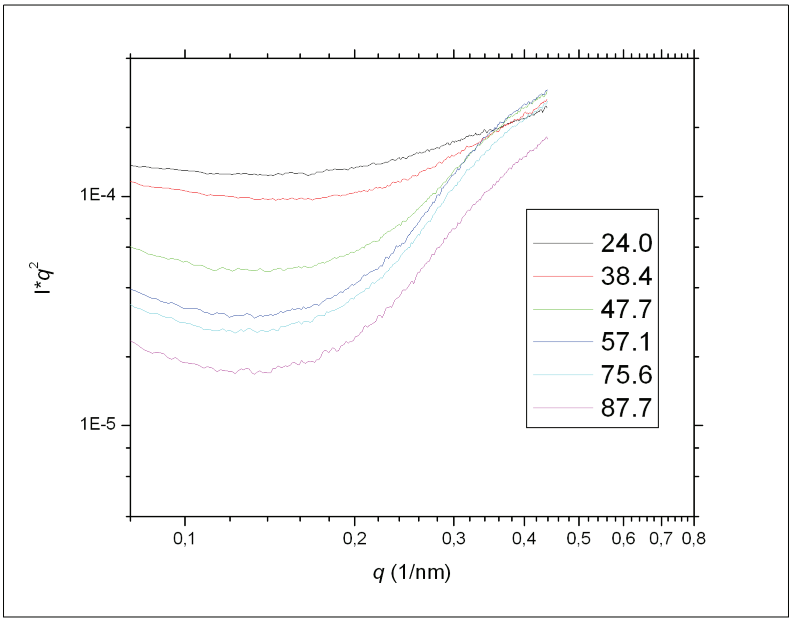

Figure 4.64: The scattered intensity multiplied by q^2 vs. q of sample C5 for various temperatures. This is frame 2, approximately 3 mm above the bottom of the capillary.

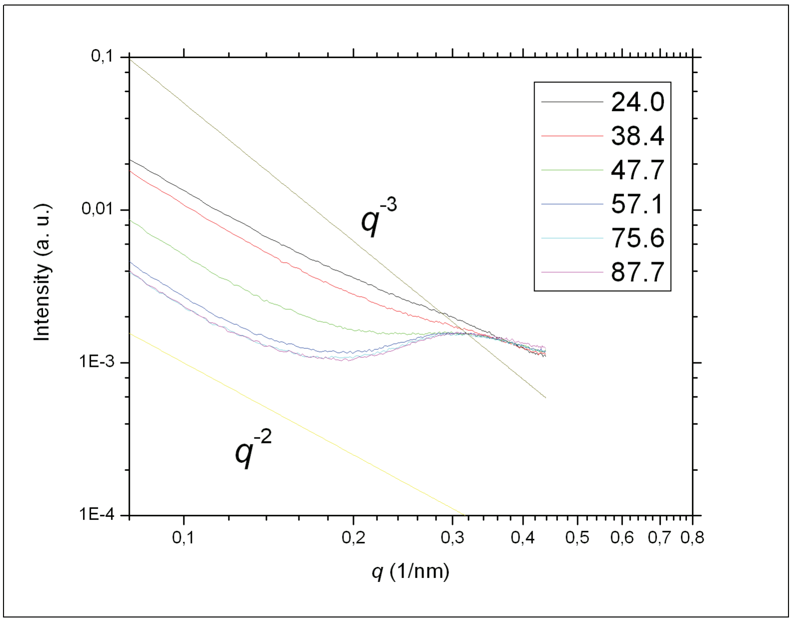

Figure 4.65: The scattered intensity vs. the scattering vector q of sample C5 for various temperatures. This is frame 4, approximately 7 mm above the bottom of the capillary.

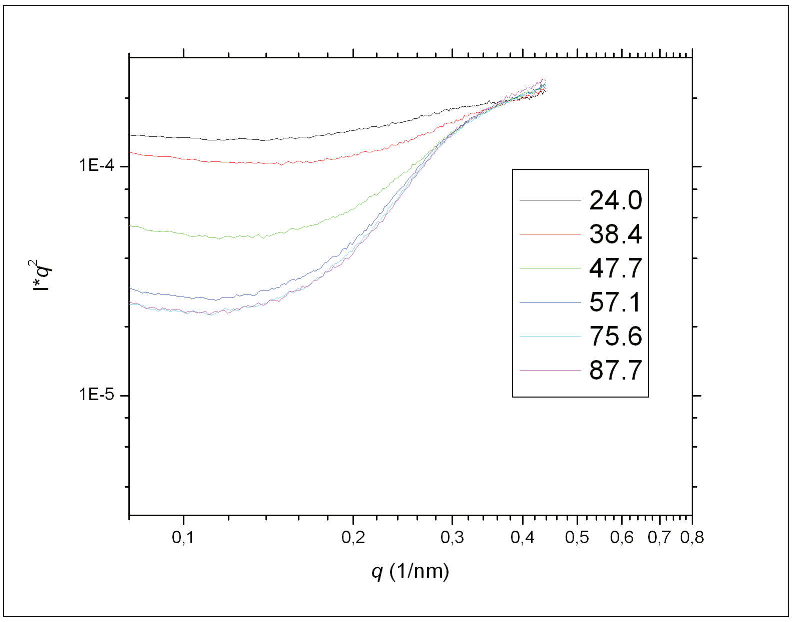

Figure 4.66: The scattered intensity multiplied by q^2 vs. q of sample C5 for various temperatures. This is frame 4, approximately 7 mm above the bottom of the capillary.

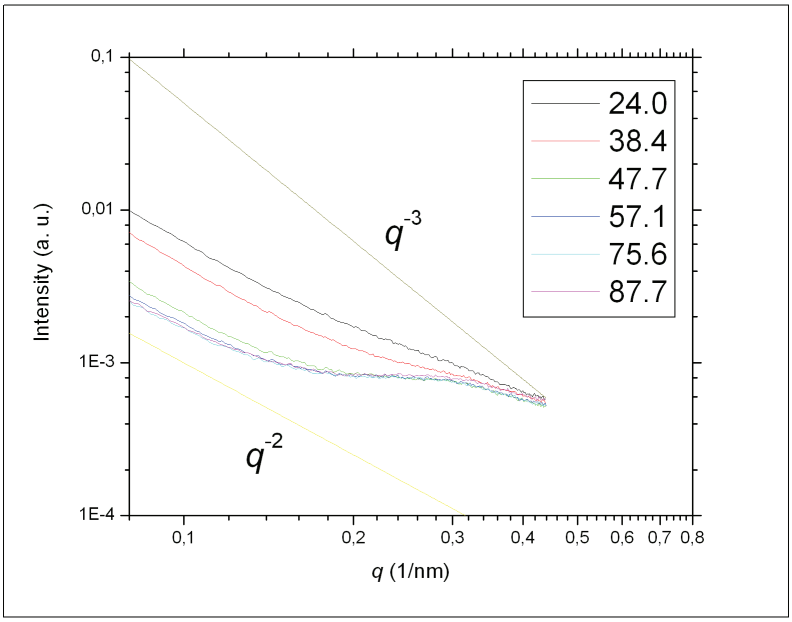

Figure 4.67: The scattered intensity vs. the scattering vector q of sample C5 for various temperatures. This is frame 7, approximately 13 mm above the bottom of the capillary.

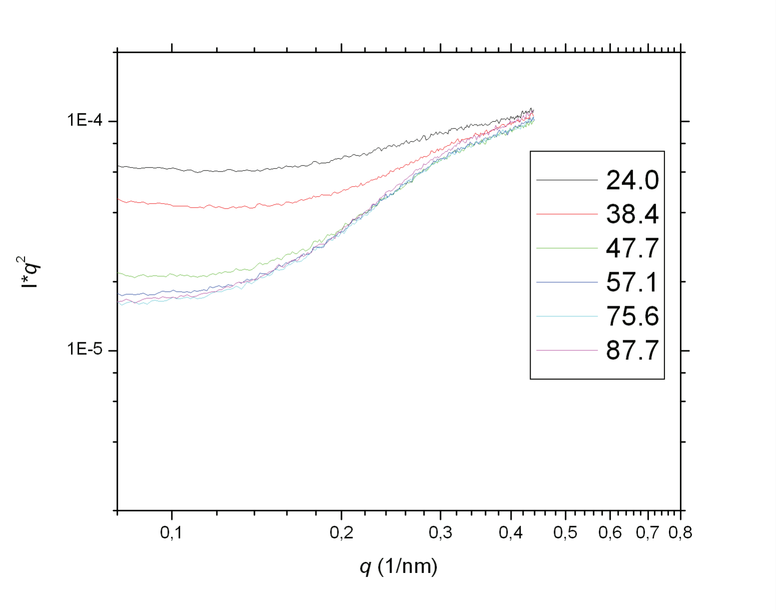

Figure 4.68: The scattered intensity multiplied by q^2 vs. q of sample C5 for various temperatures. This is frame 7, approximately 13 mm above the bottom of the capillary.

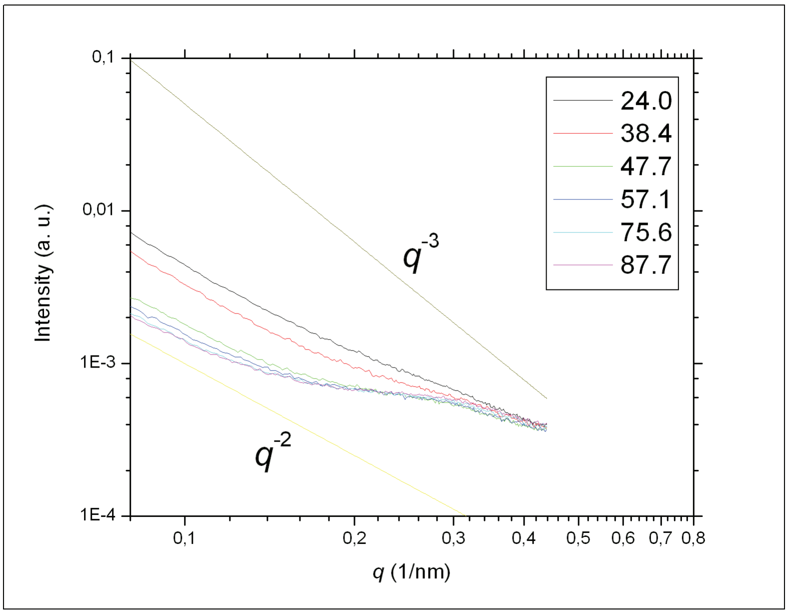

Figure 4.69: The scattered intensity vs. the scattering vector q of sample C5 for various temperatures. This is frame 10, approximately 19 mm above the bottom of the capillary.

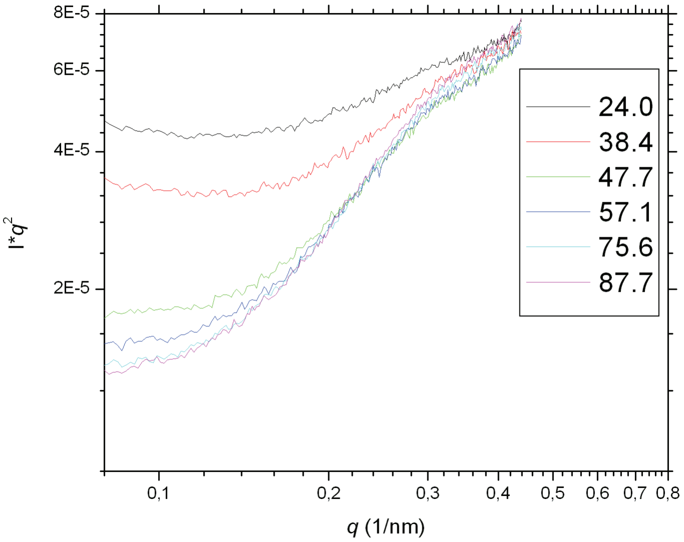

Figure 4.70: The scattered intensity multiplied by q^2 vs. q of sample C5 for various temperatures. This is frame 10, approximately 19 mm above the bottom of the capillary.

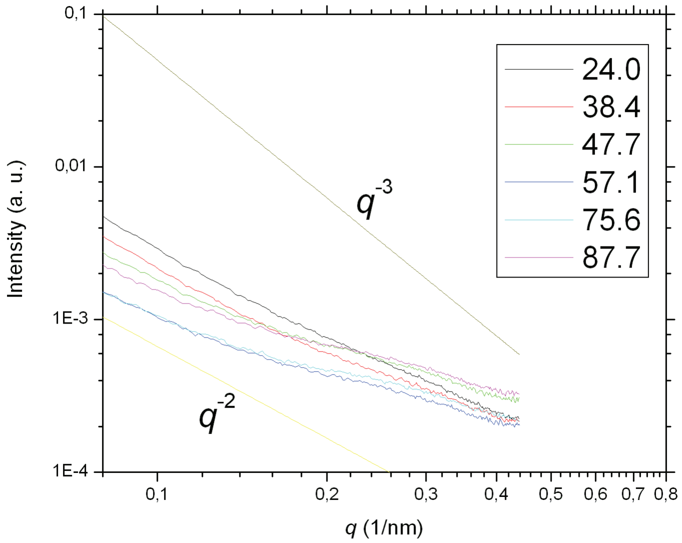

Figure 4.71: The scattered intensity vs. the scattering vector q of sample C5 for various temperatures. This is frame 15, approximately 29 mm above the bottom of the capillary.

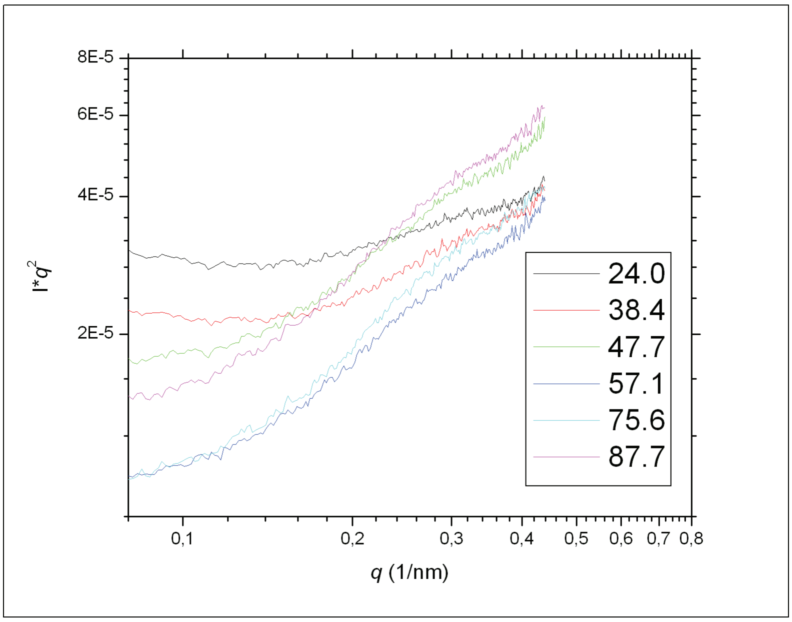

Figure 4.72: The scattered intensity multiplied by q^2 vs. q of sample C5 for various temperatures. This is frame 15, approximately 29 mm above the bottom of the capillary.

4.2 Discussion

In the results section, it was found that some heights in samples C1 and C5, both at 10 mM NaCl, became less anisotropic as the samples were heated. This was seen in Figures 4.2, 4.3 and 4.25 for sample C1, and in Figures 4.56 - 4.58 for sample C5. The methods used to find this, inspecting the diffractograms in the montage, the plots of the azimuthal distribution of the scattered intensity, and the iso-intensity ellipse eccentricities, are to some extent qualitative. It is possible to measure the anisotropicity in a more quantitative way by fitting a Gaussian curve to the peaks appearing in the azimuthal distribution. The characteristics of this peak, such as its full width at half maximum (FWHM), can then be used to find the order parameter S_2. This has been done in e.g. [19, 28]. Nevertheless, the trend of less anisotropicity as these samples were heated seems to be present for, at least, some heights. This was very evident in the plots of the eccentricity of iso-intensity ellipses. In addition, it was found that the scattered intensity for $q <\approx 0.3$ nm^{-1} decreased as the temperature increased. As the value of the scattering vector q approached 0.4 nm^{-1}, corresponding to a real-space distance of approximately 15 nm, the scattered intensity of the curves of the higher temperatures increased much faster than those at lower temperatures, as was seen in Figures 4.13 - 4.24. This, in turn, lead to the scattered intensity of all temperatures being at around the same intensity for $q \approx 0.4$ nm^{-1}. Can any conclusion be drawn from this? In the theory section the sizes of the particle dimensions were given. The particles are disc-like, and have a diameter that can be as large as 20 000 nm. The thickness varies, but each particle usually consists of 20 - 100 clay sheets. The average thickness, i.e. the average number of sheets in a particle, is larger for lower positions in the capillary, as is evident from Figure 2.3. As the sheets have a regular distance between them of 1.5 nm, the particles have to be from around 30 to 150 nm thick. These real-space distances can be transferred to the reciprocal space, where their values is given by the relation $q = \frac{2\pi}{d}$. This means that 30 and 150 nm represent $q \approx 0.2$ nm^{-1} and $q \approx 0.04$ nm^{-1}, respectively.

It is possible to imagine a scenario where the clay particles undergoes exfoliation upon heating, i.e. that some stacks of platelets split up, along the borderline between the individual sheets of the platelets, thus leaving behind a thin platelet and a thinner stack of platelets. The thinner stack of platelets could possibly exfoliate several times. Imagine, for the sake of the argument, that a particle stack consisting of 100 sheets undergoes exfoliation so many times that it end up as 100 platelets of one sheet each. All the other surrounding clay particles, for now, stay the same. A consequence of this particle exfoliating would be that the sample would have a smaller amount of planes having a certain distance, like $d = 50$ nm, between them. All the planes that had this distance between them in the now exfoliated particle would be gone. This would, in turn, probably lead to less scattering in the q-range corresponding to these certain real-space distances. This behaviour is seen for the frames in the sample C1 and C5 as the capillary is heated, e.g. in Figures 4.14 and 4.64, for the intensity multiplied by q^2 vs. q for sample C1 and C5, respectively. Also, it seems that this behaviour becomes somewhat less pronounced as one progress upwards in the capillary. As Figure 2.3 indicated, the average thickness of the particle stacks decreases as the height above the capillary is increased. Therefore, it is possible that the reduction in scattered intensity at q-values corresponding to thick particle stacks becomes less pronounced at higher positions, simply because these heights had fewer thick particles to begin with. That the slope of the intensity vs. q becomes steeper for low q-values as the temperature is increased, could mean that the platelets that result from exfoliation increase the area that the x-ray beam can scatter from. As the scattered intensity from smooth surfaces falls off like q^{-4} [16], the steeper slope can be thought of as a consequence of this. However, it is not known whether the surface of NaFh particles are smooth, as seen by the x-ray beam, or not. Any strong statements regarding this should therefore not be made.

That the anisotropicity for one particular spot in the capillary as a whole seem to decrease when the temperature is increased, does not necessarily mean that the platelets are isotropically oriented. The total isotropicity could also be the result of several small, ordered domains. When taking into consideration that the beam is 0.2 mm × 0.3 mm, i.e. much bigger than the thickness of the particle and also 10 times bigger than the diameter of the biggest particles, this could certainly be the case. However, if the particles in such small domains initially were organized such as to give rise to anisotropic scattering, it is unlikely that exfoliation would have lead to isotropic scattering if the small domains were to remain after the exfoliation. If the exfoliation lead to the small domains breaking up, much more volume would be available to the clay particles. In this way, reorganization from anistropic to isotropic could occur.

A scenario that could explain the behaviour discussed is shown in Figures 4.73 and 4.74. The first figure shows the situation before heating. There are some degree of ordering, and the particles have not yet exfoliated. The particles shown could be part of a small domain, or part of a larger structure of ordered particles. In the second figure, in which one of the particles have exfoliated into several, thinner particles, the order of these particles is very evident. Because each of the newly formed particles has an electric double layer, the volume which the particles might occupy become much smaller. The five particles demand more space than the old, bigger one, and as Onsager proposed, one way to deal with this is simply to organize in a more orientationally ordered fashion. As indicated in the last figure, the other particles are likely to be pushed away as the electric double layers of the newly formed particles come in contact with those of the other particles.

Now, if the particles were initially a part of a small domain, the particles surrounding the exfoliated particles have the chance to move out of the way, thus breaking up the small domains. This could lead to less overall anisotropicity. On the other hand, if the particles were part of a bigger, ordered structure, the particles surrounding the exfoliated particle might not have the chance to move. Thus, the particles could organize in an even more anisotropic manner to deal with the new situation.

The spatial extent of the electric double layer is determined by the Debye length λ_D. As was seen in the theory section, $\lambda_D \propto \sqrt{\frac{T}{c}}$. This means that temperature does not affect the Debye length dramatically in the temperature interval studied in this thesis. The effects of different salt concentration in the samples studied are likely to be more important, as they range from 10^{-4} M to 10^{-2} M.

When looking at sample C4, which has a salt concentration of 10^{-4} M, is is evident that the anisotropicity increases with temperature for e.g. frame 16. Thinking of the low salt concentration, leading to a reduced screening effect, it could be imagined that any possible exfoliation forces the particles to orient in the same direction in order to cope with the new situation of more particles, as explained above. This could also explain why the intensity does not drop in the same manner as did sample C1 and C5, as exfoliation might not be energitically as favourable for this salt concentration.

Sample C3, which contained 10^{-3} M of salt, did not seem to produce the same changes in the azimuthal distribution of the scattered intensity as C1 and C5 did. However, no strong statements can be made about this without a more stringent analysis, e.g. to find the order parameter S_2. However, it is possible to see the behaviour of scattered intensity vs. the scattering vector shown by C1 and C5 in the plots from this sample. Figure 4.37 shows how the intensity at the higher temperatures is lower than that of the 24 degrees curve

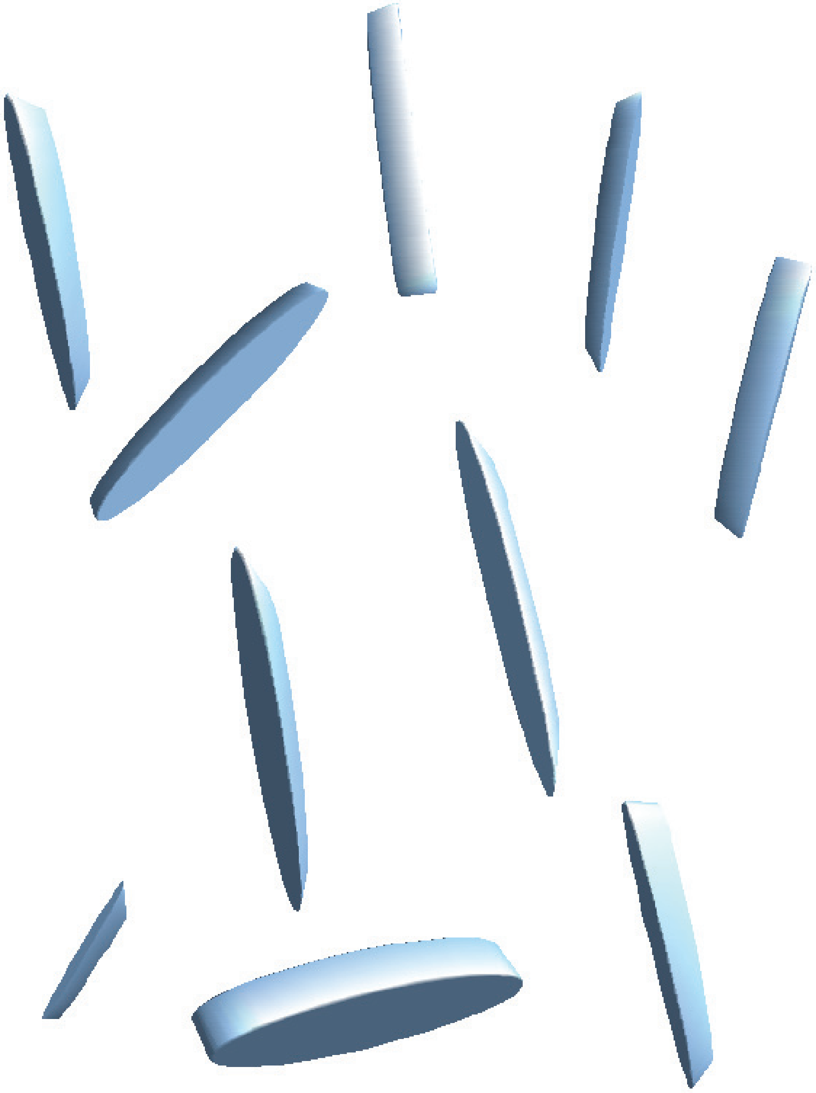

Figure 4.73: An illustration of the ordering of the platelets before heating. The particles are large, and they are somewhat ordered. The group of particles illustrated could be part of a small domain, or part of a larger structure.

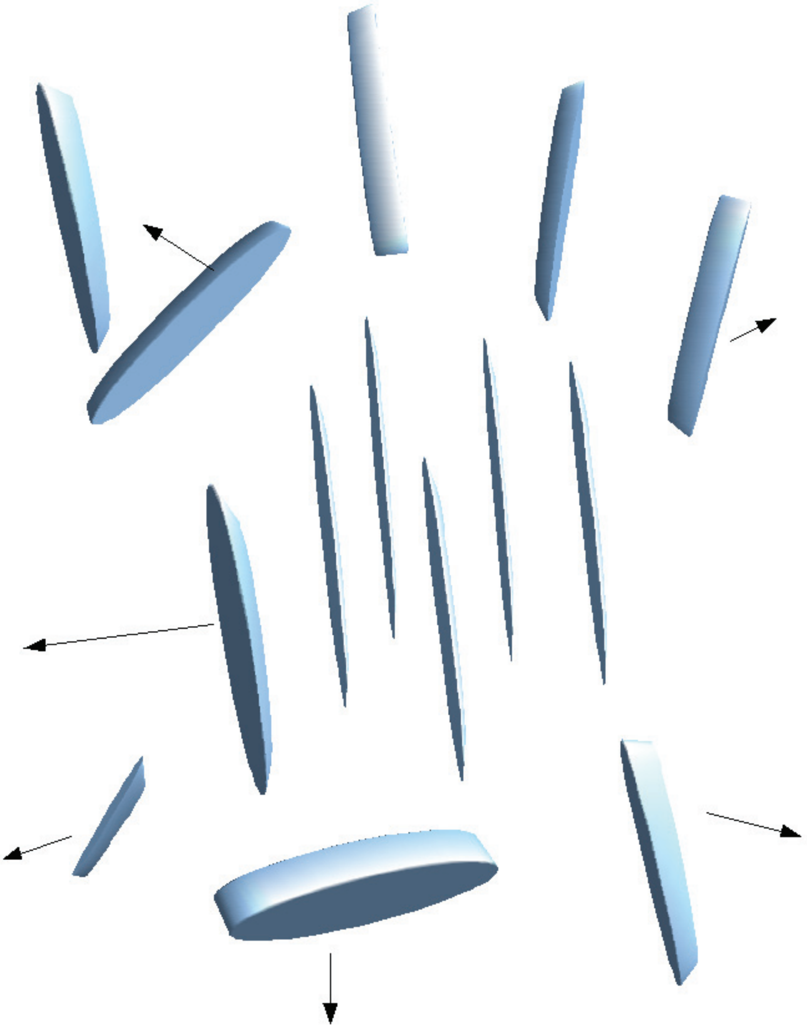

Figure 4.74: As the temperature is increased, exfoliation of the particles begin. This leads to the newly formed particles adopting an ordered structure. If the particles are part of a sample with low salt concentration, the screening effect will be small. The particles surrounding an exfoliation might not be able to give way, thus forcing the newly created particles, and their neighbours, to adopt an even more ordered organization. For higher salt concentrations, the particles are more likely to be organized in small, ordered domains. In this case, the particles surrounding an exfoliated particle will be more likely to give way, thus breaking up the small domains. This process could lead to less overall anisotropicity. That one particle exfoliates into five particles is due to illustrational purposes.

for $q <\approx 0.25$ nm^{-1}, before the low and high temperature curves approach each other when $q \approx 0.4$ nm^{-1}. However, the drop in intensity for the high temperature curves compared to the 24 degrees curve is not as large as it was for sample C1 and C5. This could be due to the lower concentration of salt in C3, leading to a smaller screening effect. Thus the particles can not be allowed to be as close to each other as they can in the 10^{-2} M solutions. This, in turn, could decrease the chance of exfoliation. This would place the behaviour of this sample naturally between that of the samples of high salt concentration, on one side, and the sample with low salt concentration, on the other side.

Chapter 5

Conclusion and suggestions for future studies

Colloidal dispersions of platelet-shaped particles may organize into liquid crystalline phases, given certain conditions. The polydisperse clay sodium fluorohectorite (NaFh), which previous studies have revealed to exhibit coexisting isotropic and nematic phases in aqueous dispersions [10, 12, 36], is known to develop regions with nematic ordering, depending on the concentration of clay and ionic strength, as well as confinement. Using small angle x-ray scattering techniques, it is found that positional correlations set in upon increasing the temperature from room temperature to around 40 °C.
The intensity at q-values corresponding to real-space distances of typical particle thicknesses becomes lower as the temperature is increased. This, together with a marked change of the slope of the intensity for $q \approx 0.1$ nm^{-1}, corresponding to a real-space distance of approximately 60 nm, indicates that exfoliation of particles takes place. Exfoliation could explain the observed behaviour as it would lead to a decrease of the characteristic distances that leads to scattering in the q-range that experiences a drop in intensity. The slope could, at least in part, be explained by the increase of area from which the x-ray beam can scatter from.
The salt concentration seems to play an important role regarding to what extent exfoliation is observed. For a 10^{-2} M concentration of salt, the intensity drop indicating exfoliation is more pronounced than it is for lower salt concentrations. The intensity drop is barely observable for concentrations of 10^{-4} M, although the observed increase of anisotropicity for some heights in the capillary of this concentration indicates that some exfoliation might have taken place. For an intermediate salt concentration of 10^{-3} M, the effects believed to be caused by exfoliation are present, but not as marked as

they were for higher concentrations.

Analyzing the diffractograms and investigating the resulting plots, I have found many features, but I would certainly not be surprised to have missed exciting and also important features during this procedure. Also, a more thorough analysis, where the anisotropicity of the samples is investigated in further detail, to infer the order parameter S_2 and to find the eccentricity of iso-intensity cuts of the scattering profiles, could reveal more of the nature of colloidal dispersions of NaFh upon heating.

Looking at the samples as they heat, using crossed polarizers, was not possible at the time that this thesis was written. Doing this, to see if what has been indicated by the SAXS experiments can be confirmed, is a natural step in the still ongoing investigations of temperature induced effects in colloidal dispersions of NaFh.

In the experiment in Grenoble, on which large parts of this thesis is based, more samples than I have analyzed here were experimented on. Analyzing these diffractograms, as well as those from a similar experiment that took place at MAX-lab, Lund, Sweden in June 2010, is an obvious way of revealing more of the behaviour of NaFh dispersions upon heating.

In addition to this, it would certainly be interesting to investigate the temperature interval in which the positional correlations evolve in more detail, both using SAXS and crossed polarizers. It would also be interesting to investigate the temperature effects using wide angle x-ray scattering.

Electromagnetic waves

Electromagnetism

Maxwell's four equations

$$\nabla \cdot \vec{E} = \frac{1}{\epsilon_0}\rho \tag{1}$$

$$\nabla \cdot \vec{B} = 0 \tag{2}$$

$$\nabla \times \vec{E} = -\frac{\partial \vec{B}}{\partial t} \tag{3}$$

$$\nabla \times \vec{B} = \mu_0 \vec{J} + \mu_0 \epsilon_0 \frac{\partial \vec{E}}{\partial t}, \tag{4}$$

and the force law

$$\vec{F} = q(\vec{E} + \vec{v} \times \vec{B}) \tag{5}$$

summarize the contents of classical electromagnetic theory.
The so-called Poisson equation can be obtained knowing that the electric field $\vec{E}$ can be written as the gradient of a scalar potential [15]:

$$\vec{E} = -\nabla V. \tag{6}$$

Using eq. 1, we have

$$\nabla^2 V = -\frac{\rho}{\epsilon_0}. \tag{7}$$

If matter is exposed to an electric field, charges will be displaced. Freely mobile charges will flow like a current, and bound charges will be displaced in a limited manner. These local charge displacements give rise to electric dipoles, and the sample becomes polarised. Two terms useful when describing polarisation effects are the polarisation $\vec{P}$ and the electric displacement $\vec{D}$. They are related to $\vec{E}$ and each other like

$$\vec{D} = \epsilon_0 \vec{E} + \vec{P}. \tag{8}$$

The polarisation is related to the electric field $\vec{E}$ via the dielectric susceptibility χ, through the relation

$$\vec{P} = \epsilon_0 \chi \vec{E}. \tag{9}$$

$\vec{P}$ represents the field-induced electric dipole moment per unit volume. The electric displacement $\vec{D}$ is related to the electric field by means of the equation

$$\vec{D} = \epsilon_0 \epsilon \vec{E}, \tag{10}$$

where ϵ is the dielectric constant.[1] As can be seen, the equations above imply that χ and ϵ links like

$$\epsilon = \chi + 1. \tag{11}$$

Magnetic fields arise, in general, from electric currents. The currents can be macroscopic, or microscopic, for instance like inside an atom. The atomic currents normally do not lead to any external effects, because they cancel inside the sample. However, if an magnetic field is applied, the sample may become magnetised. The total magnetic field $\vec{B}$ is the sum of the external magnetic field $\vec{H}$ and the magnetisation $\vec{M}$

$$\vec{B} = \mu_0 (\vec{H} + \vec{M}). \tag{12}$$

$\vec{M}$ and depends on $\vec{H}$ via the magnetic susceptibility κ,

$$\vec{M} = \kappa \vec{H}, \tag{13}$$

and $\vec{B}$ responds to $\vec{H}$ like

$$\vec{B} = \mu_0 \mu \vec{H}, \tag{14}$$

which means that the magnetic permeability μ relates to κ like

$$\mu = \kappa + 1. \tag{15}$$

When working with materials that are subject to electric and magnetic polarisation, it is convenient to rewrite Maxwell's equations, using the $\vec{D}$ and $\vec{H}$:

$$\nabla \cdot \vec{D} = \rho_f \tag{16}$$

$$\nabla \cdot \vec{B} = 0 \tag{17}$$

---

[1] Equations 9 and 10 applies only to media with linear response to electric fields. In most practical cases, this is valid.

$$\nabla \times \vec{E} = -\frac{\partial \vec{B}}{\partial t} \tag{18}$$

$$\nabla \times \vec{H} = \vec{J}_f + \frac{\partial \vec{D}}{\partial t}, \tag{19}$$

where the subscript f denotes *free.*

Waves

The concept of waves is a very important one in physics. A wave can be described as a *disturbance of a continuous medium that propagates with a fixed shape at a constant velocity* [15]. This description does not take standing waves or the fact that absorption is possible into account, but it gives an idea of what a wave is. An example of such a medium is a string. If the shape of the string is given by $f = f(x,t)$, and the continuous disturbance propagates with the velocity v, it is possible, using Newton's second law, to show that small disturbances on the string satisfy

$$\frac{\partial^2 f}{\partial x^2} = \frac{1}{v^2}\frac{\partial^2 f}{\partial t^2}. \tag{20}$$

This is equation is known as the *wave equation* [15].
Many functions obey 20. However, the sinusoidal wave form,

$$f(x,t) = A\cos[k(x - vt) + \delta] \tag{21}$$

is most commonly used. For a string, the amplitude A describes the maximum displacement from the equilibrium. k denotes the wave number. The argument of the cosine is called the phase. As the cosine function is a periodic one, it is possible to add an integer multiple of 2π to the phase without changing the wave. This means that advancing x with $\frac{2\pi}{k}$ makes the cosine execute one cycle. The distance between the same point of two cycles is usually called the wavelength, denoted by λ, and

$$\lambda = \frac{2\pi}{k}. \tag{22}$$

In the same manner, holding x constant, letting time increase (or decrease) with the amount $\frac{2\pi}{kv}$, the wave appears the same. This quantity is referred to as the period T:

$$T = \frac{2\pi}{kv}. \tag{23}$$

The frequency ν is the number of oscillations per unit time, hence

$$\nu = \frac{1}{T} = \frac{kv}{2\pi} = \frac{v}{\lambda}. \tag{24}$$

It is often convenient to use the angular frequency ω, which satisfies

$$\omega = 2\pi\nu. \tag{25}$$

Then, for a sinusiodal wave travelling in the positive x-direction, the mathematical description of it would be

$$f(x,t) = A\cos(kx - \omega t + \delta), \tag{26}$$

where δ is the phase offset.

When doing calculations involving wave functions, it is often easier to calculate using complex notation. In this case, the sinusoidal wave can be written as

$$f(x,t) = \Re[A\exp\left(i[kx - \omega t + \delta]\right)]. \tag{27}$$

Maxwell's equation consitute a set of coupled, first-order differential equations for $\vec{E}$ and $\vec{B}$. They can be decoupled by applying the curl to equations 3 and 4, i.e.

$$\begin{aligned}
\nabla \times (\nabla \times \vec{E}) &= \nabla(\nabla \cdot \vec{E}) - \nabla^2 \vec{E} &(28)\\
&= \nabla \times (-\frac{\partial \vec{B}}{\partial t}) &(29)\\
&= -\frac{\partial}{\partial t}(\nabla \times \vec{B}) &(30)\\
&= -\mu_0\epsilon_0 \frac{\partial^2 \vec{E}}{\partial t^2}. &(31)
\end{aligned}$$

In a similar way,

$$\nabla^2 \vec{B} = \mu_0\epsilon_0 \frac{\partial^2 \vec{B}}{\partial t^2}. \tag{32}$$

In fact, each of the Cartesian components of $\vec{E}$ and $\vec{B}$ satisfies the three-dimensional wave equation,

$$\nabla^2 f = \frac{1}{v^2}\frac{\partial^2 f}{\partial t^2}. \tag{33}$$

Maxwell's equations therefore imply that empty space supports the propagation of electromagnetic waves, travelling at the speed

$$v = \frac{1}{\sqrt{\epsilon_0\mu_0}} = 3.00 \times 10^8 \mathrm{m/s}. \tag{34}$$

This speed is the speed of light, and led Maxwell to believe that light in fact is electromagnetic waves, an assumption that no experiment yet has proven to be wrong.

Bibliography

[1] E. N. de Azevedo, M. Engelsberg, J. O. Fossum and R. E. de Souza, *Anisotropic water diffusion in nematic self-assemblies of clay nano-platelets suspended in water*, Langmuir 23, 5100, 2007.

[2] F. Bergaya, B. K. G. Theng, G. Lagaly, *Handbook of clay science*, Elsevier, 2006.

[3] http://www.bruker-axs.de/nanostar.html, from June 29, 2010.

[4] P. J. Collings and M. Hird, *Introduction to Liquid Crystals*, Taylor & Francis, 1997.

[5] A. H. Compton, *A Quantum Theory of the Scattering of X-rays by Light Elements*, Phys. Rev. 21, 483–502, 1923.

[6] http://www.esrf.eu/UsersAndScience/Experiments/CRG/BM26/, from June 29, 2010.

[7] S. Elliott, *The Physics and Chemistry of Solids*, John Wiley and Sons, 1998.

[8] R. Eppenga and D. Frenkel, *Monte Carlo study of the isotropic and nematic phases of infinitely thin hard platelets*, Molecular Physics, Volume 52, Issue 6, 1984.

[9] D. M. Fonseca, Y. Meheust, J. O. Fossum, K. D. Knudsen, K. J. Måløy and K. P. S. Parmar, *Phase behavior of platelet-shaped nanosilicate colloids in saline solutions: A small-angle X-ray scattering study*, J. Appl. Cryst. 40, 292, 2007.

[10] D. M. Fonseca, Y. Meheust, J. O. Fossum, K. D. Knudsen and K. P. S. Parmar, *Phase diagram of polydisperse Na fluorohectorite-water suspensions: A synchrotron small angle x-ray scattering study*, Phys. Rev. E 79, 021402, 2009.

[11] J. O. Fossum, *Physical phenomena in clays*, Physica A, 1999.

[12] J. O. Fossum, E. Gudding, D. M. Fonseca, Y. Meheust, E. DiMasi, T. Gog, C. Venkataraman, *Observations of orientational ordering in aqueous suspensions of a nano-layered silicate*, Energy The International Journal, Volume 3, 873-883, 2005.

[13] J. O. Fossum, Lecture notes from the course *Scattering by light, neutrons and x-rays*, taught fall 2009, NTNU.

[14] P. G. de Gennes and J. Prost, *The Physics of Liquid Crystals*, Oxford Science Publications, 2nd Edition, 1993.

[15] D. J. Griffiths, *Introduction to Electrodynamics*, Prentice-Hall International, 3rd Edition 1999.

[16] A. Guinier, *X-Ray Diffraction: In Crystals, Imperfect Crystals, and Amorphous Bodies*, Dover, New York, 1994.

[17] S. Hachisu, Y. Kobayashi, *Kirkwood-Alder transition in monodisperse latexes. II. Aqueous latexes of high electrolyte concentrations*, J. Coll. Interface Sci. 46:470, 1974.

[18] M. M. Hanczyc, S. M. Fujikawa, J. W. Szostak, *Experimental Models of Primitive Cellular Compartments: Encapsulation, Growth, and Division*, Science Vol. 302. no. 5645, 618 - 622, 2003.

[19] E. L. Hansen, *Colloidal Dispersions of Clay Nanoplatelets - Optical birefringence and x-ray scattering studies of nematic phases*, Master's thesis, Norwegian University of Science and Technology, 2008.

[20] E. L. Hansen, N. I. Ringdal, B. M. Kjelling, H. Hemmen, J. O. Fossum, E. N. de Azevedo, M. Engelsberg, Y. Meheust, C. Kim, S. Marathe, I. W. Cho and D. Y. Noh, *Highly ordered nematic phases and emerging positional ordering in aqeous dispersions of Sodium-Fluorohectorite (and Sodium-hectorite)*, date unknown.

[21] H. Hemmen, N. I. Ringdal, E. N. de Azevedo, M. Engelsberg, E. L. Hansen, Y. Meheust, J. O. Fossum and K. D. Knudsen, *The Isotropic-Nematic Interface in Suspensions of Na-Fluorohectorite Synthetic Clay*, Langmuir 25, 12507–12515, 2009.

[22] N. Ise, I. S. Sogami, *Structure Formation in Solution*, Springer, 2005.

[23] J. N. Israelachvili, *Intermolecular and Surface Forces*, Academic Press, London, 1991.

[24] P. D. Kaviratna, T. J. Pinnavaia and P. A. Schroeder, *Dielectric properties of smectite clays*, J. Phys. Chem. Solids 57, 1897-1906, 1996.

[25] M. Kleman, O. D. Lavrentovich, *Soft Matter Physics*, Springer, 2003.

[26] O. D. Lavrentovich *et al.* (eds), *Defects in Liquid Crystals: Computer Simulations, Theory and Experiments*, Kluwer Academic Press, 37-85, 2001.

[27] E. DiMasi, J. O. Fossum, T. Gog and C. Venkataraman, *Orientational order in gravity dispersed clay colloids: A synchrotron x-ray scattering study of Na-fluorohectorite suspensions*, Phys.Rev. E 64, 061704, 2001.

[28] Y. Meheust, S. Dagois-Bohy, K. D. Knudsen and J. O. Fossum, *Mesoscopic structure of dry-pressed clay samples from small-angle X-ray scattering measurements*, J. Appl. Cryst. 40, 286, 2007.

[29] A. Meunier, *Clays*, Springer, 2005.

[30] A. G. Michette and C. J. Buckley (eds.), *X-ray Science and Technology*, Institute of Physics Publishing, 1993.

[31] A. Mourchid and P. Levitz, *Long-term gelation of laponite aqueous dispersions*, Phys. Rev. E 57, 1998.

[32] L. Onsager, *The effects of shape on the interactions of colloidal particles*, Ann. N. Y. Acad. Sci. 51:627, 1949.

[33] A. C. Phillips, *Introduction to Quantum Mechanics*, Wiley, 2003.

[34] J. D. F. Ramsay, S. W. Swanton and J. Bunce, *Swelling and Dispersion of Smectite Clay Colloids: Determination of Structure by Neutron Diffraction and Small-angle Neutron Scattering*, J. Chem. Soc. Faraday Trans., 86 (23), 3919-3926, 1990.

[35] N. I. Ringdal, *Experimental studies of self-organized liquid crystalline phases from clay nanoplatelets in water: Birefringence and structure*, Master's thesis, Norwegian University of Science and Technology, 2008.

[36] N. I. Ringdal, D. M. Fonseca, E. L. Hansen, H. Hemmen, J. O. Fossum, *Nematic textures in colloidal dispersions of Na-fluorohectorite synthetic clay*, Phys. Rev. E 81, 041702, 2010.

[37] T. Scharf, *Polarized Light in Crystals and Polymers*, Wiley, 2007.

[38] G. J. da Silva, J. O. Fossum, E. DiMasi, K. J. Måløy and S. B. Lutnæs, *Synchrotron x-ray scattering studies of water intercalation in a layered synthetic silicate*, Phys. Rev. E 66 011303, 2002.

[39] G. Strobl, *Condensed Matter Physics,* Springer, 2004.

[40] R. P. Tenório, L. A. Alme, M. Engelsberg, J. O. Fossum and F. Hallwass, *Geometry and Dynamics of Intercalated Water in Na-Fluorhectorite Clay Hydrates*, J. Phys. Chem. C, 112, 575-580, 2008.

[41] J. A. C. Veerman and D. Frenkel, *Phase behavior of disklike hard-core mesogens*, Phys. Rev. A 45, 5632–5648, 1992.

[42] B. Velde, *Origin and Mineralogy of Clays*, Springer, 1995.